Effectiveness of Iterative Algorithms for Recovering Phase in the Presence of Noise for Coherent Diffractive Imaging

Henry Wittler

Supervisors: Michael Jones & Grant Van Riessen

November 17, 2012

Abstract

Methods of coherent diffractive imaging (CDI) rely on iterative algorithms to reconstruct the complex exit-surface wave (ESW) of the object being imaged from the measured diffraction intensity only. In this thesis we investigate by simulation the artifacts on reconstruction when noise are present in the measurement. We first confirmed the results obtained by Williams *et al.* [1, 2, 3] for plane-wave CDI, for reconstructions from simulated measurement data with various amount of shot-noise, non-sample beam scatter and background levels. Two kinds of iterative reconstruction algorithms were tested, error-reduction (ER) and hybrid-input output (HIO). An analogous examination of the effects of noise for Fresnel coherent diffractive imaging (FCDI) was then undertaken. The technique of FCDI requires a separate algorithm to recover the phase of the illumination, prior to the use of ER or HIO algorithm for obtaining the ESW of the object. Thus we simulated measurements of both the illumination and the diffracted intensity, with a certain amount of shot-noise and additionally equal or different amounts of background noise. This resulted in distinct artifacts on the reconstruction for the different noise types. A wide range of different error metrics was investigated for each noise type and level, for the reconstructed ESW and it's derived transmission function. Our results show that certain error metrics are very useful for identifying a good estimate to the generally unknown true solution, in any amount and type of noise tested. These observations will help to design FCDI experiments for optimal use of the available signal and to design new algorithms for iterative phase retrieval that can be applied to noisy data.

Contents

1 Introduction **2**
1.1 Motivation and Aim . . . 2

2 Coherent Diffractive Imaging **4**
2.1 Plane wave CDI . . . 4
2.1.1 CDI Phase-Retrieval Algorithms . . . 5
2.2 Fresnel Coherent Diffractive Imaging . . . 6
2.2.1 Fresnel CDI Phase Retrieval Algorithms . . . 7
2.2.2 White-Field Recovery . . . 8
2.3 Noise in Diffraction Imaging . . . 9
2.3.1 An Example of Measured Data . . . 10

3 Noise Simulation for Coherent Diffractive Imaging **12**
3.1 Experiment simulation . . . 12
3.2 Reconstructions . . . 15
3.2.1 Photon Number . . . 18
3.2.2 Alien Sources of X-ray Scatter . . . 20
3.2.3 Incomplete Background Subtraction . . . 22
3.3 Conclusions . . . 24

4 Noise Simulation for Fresnel Coherent Diffractive Imaging **25**
4.1 Experiment . . . 25
4.1.1 Geometry & Parameters . . . 25
4.1.2 Combining CCD Data . . . 27
4.2 Experiment simulation . . . 30
4.3 Reconstructions . . . 34
4.3.1 Zero Noise Solution . . . 36
4.3.2 Photon Number . . . 38
4.3.2.1 Iteration number . . . 41
4.3.3 Incomplete Background Subtraction . . . 45
4.3.3.1 Case I . . . 46
4.3.3.2 Case II . . . 48
4.3.3.3 Case III . . . 50
4.3.3.4 Additional Tests . . . 52
4.4 Conclusions . . . 53

5 Retrospect and Further Investigation **56**

A All Reconstructions from Chapter 3 Noise-Added Simulation for Coherent Diffractive Imaging **57**
A.1 Photon Number . . . 57
A.2 Alien Scatterers . . . 65
A.3 Incomplete Background Subtraction . . . 69

B Reconstructions from Chapter 4 Noise-Added Simulation for Fresnel Coherent Diffractive Imaging **75**
B.1 Photon Number . . . 75
B.2 Incomplete Background Subtraction . . . 82
B.2.1 Case (I) . . . 85
B.2.2 Case (II) . . . 89
B.2.3 Case (III) . . . 94
B.2.4 Error Metrics of Chapter 4, Comparing Magnitude And Phase Entities . . . 99
B.2.4.1 Photon number . . . 99
B.2.4.2 Iteration number . . . 99
B.2.4.3 Incomplete Background Subtraction . . . 101
B.2.4.4 Additional tests . . . 102

List of Figures

2.1.1 Schematic of the geometry of a plane wave CDI setup 4
2.1.2 Illustration of the support and modulus constraint. 6
2.2.1 Schematic of a FCDI experiment 7
2.3.1 Experimental data frame collected in a 1 second interval. 11

3.1.1 Examples of the procedure to simulate measurement data with different sources of noise. 14
3.1.2 The true ESW generated for comparisons to reconstructions by ER and HIO. . . 15
3.2.1 Scatter plots of ξ_1^0, ξ_1^2 and χ^2 against SNR for different noise types; (a) Photon number, (b) Alien scattering, (c) Background noise. 17
3.2.2 Scatter plots of ξ_1^0, ξ_1^2 and χ^2 against SNR for different noise, (a) Photon number, (b) Alien scattering, (c) Background noise. Original work of Reference [1]. 17
3.2.3 Magnitude of reconstructed iterate by ER and HIO, from diffraction data with shot-noise for (a) 9×10^4 photons, and (b) 10^9 photons. 19
3.2.4 Magnitude of reconstructed iterate by ER and HIO, from diffraction data with shot-noise for 9×10^4 photons and additional shot-noise due to a Poisson distributed mean of (a) 0.5 alien photons, and (b) 0.0005 alien photons. 21
3.2.5 Magnitude of reconstructed iterate by ER and HIO, from diffraction data with inherent shot-noise for 9×10^4 photons and inclusive background that have been (a) 0% background subtracted, (b) 100% background subtracted. 23

4.1.1 Illustration of an FCDI geometry 26
4.1.2 Cross-correlation function plot 28
4.1.3 Illustration of FCDI data treatment 29
4.2.1 Examples for the procedure to simulate measured diffraction and white-field data with different sources of noise. 33
4.2.2 The true ESW with it's TF used for comparison to solutions by ER and HIO obtained by noise added diffraction and white-field data. 34
4.3.1 Two solutions by ER and HIO, from simulated diffraction and white-field data that has no noise inherent.. 37
4.3.2 Solution by ER and HIO from diffraction and white-field data with three different amounts of shot-noise. 39
4.3.3 Error metric results for reconstructions to diffraction and white-field data, for a wide range of shot-noise.. 40
4.3.4 Iteration number dependency on solutions and error metrics, for diffraction and white-field data that have only shot-noise inherent for 5×10^5 measured photons. 42
4.3.5 Iteration number dependency on solutions and error metrics, for diffraction and white-field data that have only shot-noise inherent for 10^9 measured photons. . . 43
4.3.6 Iteration number dependency on solutions and error metrics, for diffraction and white-field data that have only shot-noise inherent for 10^{14} measured photons. . 44
4.3.7 The error metric results, for ER and HIO reconstructions from diffraction and white-field data that have equally 0-100% background subtraction. With shot-noise for 10^9 and 10^{11} measured photons. 46

4.3.8 Two solutions, by ER and HIO, from diffraction and white-field data that have equal 0-100% background subtraction. With shot-noise for 10^9 measured photons. 47
4.3.9 Error metrics results for reconstructions by ER and HIO, from diffraction data that have 0-100% background subtraction, for a fixed white-field data with 100% background subtracted. With shot-noise for 10^9 and 10^{11} measured photons. . . 48
4.3.10 Two solutions, by ER and HIO, from diffraction data that have 0-100% background subtraction, for a fixed white-field data with 100% background subtracted. With shot-noise for 10^9 measured photons. 49
4.3.11 Error metrics results for reconstructions by ER and HIO, from diffraction data that have 0-100% background subtraction, for a fixed white-field data with 95% background subtracted. With shot-noise for 10^9 and 10^{11} measured photons. . . 50
4.3.12 Two solutions by ER and HIO, from diffraction data that have 0-100% background subtraction, for a fixed white-field data with 95% background subtracted. With shot-noise for 10^9 measured photons. 51
4.3.13 Error metrics results by reconstructions for ER and HIO, from diffraction data that have 0-100% background subtraction, for a fixed white-field data with 0% background subtracted. With shot-noise for 10^9 and 10^{11} measured photons. . . 52
4.3.14 Error metrics results by reconstructions for ER and HIO, from diffraction data that have 10-90% background subtraction, for a fixed white-field data with 50% background subtracted. With shot-noise for 10^9 and 10^{11} measured photons. . . 53

A.1.1 All simulated diffraction data with different amount of shot-noise or measured photons, for Section 3.2.1 58
A.1.2 Reconstructed iterate from diffraction data with shot-noise for 9×10^4 measured photons. 59
A.1.3 Reconstructed iterate from diffraction data with shot-noise for 2×10^5 measured photons. 59
A.1.4 Reconstructed iterate from diffraction data with shot-noise for 5×10^5 measured photons. 60
A.1.5 Reconstructed iterate from diffraction data with shot-noise for 10^6 measured photons. 60
A.1.6 Reconstructed iterate from diffraction data with shot-noise for 2×10^6 measured photons. 61
A.1.7 Reconstructed iterate from diffraction data with shot-noise for 5×10^6 measured photons. 61
A.1.8 Reconstructed iterate from diffraction data with shot-noise for 10^7 measured photons. 62
A.1.9 Reconstructed iterate from diffraction data with shot-noise for 5×10^7 measured photons. 62
A.1.10 Reconstructed iterate from diffraction data with shot-noise for 10^8 measured photons. 63
A.1.11 Reconstructed iterate from diffraction data with shot-noise for 5×10^8 measured photons. 63
A.1.12 Reconstructed iterate from diffraction data with shot-noise for 10^9 measured photons. 64
A.2.1 All simulated diffraction data with shot-noise for 9×10^4 and additional shot-noise due to differing alien scattered photon mean, per pixel, drawn from a Poisson distribution, for Section 3.2.2. 65
A.2.2 Reconstructed iterate from diffraction data with shot-noise for 9×10^4 measured photons, and additional shot-noise, per pixel, drawn from a Poisson distrubution of mean 0.5. 66
A.2.3 Reconstructed iterate from diffraction data with shot-noise for 9×10^4 measured photons, and additional shot-noise, per pixel, drawn from a Poisson distrubution of mean 0.05. 66

A.2.4 Reconstructed iterate from diffraction data with shot-noise for 9×10^4 measured photons, and additional shot-noise, per pixel, drawn from a Poisson distrubution of mean 0.005. 67
A.2.5 Reconstructed iterate from diffraction data with shot-noise for 9×10^4 measured photons, and additional shot-noise, per pixel, drawn from a Poisson distrubution of mean 0.0013. 67
A.2.6 Reconstructed iterate from diffraction data with shot-noise for 9×10^4 measured photons, and additional shot-noise, per pixel, drawn from a Poisson distrubution of mean 0.0005. 68
A.3.1 All simulated diffraction data with shot-noise for 9×10^4 measured photons, and inherent background noise, that are between 0-100% background subtracted. For Section 3.2.3. 69
A.3.2 Reconstructed iterate from diffraction data with shot-noise for 9×10^4 measured photons, and included background noise that are 0% subtracted 70
A.3.3 Reconstructed iterate from diffraction data with shot-noise for 9×10^4 measured photons, and included background noise that are 10% subtracted 70
A.3.4 Reconstructed iterate from diffraction data with shot-noise for 9×10^4 measured photons, and included background noise that are 30% subtracted 71
A.3.5 Reconstructed iterate from diffraction data with shot-noise for 9×10^4 measured photons, and included background noise that are 50% subtracted 71
A.3.6 Reconstructed iterate from diffraction data with shot-noise for 9×10^4 measured photons, and included background noise that are 70% subtracted 72
A.3.7 Reconstructed iterate from diffraction data with shot-noise for 9×10^4 measured photons, and included background noise that are 90% subtracted 72
A.3.8 Reconstructed iterate from diffraction data with shot-noise for 9×10^4 measured photons, and included background noise that are 95% subtracted 73
A.3.9 Reconstructed iterate from diffraction data with shot-noise for 9×10^4 measured photons, and included background noise that are 99% subtracted 73
A.3.10 Reconstructed iterate from diffraction data with shot-noise for 9×10^4 measured photons, and included background noise that are 100% subtracted 74

B.1.1 All simulated diffraction data with inherent shot-noise for different number of measured photons as described in Section 4.3.2. 76
B.1.2 Reconstructed solution and TF from diffraction and white-field data with shot-noise for 5×10^5 measured photons. 77
B.1.3 Reconstructed solution and TF from diffraction and white-field data with shot-noise for 10^6 measured photons 77
B.1.4 Reconstructed solution and TF from diffraction and white-field data with shot-noise for 5×10^6 measured photons. 78
B.1.5 Reconstructed solution and TF from diffraction and white-field data with shot-noise for 10^8 measured photons 78
B.1.6 Reconstructed solution and TF from diffraction and white-field data with shot-noise for 10^9 measured photons 79
B.1.7 Reconstructed solution and TF from diffraction and white-field data with shot-noise for 5×10^9 measured photons. 79
B.1.8 Reconstructed solution and TF from diffraction and white-field data with shot-noise for 10^{10} measured photons 80
B.1.9 Reconstructed solution and TF from diffraction and white-field data with shot-noise for 5×10^{10} measured photons 80
B.1.10 Reconstructed solution and TF from diffraction and white-field data with shot-noise for 10^{11} measured photons 81
B.1.11 Reconstructed solution and TF from diffraction and white-field data with shot-noise for 10^{12} measured photons 81
B.1.12 Reconstructed solution and TF from diffraction and white-field data with shot-noise for 10^{14} measured photons 82

B.2.1 All simulated diffraction data with shot-noise for 10^9 measured photons and different amount of background subtracted. Used in Section 4.3.3, for different comparison means to background subtracted white-field data, that has equal amount of shot-noise.. 84
B.2.2 Reconstructed solution and TF from background subtracted data: 0% in diffraction data, 0% in white-field data, with shot-noise for 10^9 measured photons. 85
B.2.3 Reconstructed solution and TF from background subtracted data: 10% in diffraction data, 10% in white-field data, with shot-noise for 10^9 measured photons. 85
B.2.4 Reconstructed solution and TF from background subtracted data: 30% in diffraction data, 30% in white-field data, with shot-noise for 10^9 measured photons. 86
B.2.5 Reconstructed solution and TF from background subtracted data: 50% in diffraction data, 50% in white-field data, with shot-noise for 10^9 measured photons. 86
B.2.6 Reconstructed solution and TF from background subtracted data: 70% in diffraction data, 70% in white-field data, with shot-noise for 10^9 measured photons. 87
B.2.7 Reconstructed solution and TF from background subtracted data: 90% in diffraction data, 90% in white-field data, with shot-noise for 10^9 measured photons. 87
B.2.8 Reconstructed solution and TF from background subtracted data: 95% in diffraction data, 95% in white-field data, with shot-noise for 10^9 measured photons. 88
B.2.9 Reconstructed solution and TF from background subtracted data: 99% in diffraction data, 99% in white-field data, with shot-noise for 10^9 measured photons. 88
B.2.10 Reconstructed solution and TF from background subtracted data: 100% in diffraction data, 100% in white-field data, with shot-noise for 10^9 measured photons. 89
B.2.11 Reconstructed solution and TF from background subtracted data: 0% in diffraction data, 100% in white-field data, with shot-noise for 10^9 measured photons. 89
B.2.12 Reconstructed solution and TF from background subtracted data: 10% in diffraction data, 100% in white-field data, with shot-noise for 10^9 measured photons. 90
B.2.13 Reconstructed solution and TF from background subtracted data: 30% in diffraction data, 100% in white-field data, with shot-noise for 10^9 measured photons. 90
B.2.14 Reconstructed solution and TF from background subtracted data: 50% in diffraction data, 100% in white-field data, with shot-noise for 10^9 measured photons. 91
B.2.15 Reconstructed solution and TF from background subtracted data: 70% in diffraction data, 100% in white-field data, with shot-noise for 10^9 measured photons. 91
B.2.16 Reconstructed solution and TF from background subtracted data: 90% in diffraction data, 100% in white-field data, with shot-noise for 10^9 measured photons. 92
B.2.17 Reconstructed solution and TF from background subtracted data: 95% in diffraction data, 100% in white-field data, with shot-noise for 10^9 measured photons. 92
B.2.18 Reconstructed solution and TF from background subtracted data: 99% in diffraction data, 100% in white-field data, with shot-noise for 10^9 measured photons. 93

B.2.19 Reconstructed solution and TF from background subtracted data: 100% in diffraction data, 100% in white-field data, with shot-noise for 10^9 measured photons. 93
B.2.20 Reconstructed solution and TF from background subtracted data: 0% in diffraction data, 95% in white-field data, with shot-noise for 10^9 measured photons. 94
B.2.21 Reconstructed solution and TF from background subtracted data: 10% in diffraction data, 95% in white-field data, with shot-noise for 10^9 measured photons. 94
B.2.22 Reconstructed solution and TF from background subtracted data: 30% in diffraction data, 95% in white-field data, with shot-noise for 10^9 measured photons. 95
B.2.23 Reconstructed solution and TF from background subtracted data: 50% in diffraction data, 95% in white-field data, with shot-noise for 10^9 measured photons. 95
B.2.24 Reconstructed solution and TF from background subtracted data: 70% in diffraction data, 95% in white-field data, with shot-noise for 10^9 measured photons. 96
B.2.25 Reconstructed solution and TF from background subtracted data: 90% in diffraction data, 95% in white-field data, with shot-noise for 10^9 measured photons. 96
B.2.26 Reconstructed solution and TF from background subtracted data: 95% in diffraction data, 95% in white-field data, with shot-noise for 10^9 measured photons. 97
B.2.27 Reconstructed solution and TF from background subtracted data: 99% in diffraction data, 95% in white-field data, with shot-noise for 10^9 measured photons. 97
B.2.28 Reconstructed solution and TF from background subtracted data: 100% in diffraction data, 95% in white-field data, with shot-noise for 10^9 measured photons. 98
B.2.29 Error metrics of Section 4.3.2 (Photon number). Entities compared, (a) magnitude, (b) phase. 99
B.2.30 Error metrics of Section 4.3.2.1 (Iteration number), case 5×10^5 photons. Entities compared, (a) magnitude, (b) phase. 99
B.2.31 Error metrics of Section 4.3.2.1 (Iteration number), case 10^9 photons. Entities compared, (a) magnitude, (b) phase. 100
B.2.32 Error metrics of Section 4.3.2.1 (Iteration number), case 10^{14} photons. Entities compared, (a) magnitude, (b) phase. 100
B.2.33 Error metrics of Section 4.3.3.1 (Case I). Entities compared, (a) magnitude, (b) phase. 101
B.2.34 Error metrics of Section 4.3.3.2 (Case II). Entities compared, (a) magnitude, (b) phase. 101
B.2.35 Error metrics of Section 4.3.3.3 (Case III). Entities compared, (a) magnitude, (b) phase. 102
B.2.36 Error metrics of Section 4.3.3.4 (Additional tests; 0% background subtracted white-field data, 0-100% background subtracted diffraction data). Entities compared, (a) magnitude, (b) phase. 102
B.2.37 Error metrics of Section 4.3.3.4 (Additional tests; 50% background subtracted white-field data, 0-100% background subtracted diffraction data). Entities compared, (a) magnitude, (b) phase. 103

List of Tables

4.1 Error metric values from diffraction and white-field data with no noise inherent. 36
4.2 The $\chi^2_{reciprocal}$ values used for sorting solutions obtained from data with no noise inherent. 36

Acknowledgement

I would like to express appreciation and gratitude to my supervisors Michael Jones and Grant van Riessen. They have supported me with the project, and have read the thesis many times, giving valuable and detailed comments. I also appreciate their patience, because I've prolonged the close-date of this thesis partly due to intervening courses and other work.

I would also like to thank all the people of the x-ray physics group of La trobe university, and many other members at the centre of excellence for coherent x-ray science (CXS), for the experience in this research area, discussions, and for making me a part of the team.
Thanks to Corey Putkunz for discussion and assistance with FCDI information. And thanks to Nadia Davidson for help and mutual development of the simulation code.
The organisation IASTE, Proffessor Andrew Peele and Dr Chanh Tran helped me become a trainee at CXS in the first place, when other options was closed.

I thank Gergely Katona, researcher at the Department of Chemistry and Molecular biology Gothenburg University, for being the examinator for this thesis.

I am grateful for the constant financial support and encouragement from my family, without them matters would have been much more challenging.

Chapter 1

Introduction

The penetrating nature and short wavelength of X-rays has long made X-ray techniques popular for investigating a wide range of materials. A popular form of an X-ray technique is X-ray crystallography whereby detailed structural information are obtained from X-ray diffraction data. X-ray crystallography has a record of extraordinary achievement in science, for example elucidating the molecular structure of DNA [4]. It elucidates the structure of a molecules electron density, by requiring repeating units of the molecule in a lattice such as a crystal, to achieve sufficient X-ray diffraction signal. However a major problem for the design of new pharmaceuticals, is that membrane proteins do not typically form the crystals needed to enable further investigation of their structure [5]. The availability of third-generation synchotrons and X-ray free-electron lasers with increasing brightness are driving the development of many new methods of microscopy. Among these techniques is coherent diffractive imaging (CDI), enabling nanometre-scale imaging of non-crystallographic samples.

Coherent diffractive imaging is a technique where a crystalline or non-crystalline sample is illuminated with planar coherent X-rays and the diffracted photons form a pattern of varying intensity, measured by a detector in a far field distance. In such a measurement, the phase information is lost, however iterative algorithms are used that constrains the reconstructed "exit-surface wave" leaving the sample to be mutually consistent with the measured diffraction intensity and *a priori* knowledge of sample extent. An intrinsic problem of CDI is the uniqueness of the reconstruction, one can prove that generally a unique solution exist, though there can be trivial ambiguities which include phase offsets, 'twin' images and variation in position of the reconstructed exit-surface wave [6].
A similar technique called Fresnel coherent diffractive imaging (FCDI) uses a curved illumination on the sample, producing a Fresnel diffraction intensity pattern from which one may retrieve an image of the sample through iterative algorithms, similar to the case of CDI. In an FCDI experiment the sample can be larger than the illumination, as the illumination extent provides a constraint to the solution of the exit-surface wave. However characterisation of the illumination is needed for the iterative algorithms to be applied [7]. It has been shown that there exists only one unique solution to the FCDI problem [8], as such the ambiguities present in CDI does not exist.

1.1 Motivation and Aim

The succesful application of any iterative algorithm requires an accurate model for the data acqusition process. There have been research on the effects of deviation from perfect spatial coherence of the illuminating beam, establishing that deviations from ideal conditions that are implicit in formulation of CDI algorithms can have unfavorable effects on the quality of reconstruction [9, 10]. Of additional concern is that there may be deviations from the ideal case because of impact of noise due to low photon counts or other sources of noise. Since the measurement of these diffraction patterns records the intensity in the reciprocal space [11], any errors due to noise will probably not have a straightforward impact on the resulting real-space result.

For the technique of CDI, the effects of noise in measurements has already been extensively investigated by Williams *et al.* [1, 2, 3]. They simulated the effects on reconstruction for varying ranges of alien x-ray beam scatter, shot-noise and background levels in the measured diffraction intensity data. Williams *et al.* showed that the different kinds of noise will result in characteristic artifacts on the reconstruction [1, 2, 3]. Their analysis included the applicability of different error metrics to identify a reconstruction of acceptable quality and fidelity, in the presence of noise. In addition they investigated for how much levels of different sources of noise are acceptable to obtain a reconstruction of sufficient fidelity. Their analysis included different samples, iterative algorithms and parameters. For this thesis the aim is to first reproduce a subset of the results of Williams *et al.* [1, 2, 3]. Then our second aim is to extend the approach for an analogous investigation to the technique of FCDI, for which such an analysis had not yet been performed. For FCDI we wish to examine effects on the reconstruction for different levels of shot-noise and background-noise present in the data. This includes relative levels of background-noise in the data from diffraction and illumination respectively, and how this may affect the reconstruction. This is used to arrive at a prediction for what levels of noise can be tolerated to arrive at a FCDI reconstruction of sufficient fidelity. This analysis may have implication for the choice of experimental parameters, algorithms and detector technology. Additionally we wish to examine different error metrics to see if they can be used to identify a reconstruction of sufficient fidelity in the presence of noise.

Chapter 2

Coherent Diffractive Imaging

In this chapter we provide a brief overview of the techniques and iterative algorithms for the methods of coherent diffractive imaging (CDI) in Section 2.1, and Fresnel coherent diffractive imaging (FCDI) in Section 2.2. An overview of noise in diffraction imaging will also be provided in Section 2.3. The underlying theory of CDI including wave propagation and X-ray interaction with matter is not covered in detail here, this are covered extensively in for example References [12, 13, 14].

2.1 Plane wave CDI

Plane wave CDI is a lensless imaging technique where the intensity of the beam diffracted by a sample is measured by a detector at a far-field distance. This measured diffraction pattern intensity has a Fourier transform relationship with the sample. Through iterative algorithms the phase of the diffraction pattern intensity is also retrieved and with it information about the structure of the object illuminated.

In a CDI experiment [12, 15] a quasi-monochromatic beam of planar X-rays is incident on a beam defining aperture in order to increase the coherence of the beam and define an area of illumination. The beam is then incident on a sample with dimensions less than the illumination extent. Both transmitted light and the diffracted wavefield propagate through free space to the detector. The transmitted beam may be blocked by a beam stop to avoid damage to the CCD detector. A schematic of a CDI experiment are shown in Figure 2.1.1.

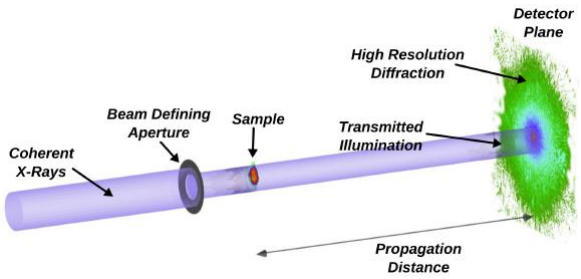

Figure 2.1.1: Geometry of a plane wave CDI experiment. Incident planar X-rays are reduced by a beam defining aperture, then incident on a sample smaller than the illumination extent. The unperturbed and diffracted wave-field propagate to the detector, where the unperturbed beam is blocked by a beam stop and the diffracted wave-field are measured.
Figure reprinted from [12], courtesy of C. T. Putkunz.

The measured intensity is proportional to the square of the magnitude of the diffracted wave-field, however the phase information of the diffracted wave-field is not measured by the detector [12, 15]. The measured intensity $I(\boldsymbol{\rho}_d)$, is related to the diffracted wave-field in the detector plane $\psi(\boldsymbol{\rho}_d)$, by

$$I(\boldsymbol{\rho}_d) = |\psi(\boldsymbol{\rho}_d)|^2 , \tag{2.1.1}$$

where $\boldsymbol{\rho}_d$ is the plane coordinate in the detector pixel array.

The samples exit surface wave (ESW) $\psi(\boldsymbol{\rho}_s)$, is related to the line integral of the sample complex scattering potential, $\frac{k^2}{4\pi}\int_{z_S}(1-n^2(\boldsymbol{\rho}_s))dz$ [12], where $\boldsymbol{\rho}_s$ is the plane coordinate in the sample plane, $n(\boldsymbol{\rho}_s)$ is the refractive index of the sample, and z being the axis along the beam trajectory.
The diffracted wave-field at the detector, with known magnitude and phase, are proportional to the ESW by a two-dimensional Fourier transform, [12, 15]

$$\psi(\boldsymbol{\rho}_d) \propto \mathcal{F}[\psi(\boldsymbol{\rho}_s)]. \tag{2.1.2}$$

Furthermore an inverse Fourier transform on the diffracted wave-field in the detector plane yields the ESW in the sample plane. This relationship between the measured intensity and the ESW is the basis of the formulation of CDI [12].

To recover the phase information of the diffracted wave-field and therefore the ESW, iterative algorithms are used (to be explained in Section 2.1.1). These algorithms start with a random guess of the phase of the diffracted wavefield, and in order for them to converge to a solution, an 'oversampling condition' must be met. The oversampling condition is for two dimensional imaging given by [13],

$$\sigma = \frac{\text{Total number of sample points}}{\text{Number of sample points inside support}} \geq 4 . \tag{2.1.3}$$

The concept of the oversampling condition is related to the Fourier phase problem which involves a large set of simultaneous non-linear equations that require fulfillment of both the support and modulus constraints [12, 13, 15]. The support constraint defines a region containing the ESW of sample, and requires the region outside to be zero. The modulus constraint [16] requires that the intensity of the recovered wave-field at the detector plane agrees with the measured intensity. If the oversampling condition is realised there will be more equations than unknowns, then iterative algorithms can converge to a solution that is unique (although with ambiguities as translation or phase offsets in the case of CDI) [12].

2.1.1 CDI Phase-Retrieval Algorithms

In this thesis we only investigate two common phase-retrieval algorithms, error reduction (ER) [16] and hybrid-input output (HIO) [16, 17]. These are only two amongst several iterative methods used to retrieve the phase of the diffracted wavefield in the detector plane [13]. Common to all of these iterative algorithms are the support and modulus constraints, illustrated in Figure 2.1.2. The support constraint operator π_s defines a region $\mathcal{S}$ in the sample plane containing the ESW and makes everything outside to zero [12, 13],

$$\psi'(\boldsymbol{\rho}_s) = \begin{cases} 0 & \forall \boldsymbol{\rho}_s \notin \mathcal{S} \\ \psi(\boldsymbol{\rho}_s) & \forall \boldsymbol{\rho}_s \in \mathcal{S} \end{cases} . \tag{2.1.4}$$

The modulus constraint operator $\hat{\pi}_m$ (where $\hat{}$ refers to the detector plane) replaces the magnitude of the wavefield $\psi'(\boldsymbol{\rho}_d)$ of the current iterate to the measured intensity $\sqrt{I}$ for each pixel [12, 18],

$$\psi'(\boldsymbol{\rho}_d) = \sqrt{I(\boldsymbol{\rho}_d)}\frac{\psi(\boldsymbol{\rho}_d)}{|\psi(\boldsymbol{\rho}_d)|} . \tag{2.1.5}$$

The propagated modulus constraint is used in the sample plane,

$$\pi_m = \mathcal{F}^{-1}\hat{\pi}_m\mathcal{F}\,, \tag{2.1.6}$$

where $\mathcal{F}$ is the Fourier transform.

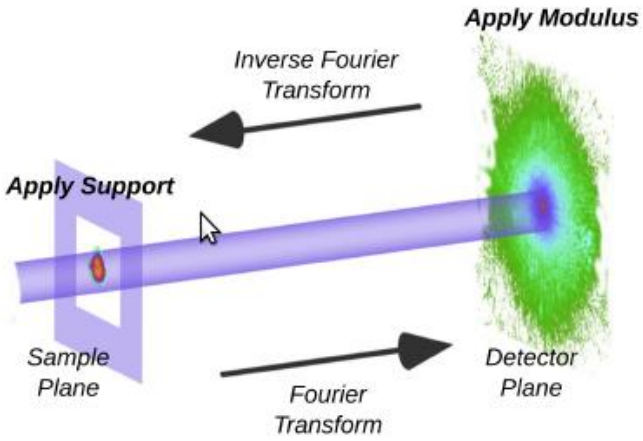

Figure 2.1.2: Illustration of two operators with application in iterative algorithms. "Apply support" means to set the complex numbers to zero outside a region containing the iterate. "Apply modulus" means that one Fourier transforms the current iterate, replaces the magnitude of the diffracted wavefield with the square root of the measured intensity, however keeping the phase, then an inverse Fourier transform back to the sample plane is performed. *Figure reprinted from [12], courtesy of C. T. Putkunz.*

With these operators the error reduction algorithm is given by ,

$$\rho_{k+1} = \pi_s\pi_m\rho_k\,, \tag{2.1.7}$$

where ρ_k is the k'th iterate of the ESW in sample plane. This algorithm thus consists of a propagation to detector plane, application of the modulus constraint, propagation back to sample plane, and the application of the support constraint.

The hybrid-input output algorithm are given by,

$$\rho_{k+1} = [1 + (1+\beta)\pi_s\pi_m - \pi_s - \beta\pi_m]\rho_k\,, \tag{2.1.8}$$

where β is a real scalar.

2.2 Fresnel Coherent Diffractive Imaging

In an FCDI experiment coherent planar X-rays illuminate a focusing optic, for example a Fresnel zone plate (FZP) [19]. The combination of the FZP central beam-stop and an order sorting aperture (OSA) allows only the first order illumination to exit the OSA to illuminate the sample. A sample which can be larger than the incident beam is placed at a de-focused distance from the OSA, with the illumination defining the area to be imaged. A schematic of an FCDI experiment is shown in Figure 2.2.1. To obtain the benefits of FCDI, sufficient curvature in the illumination are required. The degree of curvature required is defined by a Fresnel number N_F to be greater than or equal to five across the sample [12, 20]. This in turn determines the distance between the the focal point and the sample z_{FS} . The Fresnel number is defined as [21]

$$N_F = \frac{a^2}{\lambda z_{FS}}\,, \tag{2.2.1}$$

where a is a measure of the sample radius, λ is the x-ray wavelength.

The resulting diffraction pattern at the detector at a far-field distance, consists of a holographic region which contains the interference information between the diffraction from the

sample and the diverging undiffracted beam. In addition at higher angles than the extent of the undiffracted illumination there is higher resolution information of the sample, available from diffraction intensity.

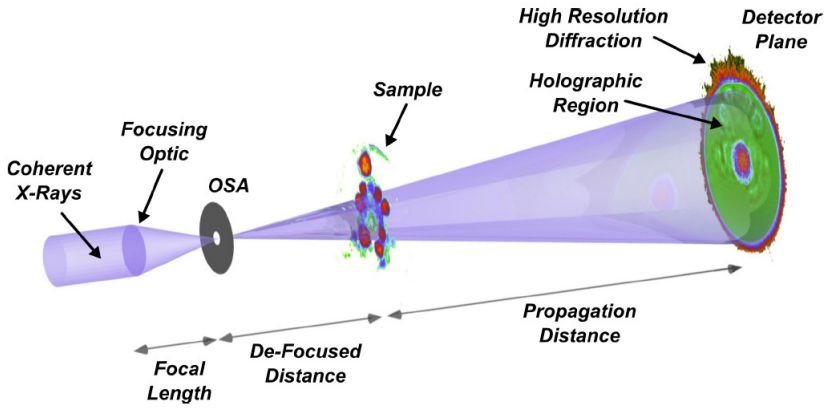

Figure 2.2.1: Schematic of a Fresnel CDI experiment. Planar X-rays are incident on the Fresnel zone plate and then conditioned by an order sorting aperture. Interaction of the diverging curved illumination and the sample produces a Fresnel diffraction pattern in the far field, which includes a central holographic region and high angle scatter.
Figure reprinted from [12], courtesy of C. T. Putkunz.

2.2.1 Fresnel CDI Phase Retrieval Algorithms

In general the iterative algorithms used for CDI are also applicable to FCDI. However instead of a Fourier transform, there is a Fresnel transform relationship between the samples ESW and the measured intensity at detector. This relationship between arbitrary planes i, j is called the Fresnel free space propagator or Fresnel transform [12, 22],

$$\psi(\boldsymbol{\rho}_j, z_j) = \frac{\pi}{\lambda z_{ij}} e^{ikz_{ij}} e^{\frac{i\pi\boldsymbol{\rho}_d^2}{\lambda z_{ij}}} \mathcal{F}[\psi(\boldsymbol{\rho}_i, z_i) e^{\frac{i\pi\boldsymbol{\rho}_i^2}{\lambda z_{ij}}}] = \mathcal{F}_F \psi(\boldsymbol{\rho}_i) = A(\boldsymbol{\rho}_j, z_{ij}) \mathcal{F}\left[\psi(\boldsymbol{\rho}_i, z_i) B(\boldsymbol{\rho}_i, z_{ij})\right] , \tag{2.2.2}$$

where $\mathcal{F}$ is a Fourier transform, $\mathcal{F}_F$ is a Fresnel transform, k is the wave-number and z_{SD} is the distance from sample to detector. The functions A and B can further be described in operator form; π_A^{ij} and π_B^{ij}. Thus one may write the Fresnel transform and its inverse in an operator form,

$$\begin{aligned} &Fresnel\,Transform && \mathcal{F}_F := \pi_A^{ij} \mathcal{F} \pi_B^{ij} , \\ &Inverse\,Fresnel\,Transform && \mathcal{F}_F^{-1} := \pi_A^{ji} \mathcal{F}^{-1} \pi_B^{ji} . \end{aligned}$$

The Fresnel transform allows phase retrieval using spherical illumination. By the projection approximation [14], the ESW of the sample is given by [12, 22],

$$\psi(\boldsymbol{\rho}_s) = e^{-ik\int^z \delta(\boldsymbol{\rho}_s, z) - i\beta(\boldsymbol{\rho}_s, z) dz} \psi_0(\boldsymbol{\rho}_s) = T(\boldsymbol{\rho}_s) \psi_0(\boldsymbol{\rho}_s) , \tag{2.2.3}$$

where $\psi_0(\boldsymbol{\rho}_s)$ is the illumination and $T(\boldsymbol{\rho}_s)$ is the transmission function, δ is the real and β the complex part of the refractive index, z is the distance in the direction of propagation. The amplitude and phase component of the transmission function is thus given by,

$$e^{-ik\int^z \delta(\boldsymbol{\rho}_s, z) - i\beta(\boldsymbol{\rho}_s, z) dz} = e^{-k\int_z \beta dz} e^{-ik\int_z \delta dz} = |T| e^{i\phi_T} , \tag{2.2.4}$$

$$|T| = e^{-k\int_z \beta dz} , \tag{2.2.5}$$

$$\phi_T = -k \int_z \delta dz \,. \tag{2.2.6}$$

The incoming illumination, henceforth refered to as the white-field, is subtracted from the iterate of the estimation to the ESW,

$$\psi^\star(\boldsymbol{\rho}_s) = \psi_0(\boldsymbol{\rho}_s)T(\boldsymbol{\rho}_s) - \psi_0(\boldsymbol{\rho}_s) = \psi_0(\boldsymbol{\rho}_s)[T(\boldsymbol{\rho}_s) - 1] \,. \tag{2.2.7}$$

Hence to obtain the transmission function, we recast Equation 2.2.7,

$$T(\boldsymbol{\rho}_s) = \frac{\psi^\star(\boldsymbol{\rho}_s)}{\psi_0(\boldsymbol{\rho}_s)} + 1. \tag{2.2.8}$$

The Fresnel support constraint π_s^F (same as π_s in CDI) is acting on the white field subtracted iterate $\psi^\star(\boldsymbol{\rho}_s)$ [23].

The Fresnel modulus constraint π_m^F, consists of the following steps: (i) propagate from the sample plane to detector plane, $\mathcal{F}_F$, (ii) add the recovered white field to $\psi^\star(\boldsymbol{\rho}_d)$, π_{WF}, (iii) enforce the measured intensity, $\hat{\pi}_m$, (iv) subtract the white field, π_{WF}^{-1}, (v) and propagate back to the detector plane, $\mathcal{F}_F^{-1}$, [20]

$$\pi_m^F = \mathcal{F}_F^{-1}\pi_{WF}^{-1}\hat{\pi}_m\pi_{WF}\mathcal{F}_F \,. \tag{2.2.9}$$

Replacing the Fresnel support and modulus constraint operators in the CDI iterative algorithms, the analogous forms are obtained for use in FCDI [22],

$$(ER) : \rho_{k+1} = \pi_s^F\pi_m^F\rho_k \,, \tag{2.2.10}$$

$$(HIO) : \rho_{k+1} = [1 + (1+\beta)\pi_s^F\pi_m^F - \pi_s^F - \beta\pi_m^F]\rho_k \,. \tag{2.2.11}$$

where ρ_k is the k'th iterate of the samples ESW.

2.2.2 White-Field Recovery

In contrast to CDI, FCDI requires that the white-field (or diverging illumination) incident on the sample to be known, in order to correctly separate its features from those of the sample's ESW. Here an iterative algorithm is described which retrieves the phase of the white-field, demonstrated in Quiney *et al* [7] and Reference [12], the notation from Reference [12] is used.

This algorithm uses the Fresnel free space propagator Equation 2.2.2, and requires the measurement of the far-field intensity of the diverging beam, the size of the pupil function of the focusing optic, it's focal length and the distance from the focal plane to the detector. The procedure uses propagation between three planes perpendicular to the beam propagation direction: the lens plane at z_L; the focal plane at z_F; and the detector plane at z_D. We denote the coordinates in the lens plane by $\boldsymbol{\rho}_l$, in the focal plane by $\boldsymbol{\rho}_f$, and in the detector plane by $\boldsymbol{\rho}_d$. The iterative determination of the white-field follows the propagation cycle $z_D \to z_F \to z_L \to z_F \to z_D$.

The illumination in the lens plane and the detector can respectively be written as,

$$\psi(\boldsymbol{\rho}_l, z_L) = P(\boldsymbol{\rho}_l)\exp\left[-\frac{i\pi\boldsymbol{\rho}_l^2}{\lambda z_{LF}}\right] , \tag{2.2.12}$$

and

$$\psi(\boldsymbol{\rho}_d, z_D) = Q(\boldsymbol{\rho}_d)\exp\left[+\frac{i\pi\boldsymbol{\rho}_d^2}{\lambda z_{FD}}\right] , \tag{2.2.13}$$

, where z_{LF} and z_{FD} are the lens to focus, and focus to detector distances respectively. $P(\boldsymbol{\rho}_l)$ and $Q(\boldsymbol{\rho}_d)$ contain only the slowly varying components of $\psi(\boldsymbol{\rho}_l, z_L)$ and $\psi(\boldsymbol{\rho}_d, z_D)$ respectively, allowing the removal of rapidly varying phase components from the iterate within the reconstruction, which would typically inhibit the algorithm due to insufficient sampling [12]. The extent of the focusing optic typically a Fresnel zone plate, is used as the support.

For a Freznel zone plate X-ray illumination, assuming zero perturbation of the white-field being perfectly spherical at the detector, gives a good starting guess of the solution [12],

$$Q(\boldsymbol{\rho}_d) = \sqrt{I(\boldsymbol{\rho}_d)}\,, \tag{2.2.14}$$

where $I(\boldsymbol{\rho}_d)$ is the measured data.
The iterative algorithm in order of operations is,

Propagate from Detector to Focus	$\psi(\boldsymbol{\rho}_f, z_F) = A(\boldsymbol{\rho}_f, z_{DF})\mathcal{F}^{-1}\left[Q(\boldsymbol{\rho}_d)\right]$
Propagate from Focus to Lens	$\mathbf{P}'(\boldsymbol{\rho}_l) = -i\exp\left[ikz_{FL}\right]\mathcal{F}^{-1}\left[B(\boldsymbol{\rho}_f, z_{FL})\psi(\boldsymbol{\rho}_f, z_F)\right]$
Apply Support Constraint	$\mathbf{P}(\boldsymbol{\rho}_l) = \pi_s P'(\boldsymbol{\rho}_l)$
Propagate from Lens to Focus	$\psi(\boldsymbol{\rho}_f, z_F) = A(\boldsymbol{\rho}_f, z_{LF})\mathcal{F}\left[P(\boldsymbol{\rho}_l)\right]$
Propagate from Focus to Detector	$Q'(\boldsymbol{\rho}_d) = -i\exp\left[ikz_{FD}\right]\mathcal{F}\left[B(\boldsymbol{\rho}_f, z_{FD})\psi(\boldsymbol{\rho}_f, z_F)\right]$
Apply Modulus Constraint	$Q(\boldsymbol{\rho}_d) = \pi_m Q'(\boldsymbol{\rho}_d)$

To the already defined operator notation we may add the notation $\pi_p^{ij} = -i\exp\left[ikz_{ij}\right]$. The white-field recovery algorithm can then be written as a single expression,

$$Q_{k+1} = \pi_m \pi_p^{FD} \mathcal{F} \pi_B^{FD} \pi_A^{LF} \mathcal{F} \pi_s \pi_p^{FL} \mathcal{F}^{-1} \pi_B^{FL} \pi_A^{DF} \mathcal{F}^{-1} Q_k\,. \tag{2.2.15}$$

2.3 Noise in Diffraction Imaging

In the measurement of a diffraction pattern in a CDI experiment, various sources of noise are present. Typically the noise is dominated by beam scatter from sources other than the sample, shot-noise (photon counting statistics), background photons, and noise generated by the X-ray detection system for example a charge coupled device (CCD) [12, 1].
Sources of beam X-ray scattering other from that of the sample, we refer to as alien scattering. Alien scattering includes beam scattered photons from the sample substrate, incoherently illuminated parts of the sample, air scatter, and other obstacles in the beam path such as upstream pinholes [1].
The inherent shot-noise is due to the probability that a diffracted photon will arrive in a pixel. This probablity follows a Poisson distribution, and so the expected uncertainty in a measurement of m photons, will have a standard deviation or noise $\sqrt{m}$ [1, 2]. The Poisson distribution for r events of a measured photon in a given pixel is given by [24],

$$P(r) = \frac{m^r e^{-m}}{r!}\,. \tag{2.3.1}$$

For the X-ray photons incident on a pixel, the fraction of photons detected is given by the quantum efficiency of the detector [12],

$$q(E_\nu) = \frac{N_\nu^d}{N_\nu}\,, \tag{2.3.2}$$

where E_v is the photon energy (at frequency ν), N_ν^d is the number of detected photons and N_ν is the number of incident photons. The detected photons travelling through the layers of a CCD, can lose energy through a number of different mechanisms. In photon energy range 30 eV to 20 keV these mechanisms are typically Compton scattering, fluorescence and the photoelectric effect. The main form of energy dissipation is from photoelectric effect which refers to creation of a number of electron-hole pairs proportional to the incident photon energy. For silicon the energy ζ to produce one electron-hole pair and thus an detectable electron is approximately 3.65 eV [12, 25].

The number of detected electrons N_{e^-} is therefore [12],

$$N_{e^-} = \frac{qN_\nu E_\nu}{\zeta}\,. \tag{2.3.3}$$

In addition to electrons generated by the incident photons, a large amount of CCD detectors have further electronic noise, read-noise and dark-current, which along with background photons contribute to background noise. The read-noise $N_R\,[e^- rms]$ can be minimised by using slower readout speeds [12]. The dark-current $N_D\left[\frac{e^-}{pixel\times s}\right]$, originates from thermal excitation of electron-hole pairs [1, 2], and can be minimised by cooling or using shorter exposure times for each data-frame [12]. CCD detectors also degrade and get radiation damage with time and the dark-current in these regions may not be the same as in undamaged ones [1].

When undertaking diffraction imaging experiments it is important to understand the relation between incident X-ray photons and measurement from a CCD. In each pixel of the CCD, photon counts are converted to analog-to-digital-units (ADUs) which are the internal units of the CCD camera [12]. Conversion of electrons to ADUs is dependent on the gain $g\left[\frac{e^-}{ADU}\right]$of the CCD camera, which is typically a floating number that can be calibrated. The number of ADUs in a given pixel N_A, as a function of the number of incident photons N_ν, is given by [12],

$$N_A = \frac{1}{g}\left(\frac{qN_\nu E_\nu}{\zeta} + N_R + N_D\right). \tag{2.3.4}$$

The pixelwise ADU-values will determine the final data frame (or frames), and will consist of the desired signal, and inherent noise that has to be dealt with prior to reconstructing the sample.

2.3.1 An Example of Measured Data

Here we demonstrate an example illustrated in Reference [12]. The data was aqcuired at beamline 2-ID-B of the Advanced Photon Source, and is for an FCDI experimental setup. This example is used in Chapter 4, where the details of an experimental setup are described. From the data collected, the gain and the pixelwise ADU values are retrieved. The detector used was an *in vacuo* Princeton Instruments PI-MTE CCD [26], with 2048x2048, 13.5μm pixels.

In Figure 2.3.1, a histogram of the lowest ADU counts, collected in a 1 second interval, for an illumination of diverging 2.535 keV X-rays is shown. The green curve corresponds to a histogram of raw data and the blue curve to a histogram of the background noise. The dark-current contribution is neglected due to the short exposure time. In addition the contribution from background photons was negligible and the background noise therefore consists primarily of read-out noise. Hence when the background noise is subtracted from the data, the resulting ADU counts (red curve) are proportional to the number of incident photons on the detector.

The detector quantum efficiency is $q = 82\%$ (at the X-ray energy 2.535 keV) [26], and $\zeta = 3.65$ eV so the above equations yields on average $N_e^- = 570$ electrons per incident X-ray photon. According to the single photon peak in Figure 2.3.1, one X-ray photon converts to $N_A = 157$ ADU counts. The corresponding gain is thus $g \approx 3.63\left[\frac{e^-}{ADU}\right]$. We also note that the single energy peak above the underlying histogram distribution is approximately Gaussian distributed [24, 27],

$$P(x) = \frac{1}{\sigma\sqrt{2\pi}} e^{-\frac{(x-\mu)^2}{2\sigma^2}}, \tag{2.3.5}$$

with a mean $\mu \approx 157$ ADUs of standard deviation $\sigma \approx 30$ ADUs. Furthermore the background noise histogram may also be approximated by a Gaussian distribution with mean $\mu \approx 210$ ADUs of standard deviation $\sigma \approx 14$ ADUs.

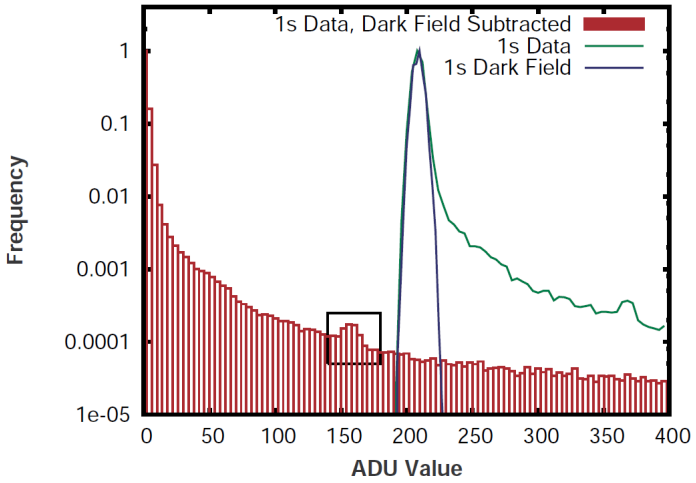

Figure 2.3.1: Histogram of ADU counts for a single 1 second (1s) frame of data after background subtraction has taken place. The black box indicates the first photon peak, used to calculate the gain ratio. The green curve shows the un-adjusted data frame, which includes the background noise. The blue curve is the histogram for the background noise. *Figure reprinted with permission from [12], courtesy of C. T. Putkunz.*

Chapter 3

Noise Simulation for Coherent Diffractive Imaging

This chapter reproduces the procedure and a subset of the results obtained by Williams *et al.* [1, 2, 3]. This provides a basis for extending the procedure to FCDI in Chapter 4 and allow a comparison of noise effect's in CDI and FCDI. The procedure by Williams *et al.* [1, 2, 3] shows how to simulate a diffraction intensity measurement including experimental realities and noise in diffraction imaging, our usage of this procedure are described in Section 3.1. Varying ranges of Poisson distributed shot-noise, alien scattering from the incident x-ray beam, and noise generated in a typical CCD detector are included in our analysis. The behaviour of the iterative algorithms ER and HIO (Section 2.1.1) in reconstructing phase from the noise added diffraction patterns are investigated in Section 3.2. Conclusions are given in Section 3.3.
The simulations were developed in C++ by the author using as a foundation code from the "Nadia Software Project" a software for electron and X-ray diffractive imaging [28].

3.1 Experiment simulation

Here we describe how to simulate measurement data, with different amount of shot-noise, alien scattering, or background noise level. (The parameters chosen explore a range of possible experimental scenarios of interfering noise according to [1, 2, 3].)
Once the level of noise from the three preceding sources has been chosen a signal-to-noise ratio (SNR) was calculated according to

$$\mathrm{SNR} = \frac{\sum_{n=1}^{N} I(\boldsymbol{\rho}_d)}{\sum_{n=1}^{N} \left(\sqrt{I(\boldsymbol{\rho}_d)} + P(\boldsymbol{\rho}_d) + B(\boldsymbol{\rho}_d) \right)}, \tag{3.1.1}$$

where $I(\boldsymbol{\rho}_d)$ is the intensity in ADUs at detector pixel coordinate $\boldsymbol{\rho}_d$, $P(\boldsymbol{\rho}_d)$ is additional signal due to alien scattered x-ray beam photons in ADUs, and $B(\boldsymbol{\rho}_d)$ is the remaining background level after a background subtraction in ADUs arising from the detector and electronics, the sums are carried out over all N pixels.

To simulate the data with a wide range of SNR the following procedure was employed:

(i) To simulate an arbitrarily scaled exit-surface wave (ESW) $\psi(\boldsymbol{\rho}_s)$, an 256×256 pixel object density projection as seen in Figure 3.1.1(a) was selected. This object was chosen to have a non-symmetric shape to determine when twin-mixing occurs in reconstruction. It was created by first having zero value outside and maximum inside the boundaries of object, then convolved to give smoothened edges. Every real number at each pixel of this 256×256 pixel object array, were then transformed to a complex number whose magnitude corresponds to the initial real number, yielding the arbitrarily scaled ESW $\psi(\boldsymbol{\rho}_s)$.

(ii) A fast Fourier transform (FFT) of the arbitrarily scaled ESW $\psi(\boldsymbol{\rho}_s)$ was performed. The modulus squared of each complex number in the array gave the diffracted intensity pattern $|\psi(\boldsymbol{\rho}_d)|^2$. The sum of the intensity over all pixels of this arbitrarily scaled diffraction intensity $\sum_{n=1}^{N} |\psi(\boldsymbol{\rho}_d)|^2$, was then converted to correspond to any selected total number of measured photons M to be present in a measurement, between the range $9 \times 10^4 - 10^9$ photons. Summing the diffraction intensity over all pixels, then dividing by the selected number of total photons, yields

$$\Xi = \frac{\sum_{n=1}^{N} |\psi(\boldsymbol{\rho}_d)|^2}{M}. \tag{3.1.2}$$

Every pixel value at coordinate $\boldsymbol{\rho}_d$ in the arbitrarily scaled diffraction intensity $|\psi(\boldsymbol{\rho}_d)|^2$ were divided by this quantity Ξ, yielding a probabilistic value of photons at every pixel $|\psi^M(\boldsymbol{\rho}_d)|^2$. Thus $\sum_{n=1}^{N} |\psi^M(\boldsymbol{\rho}_d)|^2 = M$.

(iii) To include the effects of shot-noise, each pixel in the scaled diffraction intensity $|\psi^M(\boldsymbol{\rho}_d)|^2$, was replaced with a value $|\psi^S(\boldsymbol{\rho}_d)|^2$ drawn from a Poisson distribution with mean $|\psi^M(\boldsymbol{\rho}_d)|^2$ and uncertainty $\sqrt{|\psi^M(\boldsymbol{\rho}_d)|^2}$.
Additional shot-noise due to alien scattering was included in this step, by assuming in each pixel a spatially uniform Poisson distributed number of alien photons with mean A here between 0.0005, 0.0013, 0.005, 0.05, 0.5. Thus we added a number from this Poisson distribution with mean A and standard deviation $\sqrt{A}$, to each pixel value of $|\psi^S(\boldsymbol{\rho}_d)|^2$.

(iv) To simulate what happens in an actual experiment the diffraction intensity was converted from photons to an integer number of 'analog to digital units' (ADUs). This conversion may be understood by viewing a histogram of experimental diffraction data, that the single energy photon peak is roughly Gaussian distributed (see Figure 2.3.1 for example). In accordance with experimental diffraction data used in References [1, 2, 3], the Gaussian distribution were chosen to have a mean of 324 ADUs with standard deviation 32 ADUs. Thus the number of photons in each pixel $|\psi^S(\boldsymbol{\rho}_d)|^2$, was replaced by $|\psi^S(\boldsymbol{\rho}_d)|^2$ summed numbers from this Gaussian distribution. The resulting value of ADUs in each pixel is rounded to an integer number of ADUs, and possible negative values were set to zero.
The resulting measurement intensity is $I(\boldsymbol{\rho}_d)$, accounting for the measured sample scattered photons, and $P(\boldsymbol{\rho}_d)$ accounting for any additional intensity caused by alien scattered photons, which are used in the calculation of SNR (Equation 3.1.1). An example of the steps until here with 9×10^4 photons measured without including alien scatter can be seen in Figure 3.1.1(b), and with additional alien scattered photons in each pixel for Poisson mean $A = 0.05$ in Figure 3.1.1(c).

(v) To simulate background noise all aspects of the CCD that gives rise to this background was combined. Through a fit to experimental diffraction data the background distribution is seen to be approximately Gaussian (see Figure 2.3.1 for example). In accordance to data used in References [1, 2, 3] this distribution were chosen to have a mean of 1000 ADUs with standard deviation 27 ADUs. This background scales with exposure time, corresponding to the time in which 9×10^4 photons are measured [1, 2, 3]. A number were added from this Gaussian distribution to $I(\boldsymbol{\rho}_d)$ at each pixel. To provide differing amount of background-noise level, a certain percentage 0-100% of the Gaussian mean (1000 ADUs) were subtracted from each pixel, and any resulting negative values were set to zero, the remaining background distribution is $B(\boldsymbol{\rho}_d)$ used in the SNR calculation (Equation 3.1.1). No rounding to nearest integer was performed, this was done so that very small values of the background relative to a photon's integer ADU conversion level in step (iv) may be explored [2]. An example are seen in Figure 3.1.1(d) of the steps until here for diffraction data with 9×10^4 measured photons, no included alien scatter and a 0% subtracted background.

The utility of simulating diffraction data from scratch rather than adding noise to an existing data set, is that one can create a true ESW to compare the reconstruction to. This was done by

following steps (i-ii) that is with no included noise. A multiplication were then performed by a factor of $324\left[\frac{\text{ADU}}{\text{photon}}\right]$, to be in the same scale as the analog-to-digital converted noise simulated diffraction data obtained by step (i-v) [1, 2]. Furthermore a FFT back to real-space was done to generate the true ESW seen in Figure 3.1.2.

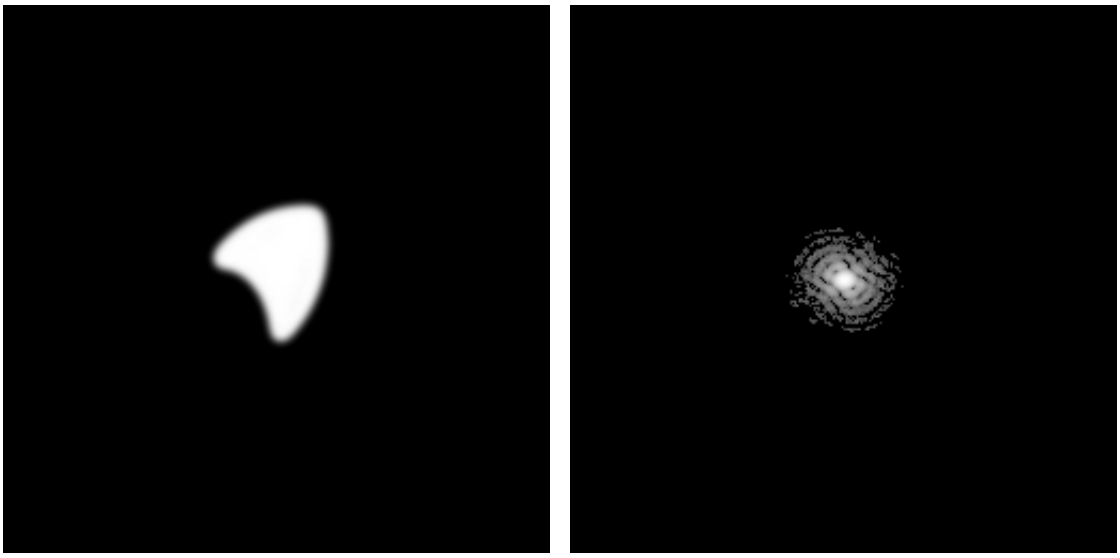

(a)

(b)

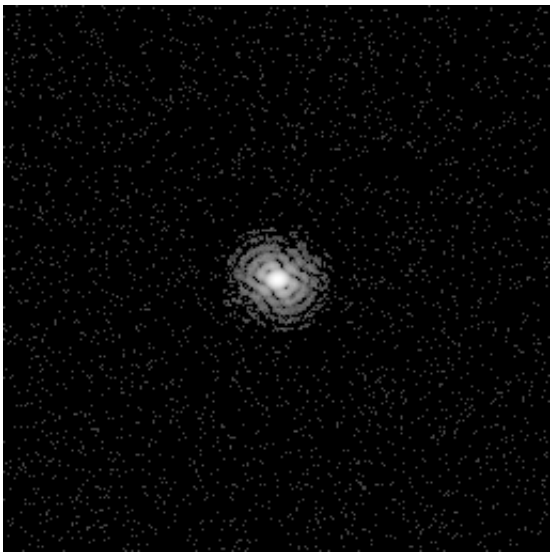

(c)

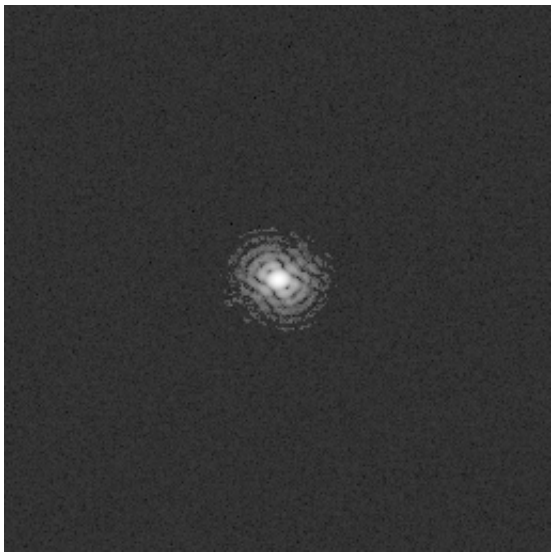

(d)

Figure 3.1.1: Examples of the simulation of measurement data with different sources of noise for the procedure described in Section 3.1.
(a) The selected object density in step (i).
(b) The simulated diffraction data after steps (i-iv) with a choice of 9×10^4 photons (log-scale).
(c) Additional alien scattering to (b) with Poisson mean of 0.05 photons per pixel (log-scale).
(d) After adding background noise to (b) without background subtraction (log-scale).

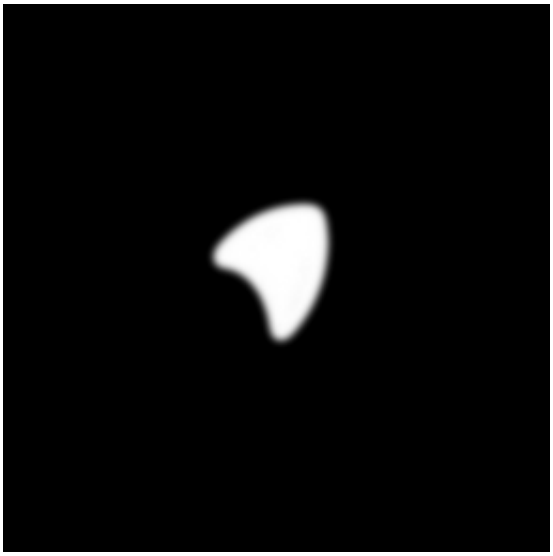

Figure 3.1.2: The true ESW generated as described in Section 3.1 used for comparison to reconstructions in Section 3.2.

3.2 Reconstructions

Simulated diffraction data with various sources and levels of noise was generated according to the method described in the previous section. Here the results on the quality of reconstructions are examined, in the presence of varying noise levels of three different types: photon number (Section 3.2.1), alien scattering (Section 3.2.2) and background noise (Section 3.2.3). The iterative phase retrieval algorithms tested are ER and HIO (described in Section 2.1.1).

For each of the three types of noise simulation the following procedure was followed: the true ESW and the simulated diffraction data were generated as 256×256 pixel arrays, and reconstructions were carried out in the same array size. The real-space support used was 70×80 pixels. A HIO parameter value $\beta = 1$ (this value was chosen because it yields good convergence in HIO [1]). The standard procedure was to perform five reconstructions by 500 iterations for each algorithm at each noise level. Each of the five reconstructions started with a different set of random phase for the simulated diffraction data, within the range $\pm 0.2\pi$ for each pixel. A convention is to regard ρ_k as the iterate, and $\pi_m \rho_k$ as an estimate of the ESW that is a potential solution [1]. However for this Chapter we investigate the iterate ρ_k in accordance with References [2, 3].

At each noise level in diffraction data and reconstruction by ER and HIO, the following error metrics are reported:

The error between magnitude of the best reconstructed iterate $|\rho^1_{500}|$ (after an iteration $k = 500$), and magnitude of the true ESW $|O|$, refered to as the fidelity [2, 3],

$$\xi^0_1 = \frac{\sum_{n=1}^{N} \left[|\rho^1_{500}(\boldsymbol{\rho}_s)| - |O(\boldsymbol{\rho}_s)| \right]^2}{\sum_{n=1}^{N} I(\boldsymbol{\rho}_d)} . \tag{3.2.1}$$

The error between magnitude of the best reconstructed iterate $|\rho^1_{500}|$, and magnitude of the second best iterate $|\rho^2_{500}|$, which one may refer to as the reproducibility [2, 3],

$$\xi^2_1 = \frac{\sum_{n=1}^{N} \left[|\rho^1_{500}(\boldsymbol{\rho}_s)| - |\rho^2_{500}(\boldsymbol{\rho}_s)| \right]^2}{\sum_{n=1}^{N} I(\boldsymbol{\rho}_d)} . \tag{3.2.2}$$

The error metric between magnitude of solution $|\pi_m \rho^1_{500}|$, and magnitude of the iterate $|\rho^1_{500}|$, in real space [1],

$$\chi^2 = \frac{\sum_{n=1}^{N} \left[|\rho^1_{500}(\boldsymbol{\rho}_s)| - |\pi_m \rho^1_{500}(\boldsymbol{\rho}_s)| \right]^2}{\sum_{n=1}^{N} I(\boldsymbol{\rho}_d)} . \tag{3.2.3}$$

And the equivalent χ^2 error metric in reciprocal space [12, 20],

$$\chi^2_{reciprocal} = \frac{\sum_{n=1}^{N} \left[|\mathcal{F}(\rho^1_{500}(\boldsymbol{\rho}_s))| - \sqrt{I(\boldsymbol{\rho}_d)} \right]^2}{\sum_{n=1}^{N} I(\boldsymbol{\rho}_d)} , \tag{3.2.4}$$

where $\mathcal{F}$ is a Fourier transform. The five best reconstructions were ranked by the lowest $\chi^2_{reciprocal}$.

Different in Reference [1] are ξ^0_1, ξ^2_1 where they've used solution ($\pi_m \rho_{500}$) instead of iterate (ρ_{500}), however in this chapter we considered the iterate as they've done in Reference [2, 3]. The same conclusions about the correlation of ξ^0_1, ξ^2_1, χ^2 is infered in References [2, 3] and [1], that is regardless of considering the iterate or solution. In this chapter we compare the magnitude entities in ξ^0_1, ξ^2_1, χ^2 apart from References [1, 2, 3] where they've compared the complex entities. And comparison of magnitude instead of the complex values of the reconstructed iterates may have some effects on the error metrics values, and may be cause of some difference in results to References [1, 2, 3].
The error metrics calculated for Section 3.2.1-3.2.3 (where there is further explanation) comparing magnitude entities are shown in Figure 3.2.1. There is a problem with the error metrics ξ^0_1, ξ^2_1 since they are not always correctly calculated because the reconstructions may be displaced or are reconstructed as a twin image ("mirror image") [6] or a mixture of the twin images [2], and may not overlap. The tedious work of overlapping entities before calculation was not done here. The error metrics χ^2, $\chi^2_{reciprocal}$ assume already overlapping entities.
The original metric values from Reference [1] are shown in Figure 3.2.2, where overlapping complex entities are compared. The higher value of HIO metrics in Figure 3.2.1 may partly be due to that the iterate is not to be regarded as a solution and contains density outside of support, the HIO entities may have been dealt with differently in Reference [1], Figure 3.2.2. The ER algorithm do end with a support constraint and thus everything outside the support is zero, and ER error metrics shows better agreement with the results in Figure 3.2.2. The comparison of non-overlapping entities in Figure 3.2.1 seems to explain partly the deviations in ξ^0_1, ξ^2_1 from Figure 3.2.2. The HIO algorithm in particular may be more deviating as it is sensitive to for example the tightness of support. There may be some deviation due to that in the original work they've used a modified π_s.

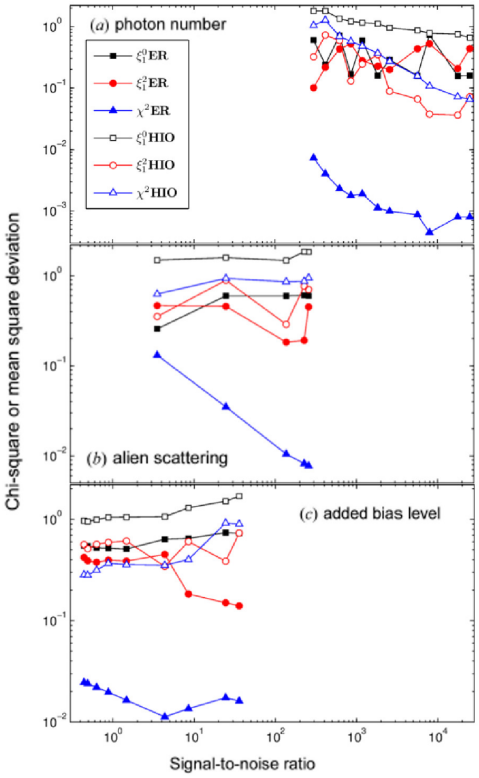

Figure 3.2.1: Scatter plots of ξ_1^0, ξ_1^2, and χ^2 against SNR for the three tests of noise level described in Section 3.2. (a) Photon number. (b) Alien scattering. (c) Background noise (or bias level). Lower values of all three quantitities indicate better agreement. Note the similarity with Figure 3.2.2 for the behaviour of the reliably calculated χ^2. Note ξ_1^0, ξ_1^2 are sometimes not valid since comparison of non-overlapping quantities occurs.

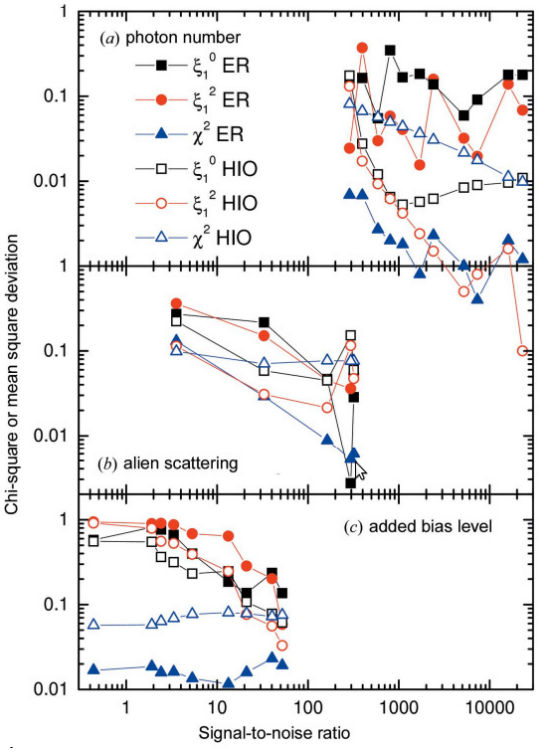

Figure 3.2.2: Scatter plots of ξ_1^0, ξ_1^2 and χ^2 against SNR for the original work in Reference [1] by equivalent three tests of noise level as described in Section 3.2. (a) Photon number. (b) Alien scattering. (c) Background noise. Lower values of all three quantitities indicate better agreement. Notice the behaviour of ξ_1^2 more closely resembles the behaviour of ξ_1^0 than does χ^2, revealing its importance as an indicator of a correct solution in the presence of noisy diffraction data.
Figure reprinted with permission from [1], courtesy of G. J. Williams.

3.2.1 Photon Number

Simulated diffraction data with varying number of measured photons between $9 \times 10^4 - 10^9$ were obtained by steps (i-iv) in Section 3.1, with SNR between 299 and 25172. The error metric values obtained for this range are shown in Figure 3.2.1(a). The reconstructed iterate magnitude for high shot-noise (SNR=299) and low shot-noise (SNR=25172) are shown in Figure 3.2.3. (All the simulated diffraction data and the reconstructed iterates are shown in Appendix A.1).
A qualitative observation is that the HIO algorithm obtains a better reconstruction as SNR increases, where as the reconstruction quality of the ER algorithm does not seem to vary as much, similar to the corresponding results in References [1, 2], and in agreement with the behaviour of ξ_1^0, ξ_1^2 in Figure 3.2.2(a) from Reference [1]. There is good similarity with the trend of χ^2 for ER and HIO in Figure 3.2.1(a), 3.2.2(a), although the possible differences in ξ_1^0, ξ_1^2 have been discussed already. However we observed a similar trend as in Figure 3.2.2(a), through qualitative comparison of the involved entities in error metrics.
The higher value of χ^2 for HIO than ER in both Figure 3.2.1(a), 3.2.2(a) is deceiving since HIO has a better resemblance to the true ESW, infered by inspection in this work and the lower ξ_1^0 in Figure 3.2.2(a), suggesting that χ^2 is not an ideal metric for HIO [1].

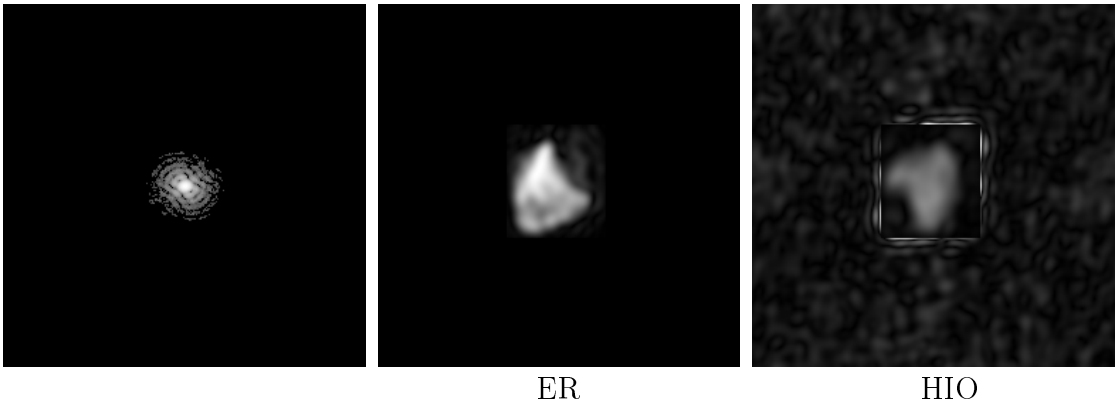

(a)

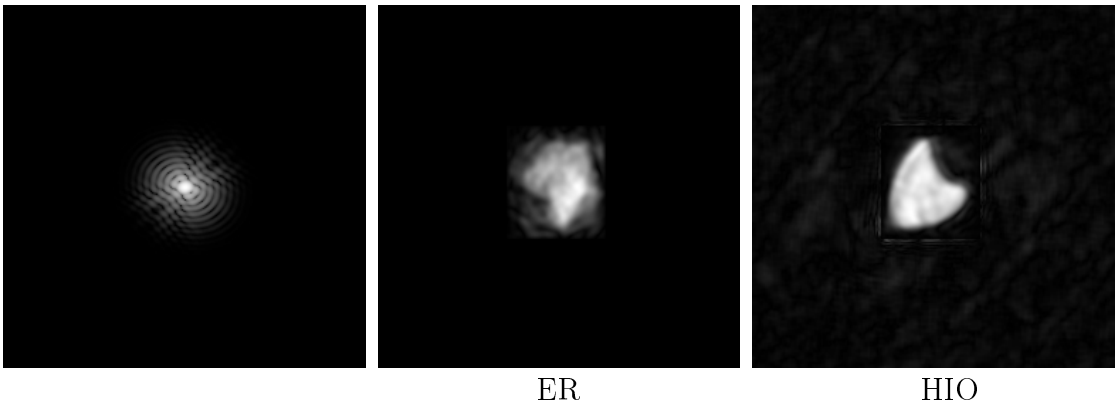

(b)

Figure 3.2.3: Magnitude of reconstructed iterate ($|\rho_{500}^1|$) from diffraction data that has only shot-noise inherent for measurements of (a) 9×10^4 photons, and (b) 10^9 photons, obtained by steps (i-iv) in Section 3.1. For both (a) and (b): diffraction data (left), ER iterate (middle), HIO iterate (right).
Here the distortion of the HIO reconstructed iterates due to the reconstructed "support-frame" and surrounding is evident (with the images normalised to their respective maximum value). For HIO the iterate is not regarded as a potential solution, but after an modulus constraint has been applied, making the outside support region diminish and is then regarded as a solution or a better reconstruction. By comparison ER has zero values outside support, and is much alike the solutions (that is when an modulus constraint have been applied to the iterate).

3.2.2 Alien Sources of X-ray Scatter

We chose the simulated data with 9×10^4 measured photons having a high amount of shot-noise, for the inclusion of alien scattered photons. (This case was chosen due to experimental congruence in Reference [1]). By the procedure of Section 3.1, diffraction data was simulated by steps (i-v) and including in step (iii) a Poisson distributed mean number of alien photons between 0.0005-0.5 per pixel. This yielded simulated diffraction data with a SNR between 258-3.53. The error metric values obtained for this range are shown in Figure 3.2.1(b). The diffraction data and the reconstructed iterate magnitude, for high alien scattering (SNR=3.53) and low alien scattering (SNR=258) are shown in Figure 3.2.4. (All the simulated diffraction data and the reconstructed iterates are shown in Appendix A.2).
The amplitude variations and 'bluriness' in the reconstructed iterate were observed for diffraction data of 9×10^4 measured photons with inherent shot-noise in Section 3.2.1. Here the additional shot-noise due to alien photons gives a real-space result with an even noisier appearance. Again there are already explained differences in Figure 3.2.1(b) from the original work in Figure 3.2.2(b), though again χ^2 shows similar behaviour, especially for ER. However qualitative comparison of the involved entities in error metrics implies a similar trend as in Figure 3.2.2(b).

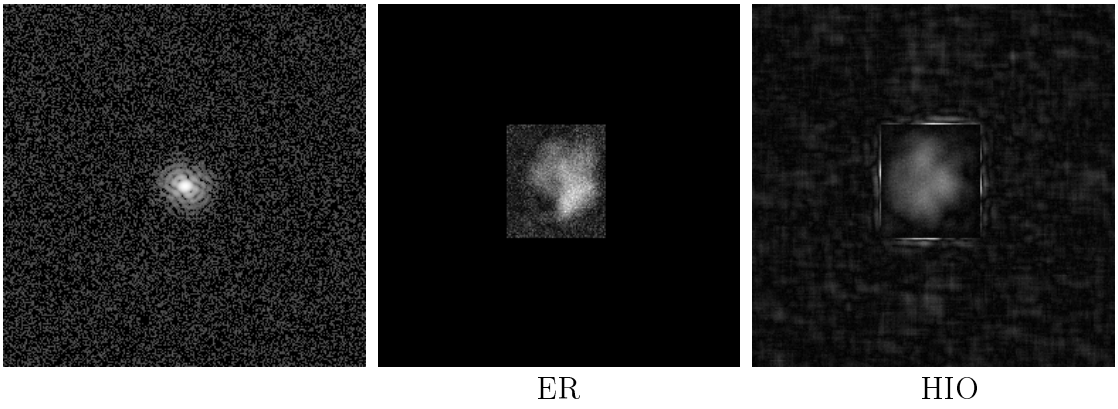

(a)

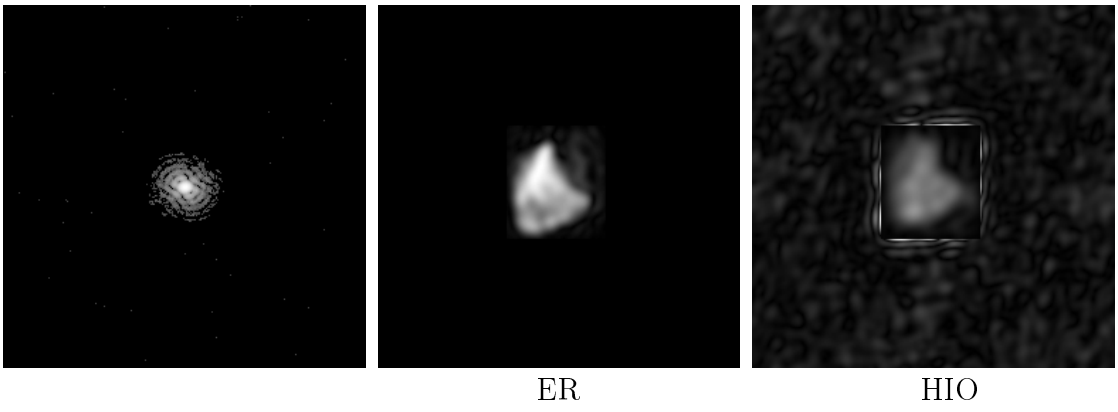

(b)

Figure 3.2.4: Magnitude of reconstructed iterate ($|\rho^1_{500}|$) from diffraction data with inherent shot-noise for 9×10^4 photons and additional shot-noise from a Poisson distributed mean of alien photons, obtained by steps (i-iv) of Section 3.1. (a) Poisson mean of alien photons 0.5 (SNR=3.53), and (b) Poisson mean of alien photons 0.0005 (SNR=258). For both (a) and (b): diffraction data (left), ER iterate (middle), HIO iterate (right).

3.2.3 Incomplete Background Subtraction

Here we again use the simulated data with 9×10^4 measured photons and including the inherent background noise, created by steps (i-v) of Section 3.1. Subtracting 0-100% of the background mean from each pixel gives diffraction data with a SNR between 0.442 and 35.92. The error metric values obtained for this range are shown in Figure 3.2.1(c). The diffraction data and reconstructed iterate for 0% background subtraction (SNR=0.442) and 100% background subtraction (SNR=35.92), are shown in Figure 3.2.5. (All the simulated diffraction data and their respective iterates are shown in Appendix A.3).
One can clearly see that an incomplete background subtraction has a quite different effect on the iterate than alien photon shot-noise of Section 3.2.2. High levels of alien scattering resulted in a generally more 'noisy' image, by instead adding high levels of background it arises an even 'noisier' real-space result with rapidly varying magnitude. The cause of this artifact can be seen as zero-magnitude dots in the reciprocal magnitude of the reconstructed iterate, in Figure 3.2.5(a) for example. These zero-magnitude dots are called phase-singularities or vortices, that are a stagnation problem and has been reported in Reference [29]. It can be seen in Appendix A.3, that these vortices appear in reciprocal space of the reconstructed iterates until at least 95% background subtracted, or for in each pixel about 50 ADUs of background noise, or $15\% (= 0.015 = \frac{50}{324})$ of the ADUs caused by a one photon event. This is in agreement with results of References [1, 2, 3]. Due to the good congruence with results of the original work, the definition is assumed to be the same as in Reference [2], where these vortices are defined to be comprised of a group of two-four adjacent pixels with near zero-amplitude points and a phase that changes rapidly by $2\pi n$ (n integer) - occuring as a loop around the group as traversed. Comparing Figure 3.2.1(c); 3.2.2(c), the similar behaviour of χ^2 is seen, possible differences of all error metrics have been discussed previously. In Figure 3.2.2 one may notice that the linear dependence of increasing ξ_1^0 with decreasing SNR is steeper for the case of added background than for the case of alien scattering. Thus an indication that the algorithms are less tolerant of a background level than they are to alien scattering. This result is at least qualatively seen in the reconstructed iterates of Appendix A.2, A.3. And also seen in the corresponding reconstructions of References [2, 3] which have the same tested noise ranges for alien scattering and background noise.

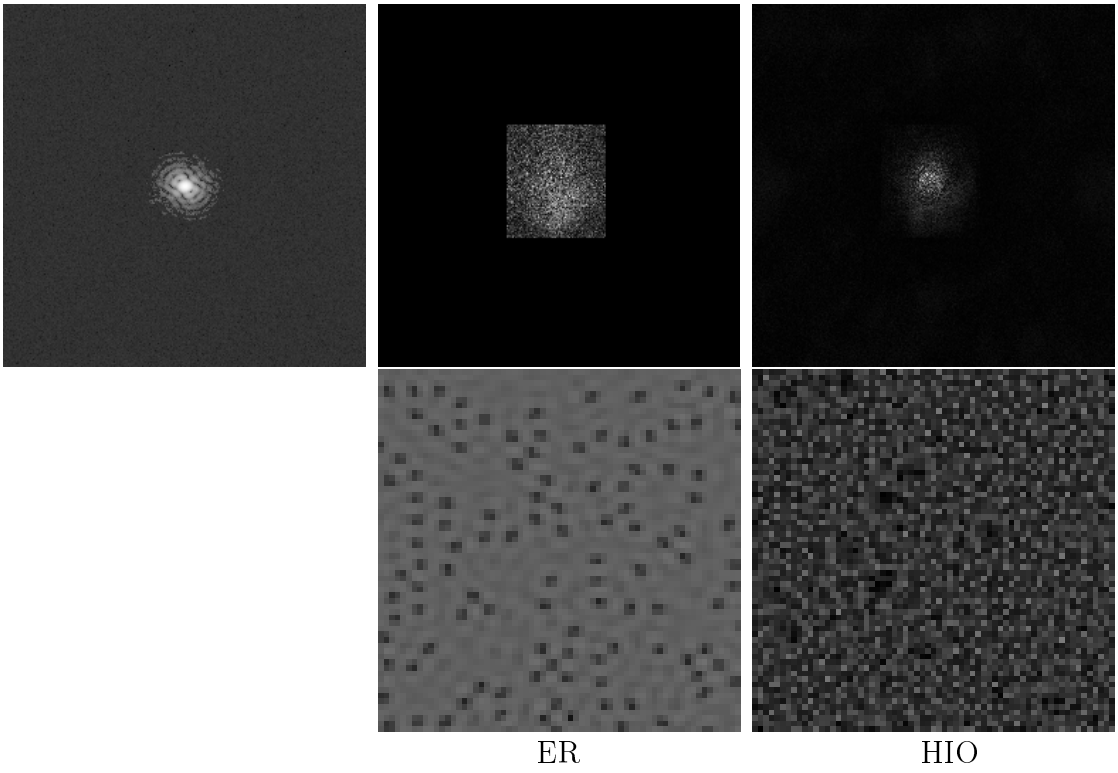

(a)

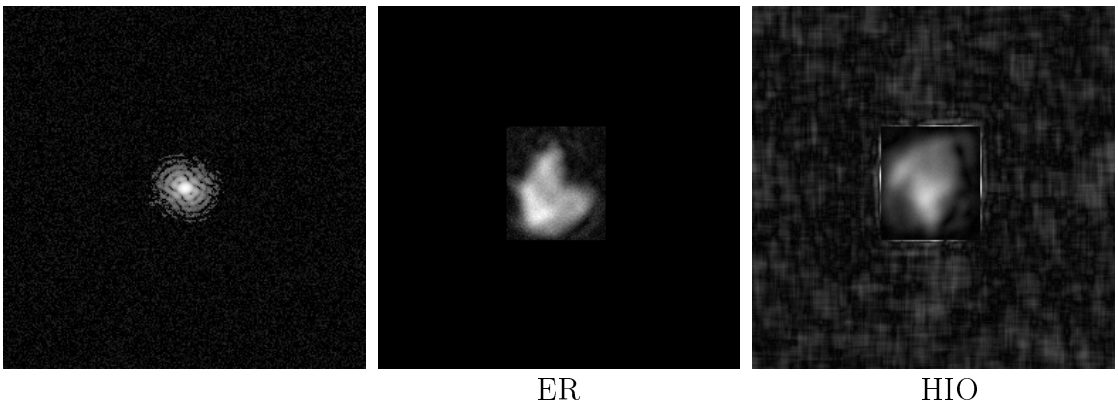

(b)

Figure 3.2.5: Magnitude of reconstructed iterate ($|\rho^1_{500}|$) from diffraction data with inherent shot-noise for 9×10^4 photons and inclusive background noise, and then subtracting different amount of background, (a) 0%, (b) 100%. Diffraction data obtained by steps (i-v) in Section 3.1. For both (a) and (b): diffraction data (left), ER iterate (middle), HIO iterate (right). In addition for (a) in second row we see the respective $|\rho^1_{500}|$ in reciprocal space zoomed in to a region of 64×64 in the upper left corner of the 256×256 array. Where zero-magnitude vortices are revealed. These are not apparent in case (b). Further explanation in text.

3.3 Conclusions

In Chapter 3 we examined the effects of noise for plane wave CDI. In particular the effects of varying number of measured photons, background levels, or alien beam scatter. The method and results obtained have been infered to be essentially the same as in the corresponding work by Williams *et al* [1, 2, 3]. However the intention was not to replicate all the original conclusions and discussion. Due to that the original work is more comprehensive in some aspects, for example by use of other phase retrieval algorithms and objects. Nevertheless the reproduction of key elements of the original work, is a validation of the method and main results.
The larger ranges of noise from different sources encompassed in References [1, 2, 3], is understood to be approximations of worse scenarios, in agreement with actual experimental data examined in References [1, 2, 3].

For the wide range of shot-noise examined, increasing number of measured photons and thus an increasing SNR, for the HIO algorithm, indicates a better agreement between the reconstructed iterate and the true ESW. Although the worse reconstruction fidelity of ER does not show much improvement with more measured photons.
Large amounts of alien photons seems troublesome, yielding a noisier appearance of the reconstruction, but if it's presence is not overwhelming, it does not yield a much notable impact, in agreement with References [1, 2]. It was assumed that the alien scattering occured with uniform probability over the detector. One might ask what effect a spatially non-uniform probability may have, for example with "contaminated" diffraction data where some intensity is measured from an interfering crystal, like a metal contaminant or the experimental apparatus [2].
Background noise is more harmful to the reliability of the reconstruction, causing vortices for less than 95% background subtracted, in agreement with References [1, 2, 3]. These vortices gives rise to a rapidly varying magnitude of the real-space magnitude, which might be mistaken for actual physical phenomena. As such, care should be taken to perform a good background subtraction [1, 2].
Interestingly when all the background has been subtracted, but the remaining variation of the Gaussian mean has not been removed (thresholded), the reconstructions becomes more similar to the case of alien scattering. This is reasonable since as the subtracted level nears the mean of the Gaussian distributed background, some pixels are reduced to zero while their neighbors still possess signal [3].
Several strategies may be employed to enchance the quality of the reconstructions presented here. For example the HIO algorithm is sensitive to the tightness of the support [1]. In addition it should be noted that the results of the noise simulation method used here, may depend to some extent of the real-space object chosen. We used a single compact object with an asymmetric shape and smooth edges. This object are similar but not identical to the one used in References [1, 2], and a different object is used in Reference [3]. It's also important to note that a mixture of ER and HIO has shown to be particularly effective, with the combination providing a better reconstruction than either algorithm alone [1, 2, 29].

Overall Chapter 3 shows agreement with the corresponding work of References [1, 2, 3], in regard to the reconstructions and conclusions. Noteworthy is the similarity of the reconstructions shown in Appendix A with the corresponding ones in Reference [2]. Also there is agreement in the χ^2 trends. Additionally it is noted that $\chi^2_{reciprocal}$ (Equation 3.2.4) overlaps (though with a factor larger for the HIO errors) with χ^2 (calculated in real space), so that either one may be used. However in Figure 3.2.1 the results of ξ_1^0, ξ_1^2 were not reliable though differences to the original work, Figure 3.2.2, were discussed. A main conclusion of the original work is the correlation between ξ_1^0 and ξ_1^2 (seen in Figure 3.2.2), and the usage of the calculable ξ_1^2 and χ^2 for a stronger identification when a good estimate is found of the unknown truth ESW. This result is anticipated to be clearly seen in this work if ξ_1^0, ξ_1^2 were comparing overlapping entities, as misplaced reconstruction occur in CDI. For FCDI there is only a unique solution such that the reconstruction always appear in the same location. Thus for FCDI, analogous ξ_1^0, ξ_1^2 error metrics will compare overlapping entities.
We have in Chapter 3 infered that the main results of Williams *et al.* [1, 2, 3] has been reached. This will allow a comparison, to an analogous analysis, for the technique of FCDI in Chapter 4.

Chapter 4

Noise Simulation for Fresnel Coherent Diffractive Imaging

In this chapter we will use a real experiment as an example and basis for our simulation, along with how the data is gathered and treated in Fresnel coherent diffractive imaging (FCDI), which will be described in Section 4.1.
The procedure used in Chapter 3 is extended to a FCDI geometry, to simulate an ESW and it's measurement data with noise incorporating varying ranges of Poisson distributed shot-noise, and noise generated in a typical CCD detector, to be described in Section 4.2.
Behaviour of the iterative algorithms ER and HIO in reconstructing a sample from the noisy diffraction data are investigated in Section 4.3, and conclusions are given in Section 4.4.
The simulations were developed in C++ by the author with support from supervisors, using as a foundation the "Nadia Software Project" a software for electron and X-ray diffractive imaging [28]. The particular experimental data used as an example for this chapter was collected by C. T. Putkunz and co-workers and is described in Reference [12]. The analysis of simulation results was undertaken by the author with support from supervisors.

4.1 Experiment

Here we describe a typical experimental setup and how the data are treated and combined in FCDI. The details are from a real experiment taken from Reference [12]. This has been already partly described in the example of Section 2.3.1, holding some details about detector, measurement and inherent noise in example data.

4.1.1 Geometry & Parameters

Here we describe the experimental parameters that were used in the simulation, the schematic of a FCDI experiment is shown in Figure 4.1.1.

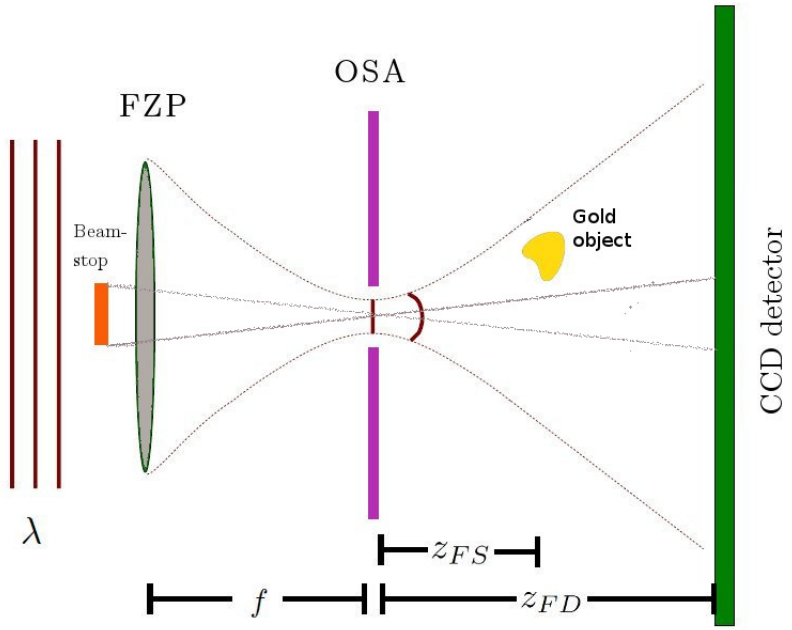

Figure 4.1.1: Illustration of a Fresnel CDI experimental geometry. Planar X-rays of wavelength λ are incident upon a Fresnel zone plate (FZP). A central beam stop and an order sorting aperture (OSA) obstruct all but the first order focus of the zone plate. The gold test sample (or object) is placed downstream of the focal plane, where the illuminating wave has a curved wavefront. A two-dimensional CCD detector are located at a far-field distance of the sample's scattering. The schematic is not to scale.

The wavelength of the illuminating X-rays was $\lambda = 4.891 \times 10^{-10}\,\mathrm{m}$ (2.535 keV). With a flux $F \sim 10^7[\frac{\mathrm{photons}}{\mathrm{s}}]$ of the incident beam across it's cross-section. The sample was 150 nm thick, homogenous gold. For gold at 2.535 keV the real and imaginary parts of the refractive index, $1 - \delta(\boldsymbol{\rho}, z) + i\beta(\boldsymbol{\rho}, z)$, will have values $\delta = 3.21 \times 10^{-4}$, and $\beta = 1.88 \times 10^{-4}$ [30].

The Fresnel zone plate (FZP) had a radius of $R = 80\,\mu\mathrm{m}$ and outer zone width $\Delta R = 50$ nm. It's focal length is given by [12],

$$f = \frac{2R\Delta R}{\lambda} = 16.3566\,\mathrm{mm}\,. \tag{4.1.1}$$

A central beam stop with radius $20\,\mu\mathrm{m}$ [31] was located in the inner region of the FZP.

The focal to sample distance was $z_{FS} = 1.45\,\mathrm{mm}$, the focal to detector distance was $z_{FD} = 0.9\,\mathrm{m}$, and the sample detector distance was thus $z_{SD} = 0.89855\,\mathrm{m}$ $(= z_{FD} - z_{FS})$.

A segment X_S at the sample will be magnified by a factor M to a segment X_D in detector plane by [12],

$$M = \frac{X_D}{X_S} = \frac{z_{FD}}{z_{FS}} = 621\,. \tag{4.1.2}$$

The beam radius at the sample was $7.092\,\mu\,\mathrm{m}$ $(= \frac{FZP\,radius}{f} \times z_{FS})$, and the beam-stop radius at the sample was $1.773\,\mu\,\mathrm{m}$ $(= \frac{Beam\,stop\,radius}{f} \times z_{FS})$.

With a sample chosen to be inside this illumination of radial length 5.319 μm, the Fresnel number will be at most

$$N_F = \frac{a^2}{\lambda \times z_{FS}} = \frac{(\frac{5.319\mu\mathrm{m}}{2})^2}{4.891\,\text{Å} \times 1.45\,\mathrm{mm}} = 9.973\,.$$

The beam will cover a radius on the detector of 326 pixels $(= \frac{FZP\,radius}{f} \times \frac{z_{FD}}{\Delta x_D})$ of pixel width $\Delta x_D = 13.5\,\mu\mathrm{m}$, and the beam-stop a radius of about 81.5 pixels $(\frac{Beam\,stop\,radius}{f} \times \frac{z_{FD}}{\Delta x_D})$.

The pixel size at the sample is, [12]

$$\Delta x_S = \frac{\lambda \times z_{SD}}{n \times \Delta x_D} = \frac{4.891\,\text{Å} \times 0.89855\ \text{m}}{2048 \times 13.5\,\mu\text{m}} = 15.9\ \text{nm},$$

where n is the number of pixels along a side of the CCD.
In the example of Reference [12], a different sample were used and $z_{FS} = 600\,\mu m$ and $z_{FD} = 0.5006\,m$. Nevertheless, experimental parameters derived from this real experiment provides a realistic scenario for our simulation. We use a similar simulated sample as for the CDI case (Chapter 3) so that results can be compared.

4.1.2 Combining CCD Data

To obtain better statistics a significant number of frames (short-time measurements) are collected, of the diffraction data (illumination with sample) and white-field data (illumination only).
Also the use of a diverging illumination on the sample gives a magnification of holographic region in the detector plane which makes the measurement sensitive to movement of sample and focusing optics. In addition for a curved wave-field it's phase varies continously across the sample and thus movement will distort, in contrast to a planar wave-field when the phase is continious across the sample. To sum data frames that are different due to sample motion, or any other varying source of noise, would result in an inaccurate FCDI reconstruction. (In Reference [32] they demonstrate an approach to ameliorate the effect of using uncorrelated frames due to sample motion). To determine the most correlated frames, one calculates a cross correlation curve of a single data frame against all other frames as [12, 22],

$$R_{ij} = \frac{\sum_{n=1}^{N} I_i(\boldsymbol{\rho}_d) \times I_j(\boldsymbol{\rho}_d)}{\sum_{n=1}^{N} I_i(\boldsymbol{\rho}_d) \sum_{n=1}^{N} I_j(\boldsymbol{\rho}_d)}, \tag{4.1.3}$$

where $\boldsymbol{\rho}_d$ is the pixel coordinate, and N is the number of pixels within the frame.
The cross correlation for the collected frames are shown in Figure 4.1.2. The poor cross correlation curve results from the high level of motion in the imaging system. A typical cutoff used for this data is about $R_{ij} = 0.99$, yielding about 100 frames that may be summed together.

Before a phase-retrieval algorithm can be applied to experimental data, the background noise in the data must be eliminated to minimize it's effect on the reconstruction. Data without X-ray illumination are collected to determine the background noise including the dark-current, readout noise and any source of photons not related to the beam. A number of background frames are collected and averaged, to reduce the uncertainty. For each of the selected correlated frames of the white-field and diffraction data, a background subtraction is carried out pixel by pixel. The stochastic nature of the background noise prevents this subtraction from being complete. Therefore a threshold is performed from the background subtracted data frame, where all values less than a certain number of ADU's are set to zero. As shown in for example Figure 2.3.1, the single-energy (2.535 keV) photon peak is clearly visible in the intensity histogram, the threshold should be chosen below this peak [12, 22].
After that the highly correlated frames have been selected, background subtracted and thresholded, the data are summed together. Some treated data from this example are shown in Figure 4.1.3.

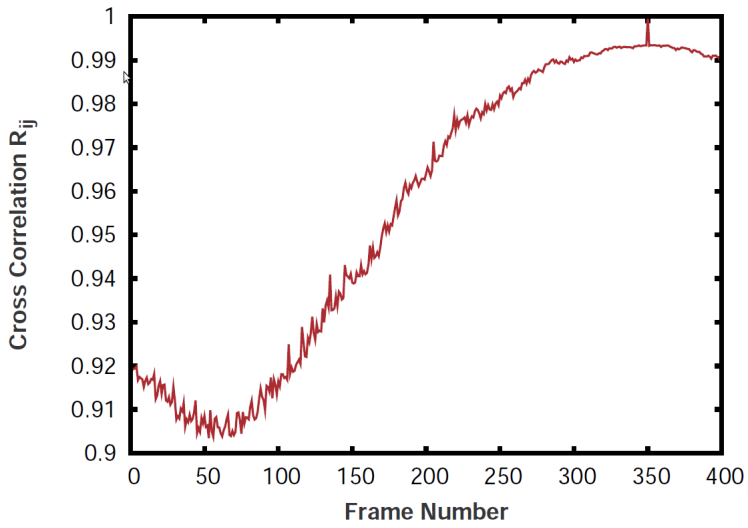

Figure 4.1.2: Cross correlation function, for 400 data frames collected. Frame 350 was used as a basis for the correlation. *Figure reprinted from [12], courtesy of C. T. Putkunz.*

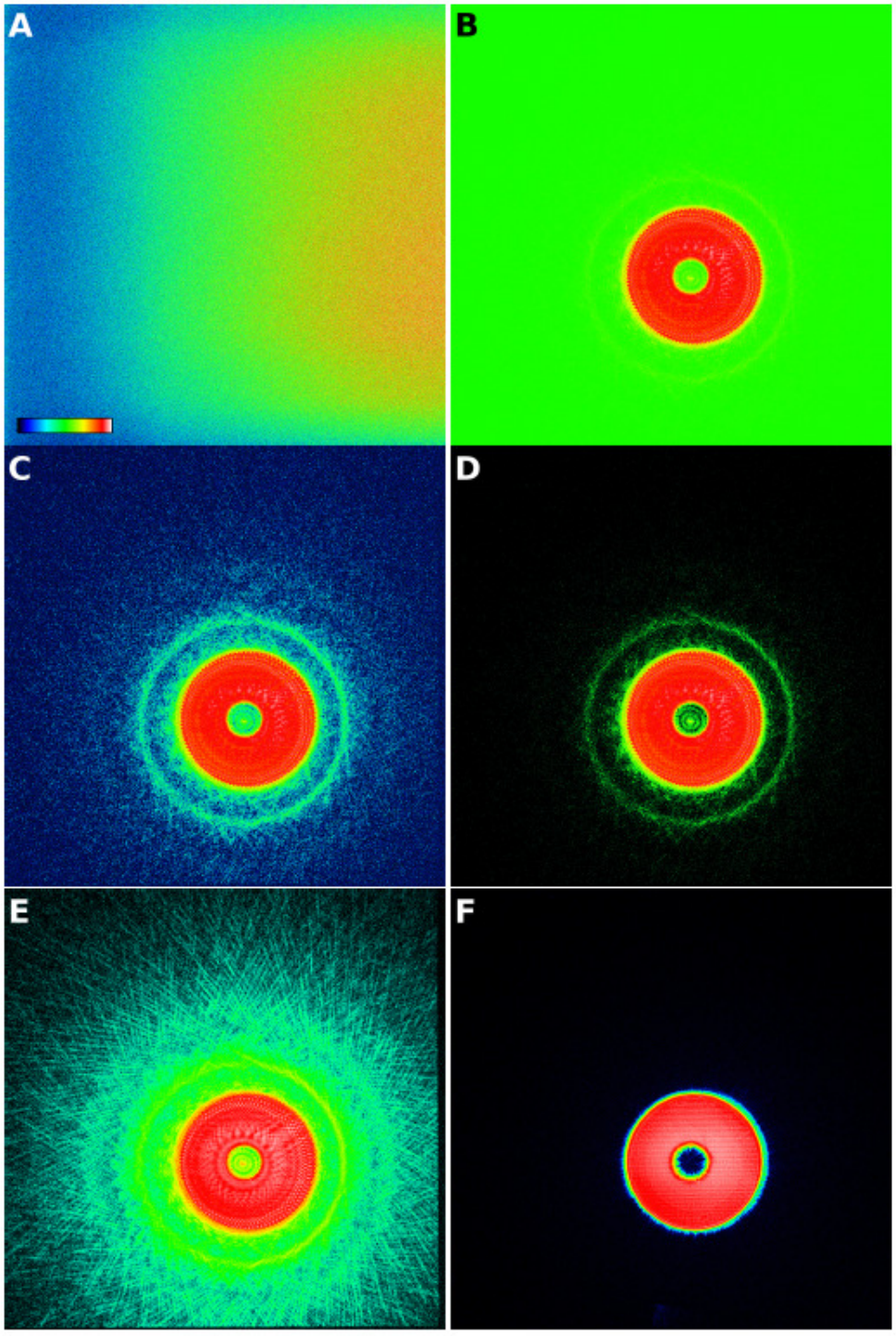

Figure 4.1.3: (A) Background image. (B) Raw single data frame. (C) Single data frame after background subtraction. (D) Single data frame after background subtraction and noise thresholding. (E) 100 combined diffraction data frames, each has been background subtracted and thresholded. (F) The white-field data frames corresponding to (E). Images (B) through (E) are shown in a logarithmic colour palette. *Figure reprinted from [12], courtesy of C. T. Putkunz.*

4.2 Experiment simulation

The procedure described here is similar to the one in Section 3.1, though extended to the methodology of FCDI. We build here on the experiment given in the previous section and describe our method to simulate measurements of diffraction and white-field data. In particular data that has different number of measured photons with inherent shot noise, and additionally varying levels of background noise. Once the level of noise from the two preceding sources had been chosen a signal to noise ratio (SNR) were calculated only for the diffraction data,

$$\mathrm{SNR} = \frac{\sum_{n=1}^{N} I(\boldsymbol{\rho}_d)}{\sum_{n=1}^{N} \left(\sqrt{I(\boldsymbol{\rho}_d)} + B(\boldsymbol{\rho}_d)\right)}, \tag{4.2.1}$$

where $\boldsymbol{\rho}_d$ is the pixel coordinate, $I(\boldsymbol{\rho}_d)$ is the number of measured photons converted to ADUs, and $B(\boldsymbol{\rho}_d)$ is the background in ADUs.

To generate the data with varying levels of SNR the following procedure was employed, first written in short statements followed by their detailed descriptions:

(i) Simulate an arbitrarily scaled white-field $\psi_0(\boldsymbol{\rho}_s)$ and sample ESW $\psi(\boldsymbol{\rho}_s)$; (ii) propagate the ESW and white-field to detector plane to retrieve the arbitrarily scaled diffraction and white-field intensity. Then respectively scale to correspond to a given number of total photons; (iii) include inherent shot-noise to the diffraction and white-field intensity respectively; (iv) for the diffraction and white-field intensity convert photon number in each pixel to correspond to a number of ADUs; (v) include to this data of diffraction and white-field intensity inherent background noise present in a measurement, and perform a subtraction of a certain percentage of this background.

(i) To simulate an arbitrarily scaled sample ESW $\psi(\boldsymbol{\rho}_s) = T(\boldsymbol{\rho}_s)\psi_0(\boldsymbol{\rho}_s)$, an object density was selected seen in Figure 4.2.1a with zero outside and maximum value inside the boundaries of object, then convolved with a small Gaussian width to give less sharp edges. Every pixel value in this 2048×2048 object array was divided by the largest number in the array, then multiplied by the sample thickness $\tau(\boldsymbol{\rho}_s) = 150\,\mathrm{nm}$. To obtain the magnitude and phase of the transmission function $T(\boldsymbol{\rho}_s)$, in each pixel we assume that the sample is homogenous gold and by the Equations 2.2.4-2.2.6, set the magnitude and phase respectively as

$$|T| = exp\left[-\beta k \tau(\boldsymbol{\rho}_s)\right] \text{ and}$$

$$\phi_T = -\delta k \tau(\boldsymbol{\rho}_s)\,.$$

To obtain magnitude and phase of the white-field in the detector plane $\psi_0(\boldsymbol{\rho}_d)$, we simulated a white-field intensity distribution in the detector plane by assigning to each pixel in detector plane a magnitude equal to

$$e^{-\frac{\boldsymbol{\rho}_d}{(2\times G\times \Delta x_D)}},$$

(where G is a decay constant and $\Delta x_D = 13.5\ \mu$m is the pixel width), and phase equal to

$$\frac{\pi \boldsymbol{\rho}_d^2}{\lambda \times (\frac{-1}{z_{FD}-z_{FS}} + \frac{1}{z_{FD}})}.$$

The resulting complex array was multiplied pixelwise with a complex valued circle (that first was a real circle with magnitude 1 between beam stop radius and the beam radius and zero otherwise, then convolved and then turned into a complex circle with a magnitude equal to the corresponding real pixel value), which resulted in a precursor white-field in the detector plane, whose magnitude and phase are given in Figure 4.2.1bc.
Then only the magnitude of the white-field were kept and utilizing the white-field phase

recovery algorithm (Section 2.2.2) by 21 iterations, to recover the phase seen in Figure 4.2.1d, yielding the arbitrarily scaled $\psi_0(\boldsymbol{\rho}_d)$. (This reconstruction was done so that the phase matches the one recovered by the same algorithm from simulated noisy white-field data described in Section 4.3).
This white-field was then propagated to the sample plane by a Fresnel transform yielding $\psi_0(\boldsymbol{\rho}_s)$, then multiplied pixelwise with the transmission function array, resulting in the arbitrarily scaled ESW $\psi(\boldsymbol{\rho}_s)$.

(ii) The ESW $\psi(\boldsymbol{\rho}_s)$ was propagated to the detector plane by a Fresnel transform. Taking the modulus squared of each complex value in the resultant array yielded it's diffraction intensity $|\psi(\boldsymbol{\rho}_d)|^2$. The sum of all intensity over all pixels $\sum_{n=1}^{N} |\psi(\boldsymbol{\rho}_d)|^2$ of this arbitrarily scaled diffraction intensity, was then converted to correspond to a selected number of total measured photons M. The range of M examined we chose between $5 \times 10^5 - 10^{14}$ photons. A 1 second data frame is taken to correspond to 10^7 measured photons. Thus equivalently a corresponding range of $0.05 - 10^7$ number of frames were selected.
Summing all pixel values in the diffraction intensity, divided by the selected number of photons, yields

$$\Xi = \frac{\sum_{n=1}^{N} |\psi(\boldsymbol{\rho}_d)|^2}{M} .$$

Each pixel value at coordinate $\boldsymbol{\rho}_d$ in the arbitrarily scaled diffraction intensity $|\psi(\boldsymbol{\rho}_d)|^2$ and white-field intensity $|\psi_0(\boldsymbol{\rho}_d)|^2$, was divided by this quantity Ξ, yielding a probabilistic value of photons in that pixel $\psi^M(\boldsymbol{\rho}_d)$ and $\psi_0^M(\boldsymbol{\rho}_d)$ respectively. The sum $\sum_{n=1}^{N} |\psi^M(\boldsymbol{\rho}_d)|^2$ was then equal to the number of photons M, and the resulting sum $\sum_{n=1}^{N} |\psi_0^M(\boldsymbol{\rho}_d)|^2$ was equal to a number a few percent larger than M.

(iii) To include shot-noise to the diffraction intensity each pixel photon value $\psi^M(\boldsymbol{\rho}_d)$, was replaced with a number $\psi^S(\boldsymbol{\rho}_d)$ drawn from a Poisson random distribution with a mean $\psi^M(\boldsymbol{\rho}_d)$ and uncertainty $\sqrt{\psi^M(\boldsymbol{\rho}_d)}$. Analogously to include shot-noise to the white-field intensity each pixel photon number $\psi_0^M(\boldsymbol{\rho}_d)$, was replaced with a number $\psi_0^S(\boldsymbol{\rho}_d)$ drawn from a Poisson random distribution with a mean $\psi_0^M(\boldsymbol{\rho}_d)$ and uncertainty $\sqrt{\psi_0^M(\boldsymbol{\rho}_d)}$. The result is diffraction and white-field intensity with the inherent Poisson distributed shot-noise. (This shot-noise is a valid approximation also for FCDI [12, 33, 34]).

(iv) To simulate what happens in an actual experiment the diffraction and white-field intensity was converted from photons to an integer number of 'analog to digital units' (ADUs). This may be approximated by viewing the histogram of experimental intensity data that the single energy photon peak is roughly Gaussian distributed. In accordance to the single energy peak ($\lambda = 2.535$ keV) in the histogram of experimental intensity data of Figure 2.3.1, this Gaussian distributed variable x was chosen to have a mean $\mu = 157$ ADUs and standard deviation $\sigma = 30$ ADUs. Thus in the diffraction intensity the number of photons in each pixel $\psi^S(\boldsymbol{\rho}_d)$, was replaced with $\psi^S(\boldsymbol{\rho}_d)$ summed numbers from this Gaussian distribution. Analogously for the white-field intensity the number of photons in each pixel $\psi_0^S(\boldsymbol{\rho}_d)$, was replaced with $\psi_0^S(\boldsymbol{\rho}_d)$ summed numbers from this distribution. (To save computation in Gaussian distribution summation, we used the fact that summing a number of Gaussian distributed variables x_1, x_2, x_3..., is the same as drawing a number from a Gaussian distributed variable x with mean $\mu = \mu_1 + \mu_2 + \mu_3$... and variance $\sigma^2 = \sigma_1^2 + \sigma_2^2 + \sigma_3^2$... [35]). The resulting value of ADUs in each pixel was rounded to an integer number of ADUs and any negative values were set to zero [24]. The resulting measurement data to this point are $I(\boldsymbol{\rho}_d)$ in Equation 4.2.1 (though only the diffraction data were used for all SNR calculations). Figure 4.2.1e shows an example of diffraction data $I(\boldsymbol{\rho}_d)$ with the steps until here for 10^9 measured photons, equivalent to 100 frames of 1 second exposure data that are perfectly correlated, background subtracted and thresholded.

(v) To simulate background noise for the diffraction and white-field data respectively. All aspects of the CCD plus photons from the surrounding that gives rise to this background are combined. A background distribution in an histogram of experimental intensity data is approximately Gaussian distributed. In accordance with Figure 2.3.1 (which shows background noise accumulated for a 1 second measurement of data), this Gaussian distributed variable x^B was chosen to have a mean of $\mu^B = 210$ ADUs and standard deviation $\sigma^B = 14$ ADUs. For background in diffraction and white-field data simulations we only considered 100 and 10^4 second measurement data with inherent background noise. For example 100 seconds of exposure time equivalent to 10^9 measured photons (up to step (iv) above), we added 100 seconds of background noise by adding in each pixel 100 numbers of the Gaussian distributed variable x^B.
To mimick the stochastic noise left from a background subraction and provide differing values of SNR. A certain percentage 0-100% of the Gaussian mean $100 \times \mu^B$ were subtracted from each pixel, in the same or different percentage in the diffraction and white-field data. Any negative values were set to zero. The resulting amount of background noise left after a background subtraction is $B(\boldsymbol{\rho}_d)$ in Equation 4.2.1 (though only the diffraction data were used for all SNR calculations).
Figure 4.2.1f shows an example of diffraction data ($I(\boldsymbol{\rho}_d)$+$B(\boldsymbol{\rho}_d)$) with the steps until here for 10^9 measured photons, equivalent to 100 frames of 1 second exposure data, where 0% of the background is subtracted.

The true ESW to compare reconstructions to in Section 4.3 was made by following the two step procedure (i-ii), in addition subtracting the white-field and multipliplying by a factor of $157\left[\frac{\text{ADU}}{\text{photon}}\right]$ (to be in the same scale as the respective 'analog-to-digital' converted noise simulated diffraction data). Furthermore a Fresnel transform back to the real space was done to generate the true ESW. The transmission function (TF) generated in step (i) we used for comparison to reconstructions of Section 4.3. It can be seen in Equation 2.2.8 that the TF are independent of scaling. This true ESW and it's TF are seen in Figure 4.2.2.

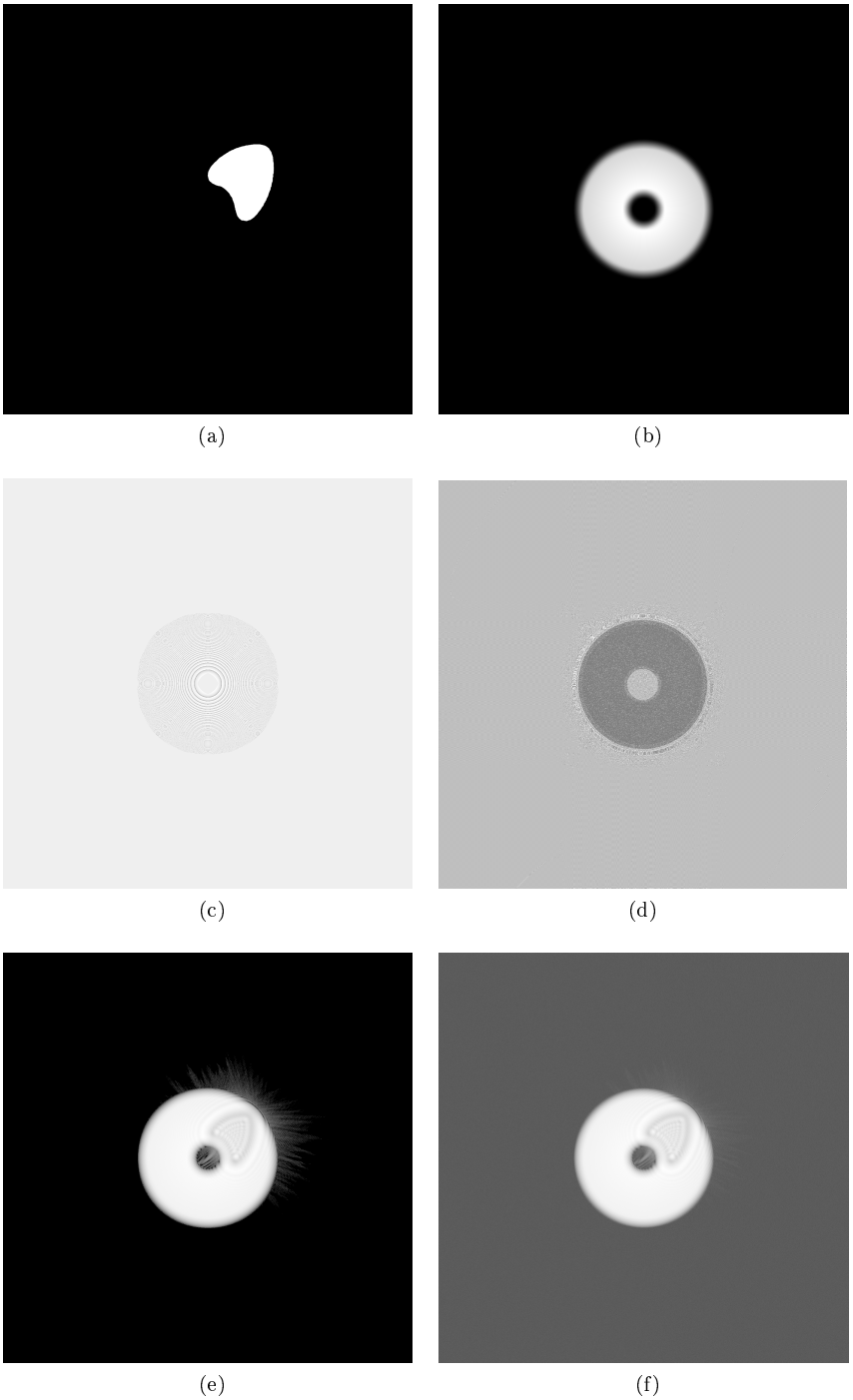

(a) (b)

(c) (d)

(e) (f)

Figure 4.2.1: Examples for the procedure of Section 4.2, for simulating noisy diffraction and white-field data.
(a) The initial real object density that was used in step (i).
(b) Simulated magnitude of white-field in detector plane of step (ii).
(c) Simulated phase of white-field in detector plane of step (ii).
(d) The recovered phase of the white-field intensity of step (ii).
(e) The diffraction data after step (i-iv), with 10^9 measured photons or equivalently 100 frames of measurement data. Corresponding to perfectly correlated, background subtracted and thresholded data. Log-scale.
(f) After step (v), that is adding 100 frames of background noise to (e). Corresponding to perfectly correlated data that have no background subtracted. Log-scale.

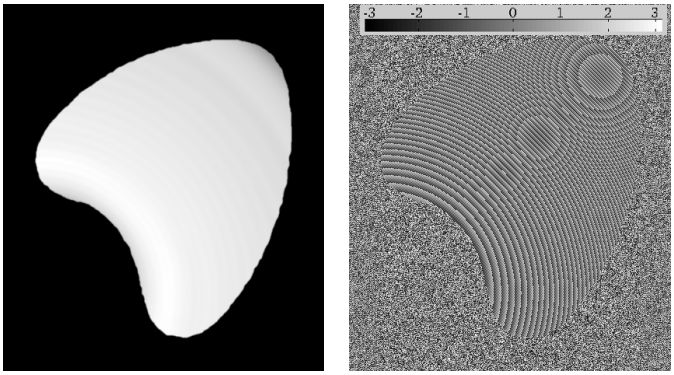

(a) (b)

(c) (d)

Figure 4.2.2: The true ESW, (a) magnitude, (b) phase. And the true TF; (c) magnitude, (d) phase. Generated as described in Section 4.2, used for comparison to reconstructions in Section 4.3. The ESW magnitude is zero outside and positive inside object, scale bar included for phase. The TF has inverted colours since the magnitude has value 1 outside object and 0.7 inside. And phase has zero value outside object and -0.62 inside. (All simulated images in this thesis are .tiff format which use black for the lowest value and white for the highest, and gray scale in between).

4.3 Reconstructions

Simulated experimental measurement of diffraction and white-field data, with various sources and levels of noise were generated according to the method described in the previous section. Here the results on the quality of reconstructions are examined. In Section 4.3.1 we will first show an example of a reconstruction when no noise is included. Then in Section 4.3.2 a wide range of shot-noise will be examined, and also a wide range of iteration numbers for a certain amount of shot-noise. And lastly in Section 4.3.3 we investigate a wide range of background noise of different proportions in the diffraction and white-field data. The iterative phase retrieval algorithms tested are Error Reduction (ER) and Hybrid Input-Output (HIO), which are introduced in Section 2.2.1.

For all tests in this chapter the true ESW, true TF and the simulated measurement data were generated as 2048×2048 pixel arrays. And the reconstructions were carried out in the same array size. The real space support used were 420×470 pixels in extent. For HIO, $\beta = 1$ [28], the same as in Chapter 3. For each test of simulated data we used the procedure in Section 2.2.2 by 21 iterations, to recover a phase for the white-field data to be used in the iterative algorithms.

To recover a phase for the diffraction data, the standard procedure was to perform five reconstructions by 125 iterations for each algorithm at each noise level. Each of these five iterative reconstructions start with a different set of random phases, this was done by subtracting the

white-field from the diffraction data and setting the phase of each pixel to a random value between $\pm 0.2\pi$, then propagating to the sample plane and applying a support. We regard the quantity ρ_k^n as the iterate, where k is the iteration number and n is the ranking of the five reconstructions. The convention is that $\pi_m^F \rho_k^n$ is an estimate of the ESW, that is a solution [20, 23, 22]. The following error metrics were calculated for each reconstruction and algorithm at each noise level, a large value of these error metrics indicates a poor agreement between the two compared arrays, and a zero value would indicate perfect agreement.:

Mean square deviation of the best solution and the true ESW (or true solution) (denoted by $0(\boldsymbol{\rho}_s)$),

$$\xi_1^0 = \frac{\sum_{n=1}^{N} \left[\pi_m^F \rho_k^1(\boldsymbol{\rho}_s) - 0(\boldsymbol{\rho}_s)\right]^2}{\sum_{n=1}^{N} I(\boldsymbol{\rho}_d)}. \tag{4.3.1}$$

Mean square deviation of the best and second best solution,

$$\xi_1^2 = \frac{\sum_{n=1}^{N} \left[\pi_m^F \rho_k^1(\boldsymbol{\rho}_s) - \pi_m^F \rho_k^2(\boldsymbol{\rho}_s)\right]^2}{\sum_{n=1}^{N} I(\boldsymbol{\rho}_d)}. \tag{4.3.2}$$

Mean square deviation of best solution and it's iterate in real space,

$$\chi^2 = \frac{\sum_{n=1}^{N} \left[\rho_k^1(\boldsymbol{\rho}_s) - \pi_m^F \rho_k^1(\boldsymbol{\rho}_s)\right]^2}{\sum_{n=1}^{N} I(\boldsymbol{\rho}_d)}. \tag{4.3.3}$$

And the equivalent error metric in reciprocal space [12, 20],

$$\chi^2_{reciprocal} = \frac{\sum_{n=1}^{N} \left[|\mathcal{F}(\rho_k^1(\boldsymbol{\rho}_d))| - \sqrt{I(\boldsymbol{\rho}_d)}\right]^2}{\sum_{n=1}^{N} I(\boldsymbol{\rho}_d)}. \tag{4.3.4}$$

The five best solutions was ranked by the lowest $\chi^2_{reciprocal}$.
We also calculated the analogous error metrics for the transmission function of solutions (obtained by Equation 2.2.8):

$${}^{TF}\xi_1^0 = \frac{\sum_{n=1}^{N} \left[\left(\frac{\pi_m^F \rho_k^1(\boldsymbol{\rho}_s)}{\psi_0} + 1\right) - {}^{TF}0(\boldsymbol{\rho}_s)\right]^2}{\sum_{n=1}^{N} I(\boldsymbol{\rho}_d)}, \tag{4.3.5}$$

$${}^{TF}\xi_1^2 = \frac{\sum_{n=1}^{N} \left[\left(\frac{\pi_m^F \rho_k^1(\boldsymbol{\rho}_s)}{\psi_0} + 1\right) - \left(\frac{\pi_m^F \rho_k^2(\boldsymbol{\rho}_s)}{\psi_0} + 1\right)\right]^2}{\sum_{n=1}^{N} I(\boldsymbol{\rho}_d)}, \tag{4.3.6}$$

$${}^{TF}\chi^2 = \frac{\sum_{n=1}^{N} \left[\left(\frac{\pi_m^F \rho_k^1(\boldsymbol{\rho}_s)}{\psi_0} + 1\right) - \left(\frac{\rho_k^1(\boldsymbol{\rho}_s)}{\psi_0} + 1\right)\right]^2}{\sum_{n=1}^{N} I(\boldsymbol{\rho}_d)}. \tag{4.3.7}$$

In addition we have for all tests calculated the magnitude and phase entity of ξ_1^0, ξ_1^2, χ^2 and ${}^{TF}\xi_1^0$, ${}^{TF}\xi_1^2$, ${}^{TF}\chi^2$ (included in Appendix B.2.4). However in this chapter we will only show the

error metrics above comparing the complex entity. The error metrics comparing magnitude or complex entity have almost identical behaviour, whereas the ones comparing phase entity shows resembling behaviour, to be discussed later in this chapter.

For this chapter we will mostly show the solution of ER and HIO. Since the TF of solution display same appearance with regard to variation and artifacts as the solution for all tests. (All solutions with TF are given in Appendix B).

4.3.1 Zero Noise Solution

For this example we obtained a reconstruction from diffraction and white-field data with no noise inherent as shown in Figure 4.3.1. The data were generated by a modified procedure of Section 4.2, that is step (i-ii) with 10^{14} measured photons selected and excluding step (iii-v), that is no shot noise or background included, and in step (iv) there are no variation from the Gaussian mean 157 $[\frac{\text{ADU}}{\text{photon}}]$ in the photon to ADU conversion. We note the blurred internal features within and surrounding the boundary of the solution, which is as expected. (A complex constraint for a similar experimental setup [36] has been shown to greatly increase the reconstruction quality, though in this work a complex constraint were not applied).
The error metric values for this reconstruction are seen in Table 4.1. The number of 10^{14} measured photons we chose because shot-noise for this number of photons is negligible. Thus to show that the error metrics including shot-noise in Section 4.3.2 for 10^{14} photons, has the same value as in Table 4.1. Note a scaling in number of measured photons will cancel out in numerator and denominator of ξ_1^0, ξ_1^2, χ^2, but in the ${}^{TF}\xi_1^0$, ${}^{TF}\xi_1^2$, ${}^{TF}\chi^2$ the numerator will cancel out, and the denominator will be scaled.

ER	ξ_1^0	ξ_1^2	χ^2
	1.31×10^{-2}	1.18×10^{-4}	3.73×10^{-6}

ER	${}^{TF}\xi_1^0$	${}^{TF}\xi_1^2$	${}^{TF}\chi^2$
	1.74×10^{-10}	1.1×10^{-10}	1.65×10^{-10}

HIO	ξ_1^0	ξ_1^2	χ^2
	1.23×10^{-2}	1.66×10^{-4}	9.8×10^{-4}

HIO	${}^{TF}\xi_1^0$	${}^{TF}\xi_1^2$	${}^{TF}\chi^2$
	4.5×10^{-9}	2.17×10^{-9}	2.32×10^{-7}

Table 4.1: The error metric values for the case when no noise is included in data as described in Section 4.3.1.

It is seen in Figure 4.3.1 that solutions by ER and HIO show similar quality, also their respective first and second best solutions show similar quality. In addition the $\chi^2_{reciprocal}$ values for sorting the 5 reconstructed iterates in table 4.2. This indicates that a unique solution is obtained regardless of which random start-phases are used, when no noise is inherent in the data.

ER	1	2	3	4	5
$\chi^2_{reciprocal}$	1.14×10^{-3}	1.15×10^{-3}	1.166×10^{-3}	1.178×10^{-3}	1.179×10^{-3}

HIO	1	2	3	4	5
$\chi^2_{reciprocal}$	3.75×10^{-6}	3.78×10^{-6}	3.83×10^{-6}	3.86×10^{-6}	3.9×10^{-6}

Table 4.2: The $\chi^2_{reciprocal}$ values used for sorting the reconstructed iterates, from diffraction and white-field data with no noise inherent.

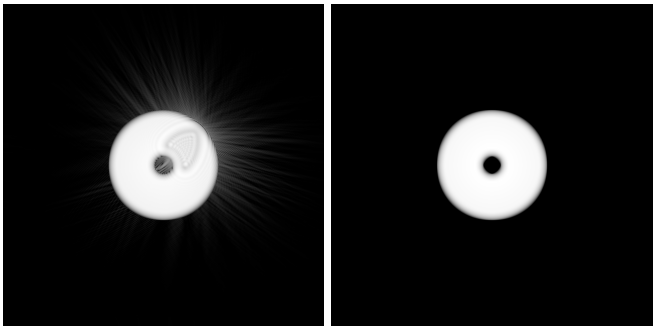

(a)

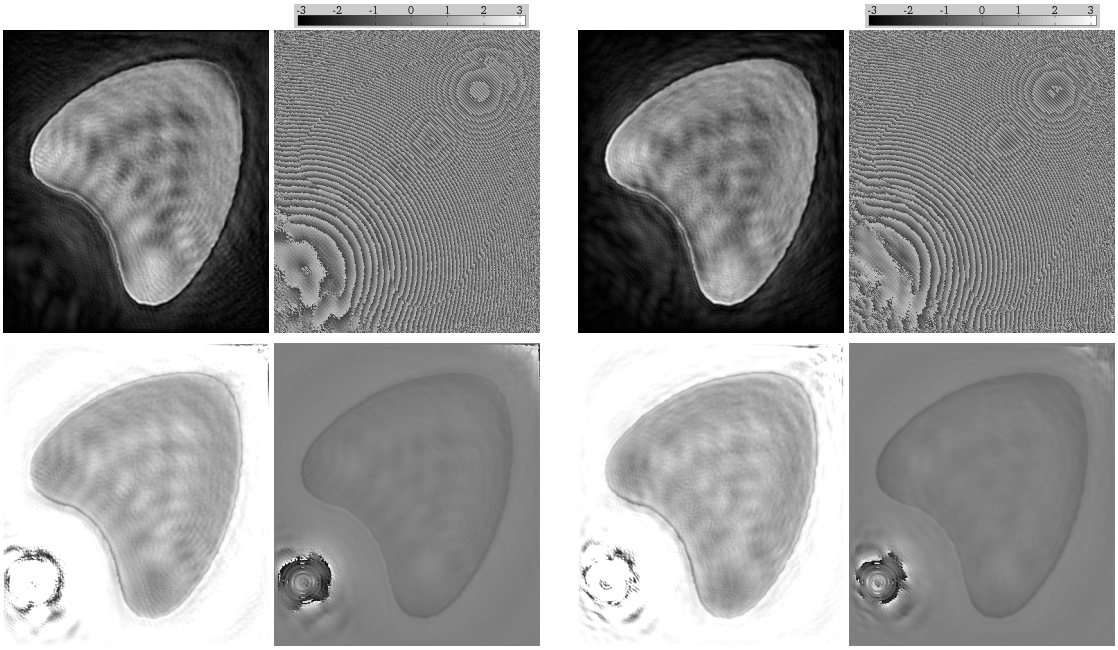

(b)

(c)

Figure 4.3.1: Solutions (support region displayed) from data with no noise inherent.
(a) The diffraction data (left) and white-field data (right). (b) The best solution of ER and HIO respectively: First row show the solution ($\pi_m^F \rho_k^1$), magnitude (left) and phase (right). In second row we see the retrieved transmission function ($\frac{\pi_m^F \rho_k^1}{\psi_0} + 1$), magnitude (left) and phase (right). (To make the transmission function magnitude visible, everything above 1 is replaced with the value 1). The scale bar included applies to both phase of solution and it's TF. (c) The second best solution of ER and HIO respectively: Here only the magnitude of solution ($\pi_m^F \rho_k^2$) are shown, note the identical quality as ($\pi_m^F \rho_k^1$).

4.3.2 Photon Number

Here we use the steps (i-iv) in Section 4.2 to simulate diffraction and white-field data. These data have a wide range $5 \times 10^5 - 10^{14}$ measured photons, which equals $0.05 - 10^7$ one second frames of data, with 10^7 measured photons per frame. This exceedingly wide range of photons are to investigate the behaviour of iterative algorithms for large amounts of shot-noise. With the inherent shot-noise of the photons measured, this yields SNR calculated only for the diffraction data in the interval 19 to 212923. These data corresponds to a summation of diffraction and white-field 1 second frames of data respectively that are perfectly correlated, background subtracted and thresholded. Three examples of the solution (or reconstructed ESW) are shown in Figure 4.3.2 and the error metric values are shown in Figure 4.3.3. (The entire range of simulated data and their respective solution are shown in Appendix B.1).
Although the solution and it's calculated TF will have the same quality and artifacts within the support region, they differ in the whole 2048×2048 array, and thus their error metric values differs as seen in Figure 4.3.3. For HIO ${}^{TF}\xi_1^0$,${}^{TF}\xi_1^2$ have high correlation and for ER ${}^{TF}\xi_1^0$,${}^{TF}\xi_1^2$, ${}^{TF}\chi^2$ have high correlation. Revealing the possible importance of the calculable error metrics (${}^{TF}\xi_1^2$, ${}^{TF}\chi^2$) in locating the true TF (here located by ${}^{TF}\xi_1^0$).
In Figure 4.3.3 ξ_1^0, ξ_1^2, χ^2 better reveal a criteria when the solutions are close in quality to the zero noise solution of Section 4.3.1. That is for ER when more than 10^8 photons are measured (SNR>218) and for HIO when more than 5×10^{10} photons are measured (SNR>4789). Below this criteria they respectively show a higher value of ξ_1^2 and a noisy solution that departs from a "zero-noise solution" (this may be confirmed by seeing all the solutions in Appendix B.1). Although ${}^{TF}\xi_1^0$,${}^{TF}\xi_1^2$, ${}^{TF}\chi^2$ is not a good indicator of this criteria, even when the denominator is unscaled (see Figure 4.3.3). Note although that the criteria holds here for both the solution and it's TF, since they display same appearance in support region.
The difference in reconstruction quality of ER and HIO at approximately 10^9 measured photons (SNR=686), are well represented by ξ_1^0. Data with 10^9 measured photons is what we understand from litterature are the order of what can be typical in FCDI experiments [12, 20, 23, 22, 36, 31]. We note here the larger difference of ρ_k^1 against $\pi_m^F \rho_k^1$ in HIO, than for ER. As in CDI (Chapter 3) the HIO iterate is not to be regarded as a solution, apart from ER where the iterate and solution has better agreement.

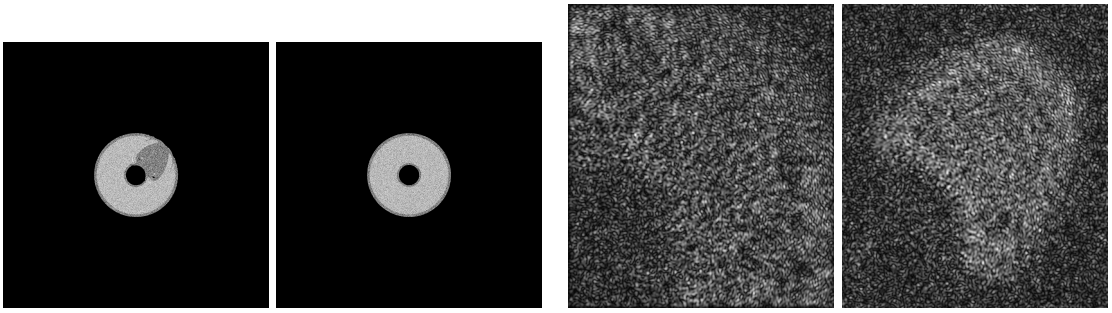

5×10^5 photons (SNR=19).

(a)

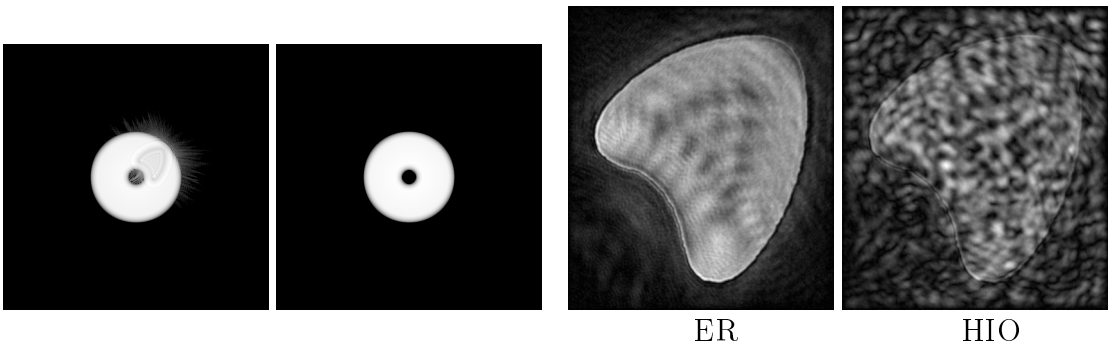

10^9 photons (SNR=686).

(b)

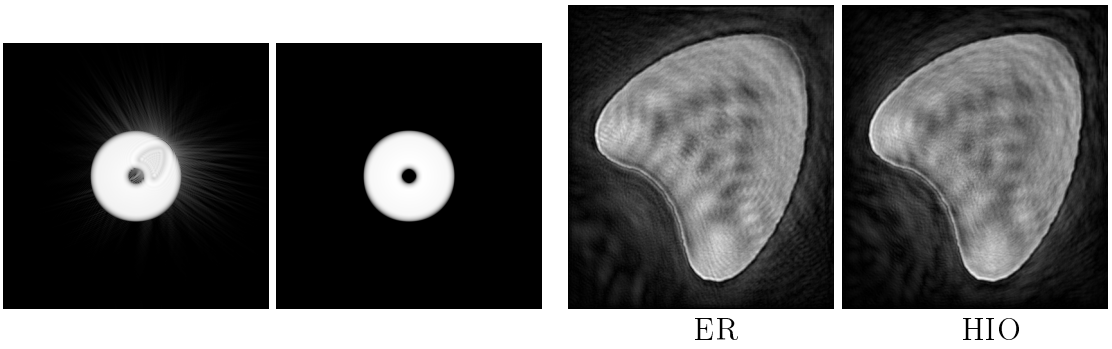

10^{14} photons (SNR=212923).

(c)

Figure 4.3.2: Magnitude of solution (support region displayed) from diffraction and white-field data (log-scale), that have different amount of measured photons with inherent shot-noise, yielding different signal-to-noise ratio.
(a) 5×10^5 measured photons, (b) 10^9 measured photons, (c) 10^{14} measured photons. For (a), (b), (c), from left to right: Diffraction data, white-field data, magnitude of ER solution, magnitude of HIO solution.

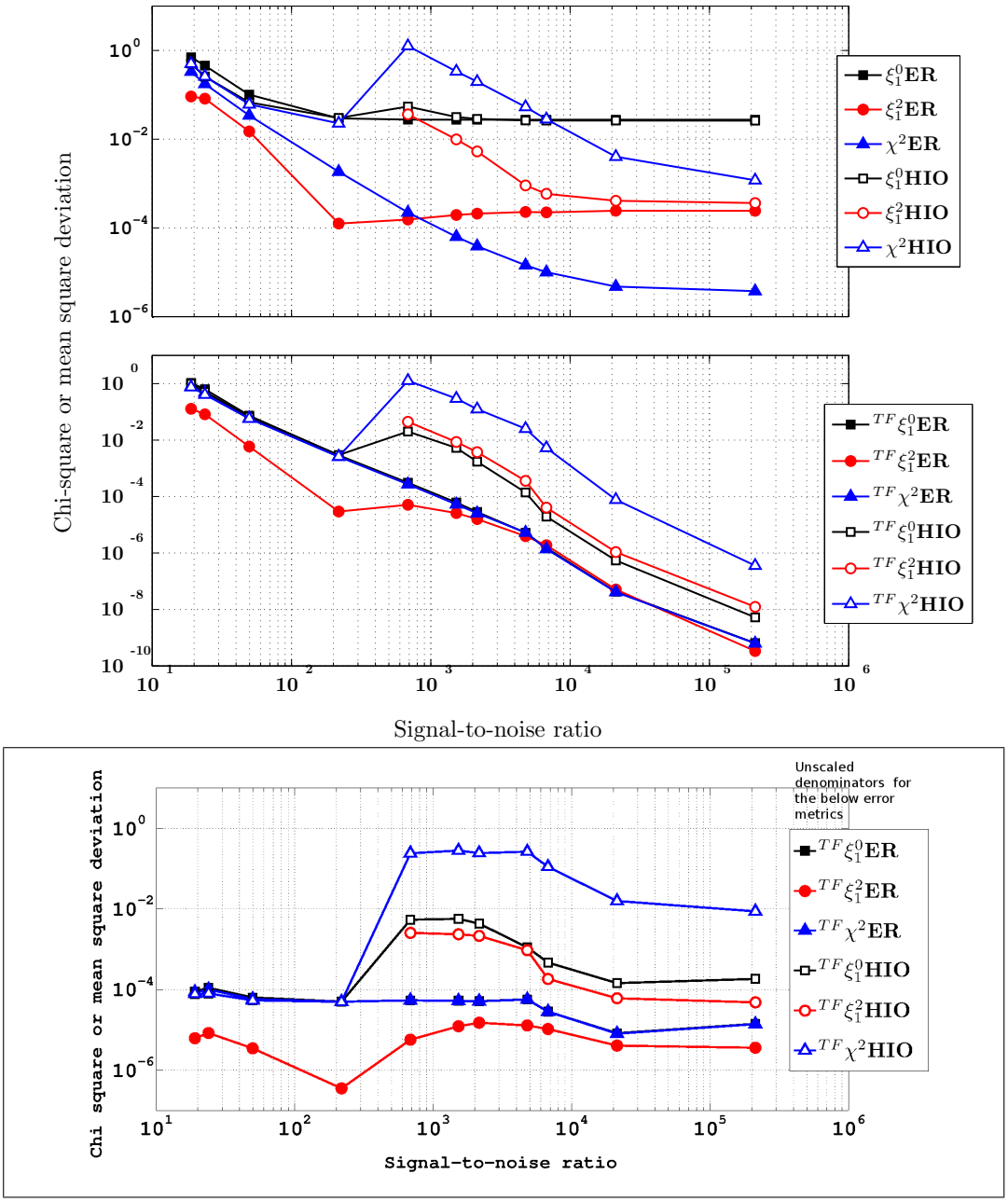

Figure 4.3.3: The error metric results from data with varying amount of measured photons. The TF error metrics ($^{TF}\xi_1^0$, $^{TF}\xi_1^2$ $^{TF}\chi^2$) have steeper slope from that of the solution (ξ_1^0, ξ_1^2, χ^2). Because a scaling in measured photons will cancel out in the numerator of the TF error metrics, but their denominator will have this scaling. Apart from the ESW error metrics where the scaling in numerator and denominator cancels out. (In the framed graph, are modified TF error metrics with an denominator of unscaled summed intensity, so that these are independent of scaling by number of photons, just as the original solution error metrics are.) Also note here that $^{TF}\xi_1^0$, $^{TF}\xi_1^2$ have high correlation for HIO and $^{TF}\xi_1^0$, $^{TF}\xi_1^2$ $^{TF}\chi^2$ have high correlation for ER. The quality of the zero noise solution and values of ξ_1^0, ξ_1^2 are reached for ER when more than 10^8 photons are measured (SNR>218) and for HIO when more than 5×10^{10} photons are measured (SNR>4789). For the shot-noise with 10^{14} measured photons (SNR=212923), the solution and TF error metric values are very close to those of the zero noise solution in Table 4.1 of Section 4.3.1 (because of equal scaling with 10^{14} measured photons for $^{TF}\xi_1^0$, $^{TF}\xi_1^2$ $^{TF}\chi^2$).

4.3.2.1 Iteration number

Here we used the diffraction and white-field data with three different amounts of shot-noise for 5×10^5, 10^9 and 10^{14} measured photons. The conditions for the iterative algorithms are the same. However instead of only using 125 iterations (whose solution can be seen in Figure 4.3.2), the range between $1-456$ iteration numbers are investigated. The respective error metric values versus iteration number with the solution after 5 and 456 iterations, are shown in Figure 4.3.4-4.3.6.

The results for data with 5×10^5 measured photons, Figure 4.3.4. For this high amount of shot-noise the quality of solution is materially destroyed. The error metric values does not vary substantially, and HIO indicates worse solutions, reproducibility and difference of iterate and solution, than that of the ER algorithm.

The results for data with 10^9 measured photons, Figure 4.3.5. ER displays good convergence and quality close to that of a zero-noise solution, indicated by the stable error metric values. Although HIO deteriorates with increasing iteration number, along with the error metric values that increase, indicating a diverging solution, reproducibility and increasing difference of iterate and solution.

The results for data with 10^{14} measured photons, Figure 4.3.6. This amount of measured photons, makes shot-noise negligible. However we see that again ER is stable at a zero-noise solution, although χ^2 indicates a decreasing difference of iterate and solution. For the HIO algorithm the solution is close to a zero-noise solution, and seems to show a small inclination to converge to the true solution (O), this we have not verified. However HIO also shows an increasing reproducibility and difference of iterate and solution, which may imply it is a diverging behaviour.

The error metrics values in Figure 4.3.4-4.3.6, shows that ER have close correlation between ${}^{TF}\xi_1^0$, ${}^{TF}\chi^2$ and to a lesser extent also with ${}^{TF}\xi_1^2$. Apart from HIO which shows good correlation of ${}^{TF}\xi_1^0$, ${}^{TF}\xi_1^2$. Thus this imply that the calculable error metrics ${}^{TF}\xi_1^0$, ${}^{TF}\chi^2$ are good identifiers of an estimate to a true solution, for atleast the amount of shot-noise and iteration numbers that we have tested.

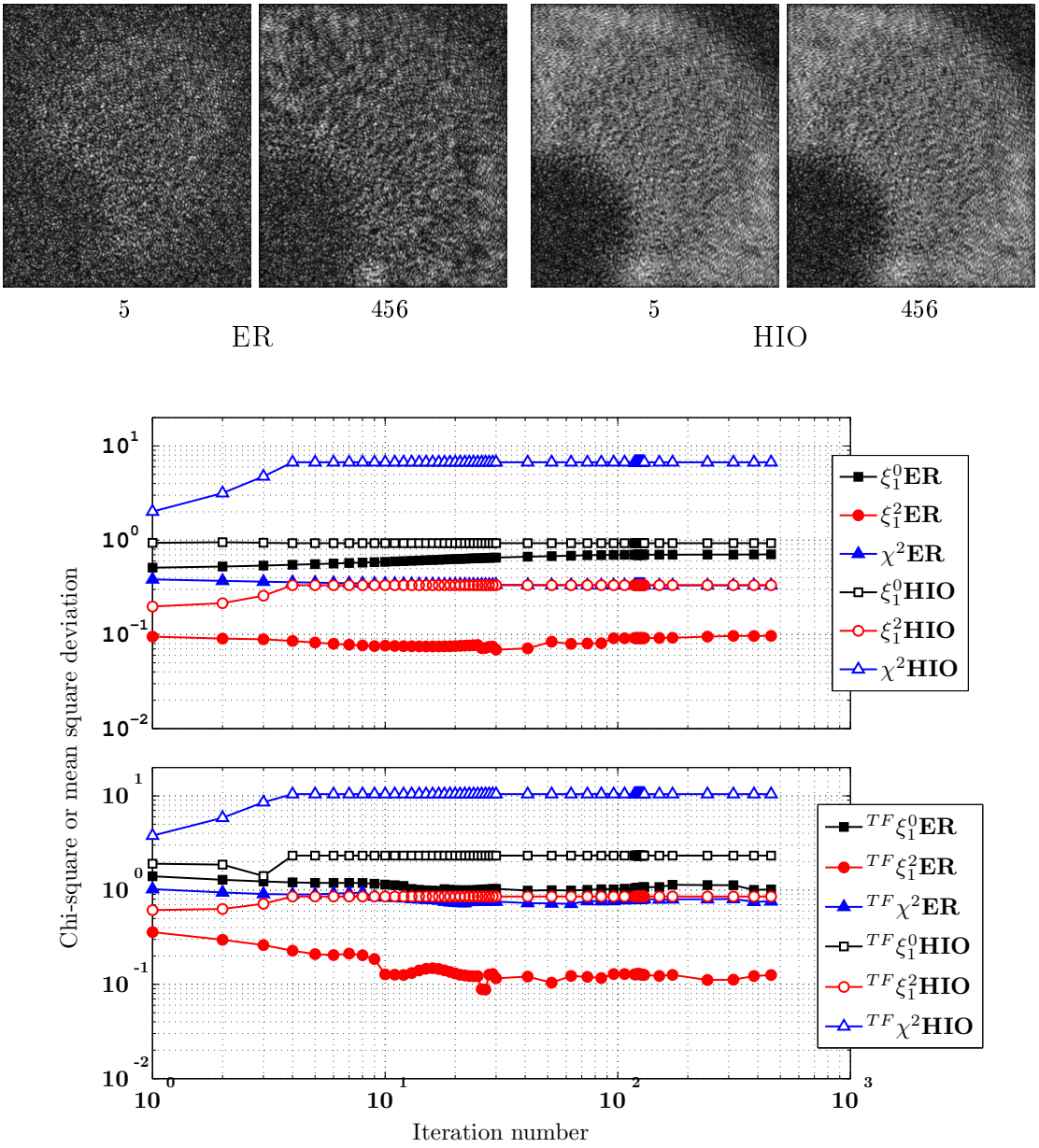

Figure 4.3.4: Iteration number dependency on solutions from diffraction and white-field data that have only shot-noise inherent for 5×10^5 measured photons. Above are the magnitude of solution ($|\pi_m^F \rho_k^1|$) after 5 and 456 iterations. Below are the error metric values versus iteration number.
The error metric values and solution does not vary much by the iteration number. Although for this high level of shot-noise the quality of the solution are materially destroyed. The higher value of HIO error metrics indicates worse solutions, reproducibility and difference of iterate (ρ_k^1) and solution ($\pi_m^F \rho_k^1$), than that of the ER algorithm.

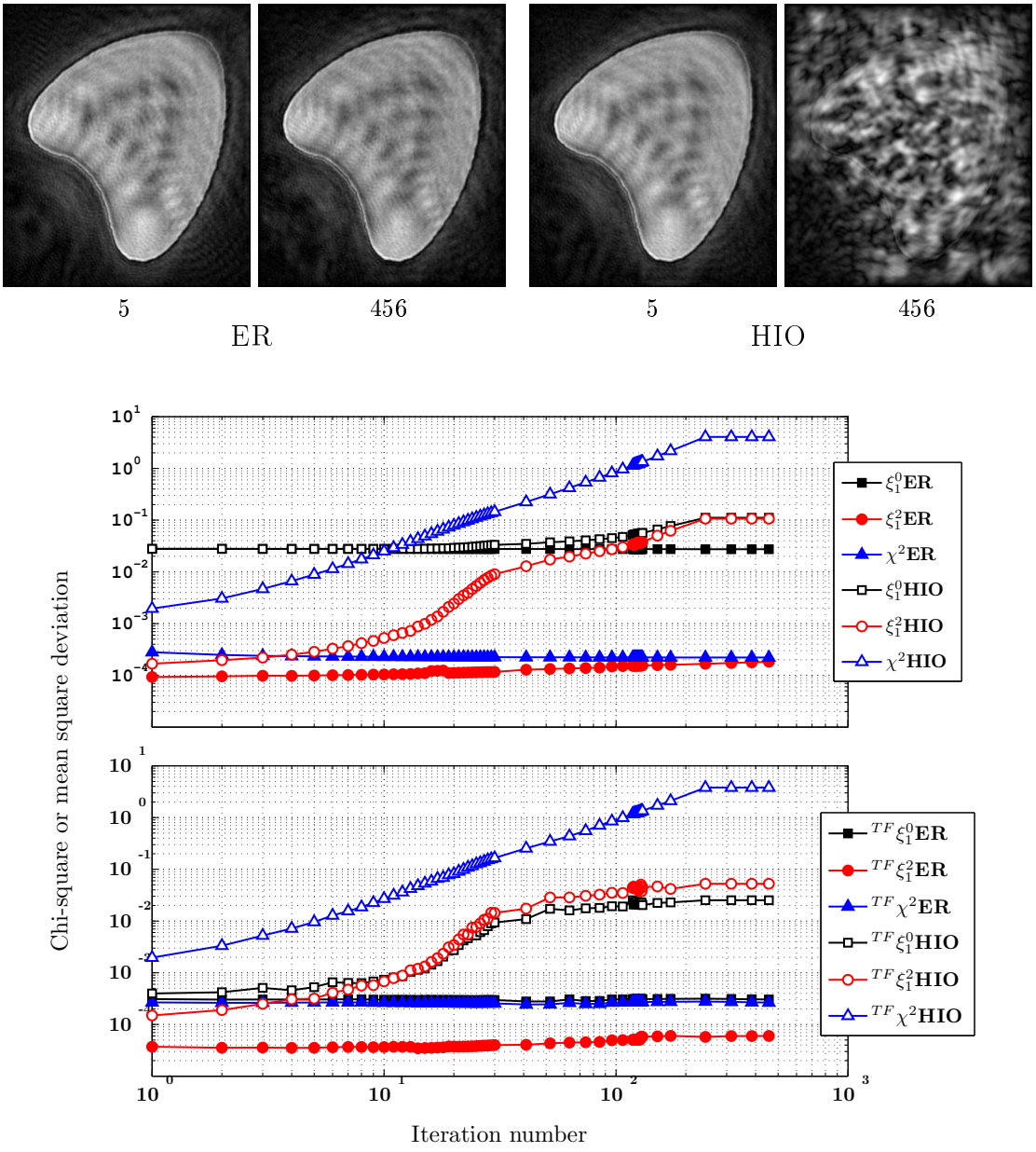

Figure 4.3.5: Iteration number dependency on solutions for diffraction and white-field data that have only shot-noise inherent for 10^9 measured photons. Above are the magnitude of solution ($|\pi_m^F \rho_k^1|$), after 5 and 456 iterations. Below are error metric values versus iteration number. For the ER algorithm the error metric values and solution does not vary much by the iteration number, with the solution staying close to a zero noise solution. The increasing value of HIO error metrics indicates a diverging solution, with deteriorating reproducibility and increasing difference of iterate (ρ_k^1) and solution ($\pi_m^F \rho_k^1$). Note for ER the precise correlation of $^{TF}\xi_1^0$, $^{TF}\chi^2$. And for HIO we see the good correlation of $^{TF}\xi_1^0$, $^{TF}\xi_1^2$.

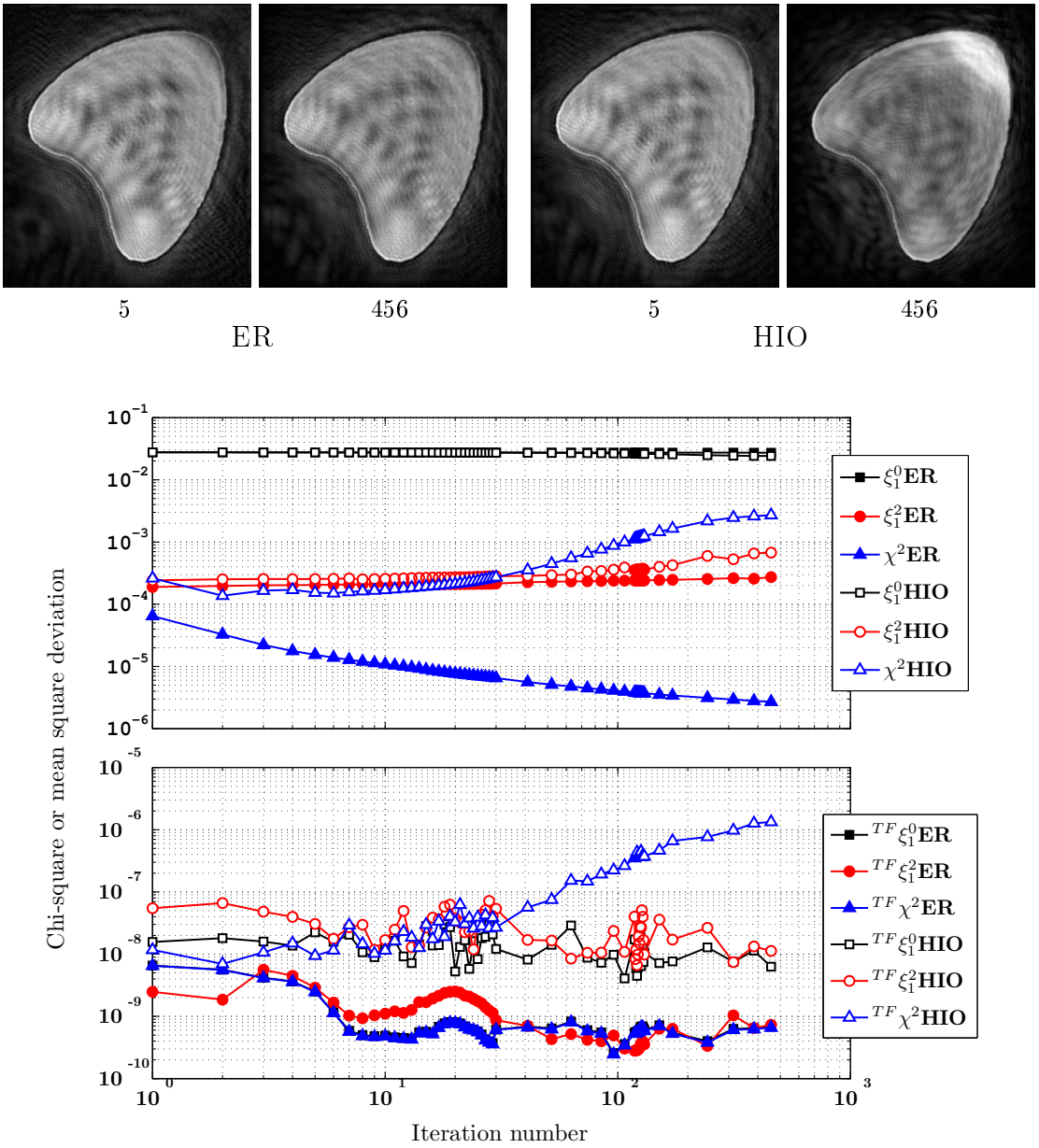

Figure 4.3.6: Iteration number dependency on solutions from diffraction and white-field data that have only shot-noise inherent for 10^{14} measured photons. Above we see the magnitude of solution ($|\pi_m^F \rho_k^1|$), after 5 and 456 iterations. Below are the error metric values versus iteration number.
For the ER algorithm, solution and error metric values does not vary much. Although as seen in χ^2 the difference between iterate and solution diminishes. Neither do HIO vary much although it shows an artifact at the upper right corner of the solution for higher iteration numbers, almost as if it were a slow convergence to the true solution (O). Although HIO by higher iteration numbers, gradually seems to yield less reproducible solutions, and more difference between iterate and solution. Note for ER the perfect correlation of $^{TF}\xi_1^0$, $^{TF}\chi^2$ and to a lesser extent to $^{TF}\xi_1^2$. And for HIO we see the good correlation of $^{TF}\xi_1^0$, $^{TF}\xi_1^2$.

4.3.3 Incomplete Background Subtraction

Here we performed an extensive simulation of diffraction and white-field data with inherent shot-noise for 10^9 measured photons, with equal or different proportions of background levels. The procedure for this may be understood from steps (i-v) in Section 4.2. Background subtracting 0-100% of the background mean (100×210 ADUs), of the diffraction and white-field data.
For the three cases (Section 4.3.3.1-4.3.3.3), we used the same diffraction data range, 0-100% background subtracted, yielding a SNR interval 1.8 to 339:
In case I (Section 4.3.3.1) we used white-field data with the same amount of background as the diffraction data for it's entire range.
In case II (Section 4.3.3.2) we used a fixed white-field data that had 100% background subtracted and were thresholded, for the entire diffraction data range.
In case III (Section 4.3.3.3) we used a fixed white-field data that had 95% of the background subtracted, for the entire diffraction data range.

In Section 4.3.3.4, additional tests are shortly described.

In addition we performed analogously all tests in this section for data with negligable shot-noise. Simulating by steps (i-v) of Section 4.2, white-field and diffraction data corresponding to 10^{11} measured photons. Background subtracting 0-100% of the background mean ($10^4 \times 210$ ADUs), of the diffraction and white-field data. Thus diffraction data range used for the analogous tests of case I-III had a SNR interval 1.8 to 3365. What are notable is that very much the same artifacts on solutions are reached as when considering case I-III with shot-noise for 10^9 measured photons. So we only included the error metrics results in Section 4.3.3.1-4.3.3.4 to demonstrate this point. Though the shot-noise for 10^{11} measured photons (SNR = 6762) is substantially less than that for 10^9 measured photons (SNR = 686), and solutions by ER and HIO is very similar for this lesser shot-noise (see Section 4.3.2). What is more revealing in solutions of particularly case I, is that the quality of solutions by HIO is more affected by adding background noise and ER being more resilient. Differences in error metrics due to shot-noise in this section can be understood from the shot-noise plot of Figure 4.3.3. It is noted again for all tests in this section (and the whole chapter) that the solution and TF error metrics differ, however they display the same general appearance and artifacts due to noise within the support region.

4.3.3.1 Case I

Here for the whole SNR range of 0-100% background subtracted in diffraction data, we have used white-field data with an equal amount of background noise. Error metrics are shown in Figure 4.3.7 and two examples of data with solution are shown in Figure 4.3.8. (The entire range of data and solutions are shown in Appendix B.2.1).
Varying the amount of background noise equally in the diffraction and white-field data, give more or less the same quality of solution. Although the quality becomes better when the background level becomes smaller, especially for HIO.
When the diffraction and white-field data both have background-level, resulted in spurious cross-shaped features and copies of the object in solution and it's derived TF. Though this artifact is more prominent in ER for higher background levels, see Figure 4.3.8(a), and only slightly appears in HIO for small background, see Figure 4.3.8(b). The same artifact arises when a white-field extent support are used, excluding the spurious feature to arise from the rectangular support. Why this artifact occurs we have not yet found another explanation to. Solutions to ER display higher reproducibility or similarity (lower $\xi_1^2, {}^{TF}\xi_1^2$), for higher background in diffraction and white-field data, although the prominent spurious cross-shaped artifacts are present.

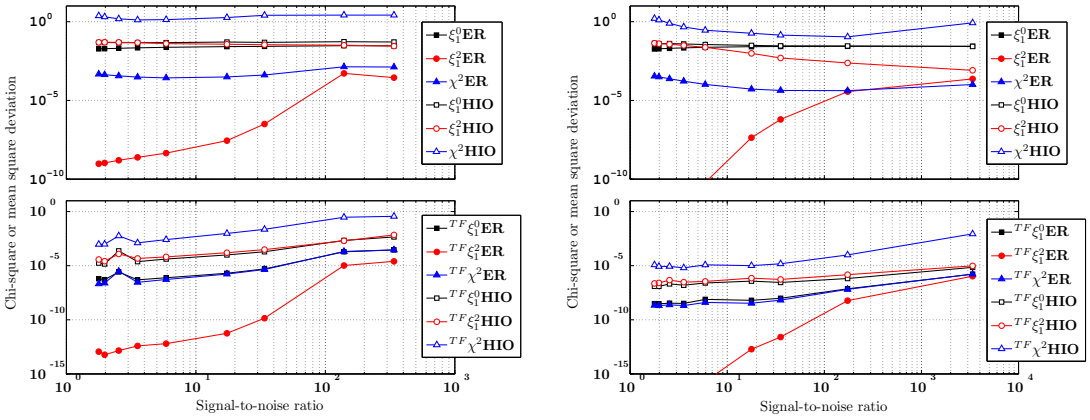

(a) (b)

Figure 4.3.7: The error metric results, for ER and HIO reconstructions from 0-100% equally background subtracted diffraction and white-field data with a certain amount of shot-noise (case I, Section 4.3.3.1). (a) Shot-noise for 10^9 measured photons. (b) Shot-noise for 10^{11} measured photons. The steep slope of decreasing ξ_1^2 for increasing background level in ER, implies that the reconstruction becomes more reproducible. Particularly again there is a precise correlation between ${}^{TF}\xi_1^0, {}^{TF}\xi_1^2$ for HIO, and ${}^{TF}\xi_1^0, {}^{TF}\chi^2$ for ER, revealing their possible importance in locating the true TF.

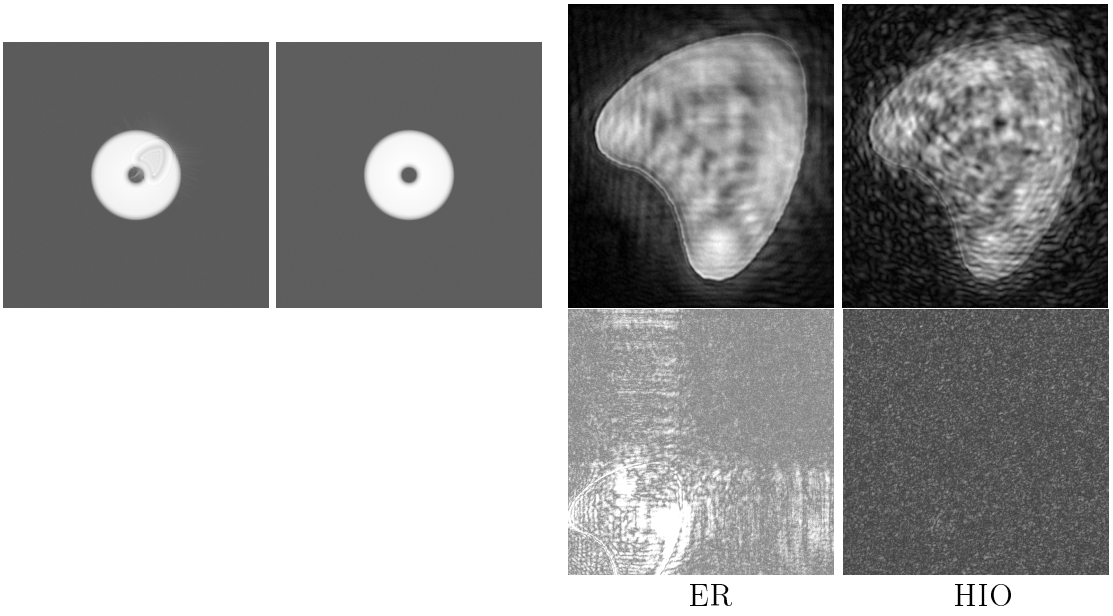

(a)

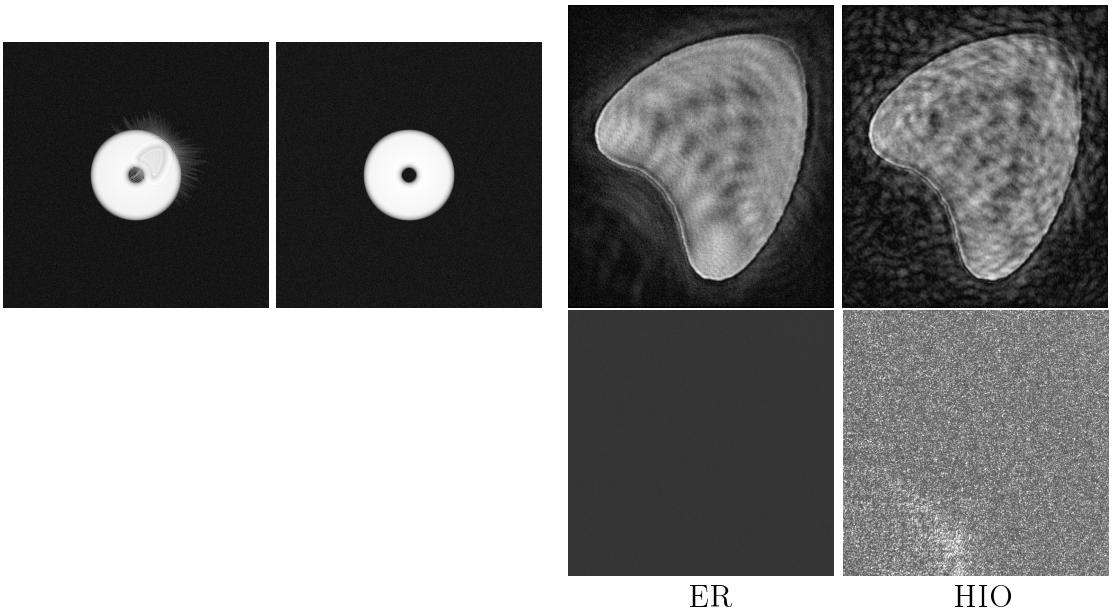

(b)

Figure 4.3.8: Two examples of case I (Section 4.3.3.1). For each (a) and (b), in the first row from left to right: Diffraction data (log-scale), white-field data (log-scale), support region of the magnitude of solution ($|\pi_m^F \rho_{125}^1|$) by ER and HIO. In the second row we see a zoomed in part of 768x768 pixels of the bottom left corner of the solution, contrasted to reveal the spurious copy of the object and crossed-over stripes that appear in magnitude and phase of the solution and it's derived TF.
(a) 0% background subtracted in diffraction data (SNR = 1.8). And 0% background subtracted in white-field data. Shot-noise for 10^9 measured photons. ER display the spurious cross shaped feature with stripes.
(b) 100% background subtracted in diffraction data (SNR = 338.9). And 100% background subtracted white-field data. Shot-noise for 10^9 measured photons. HIO display to some extent the spurious feature.

4.3.3.2 Case II

Here we used diffraction data with 0-100% background subtracted (SNR 1.8 to 338.9). For reconstructions we used this whole diffraction data range with a fixed white-field data that are 100% background subtracted and thresholded. The error metric plot are shown in Figure 4.3.9 and two examples are shown in Figure 4.3.10. (The entire range of data with solutions are shown in Appendix B.2.2).
This case is particularly interesting because it gives very similar effects as the background noise in CDI (Section 3.2.3). In Figure 4.3.10 we see the same rapidly varying magnitude in the solutions, that is a very noisy or to say ghost-like appearance. Much similar artifacts that were seen in reconstruction in CDI from data with background noise (Section 3.2.3). Not surprisingly this noise artifact must be related to vortices (phase-singularities). These vortices arise in the reciprocal space of the reconstructed iterate intensity ($|\rho^1_{125}|^2$), when zoomed in to a 64x64 area they look resembling for ER and HIO respectively to the corresponding ones we have seen in CDI. These vortices arise here up to a 99% background subtraction.
Also the spurious artifact with stripes in case I, does not arise for any of the solutions of case II. This artifact seemingly arises when there are no thresholding, or high background levels of both the diffraction and white-field data.
We note the overall steep slope of the error metrics in Figure 4.3.9, although HIO χ^2, ${}^{TF}\chi^2$ shows different behaviour, the HIO iterate deviates from the HIO solution. Although all behaviour of reconstructions for case I-III are the same with shot-noise for 10^9, 10^{14} measured photons, the error metrics results differ slightly, again this can be understood from Figure 4.3.3, Section 4.3.2.

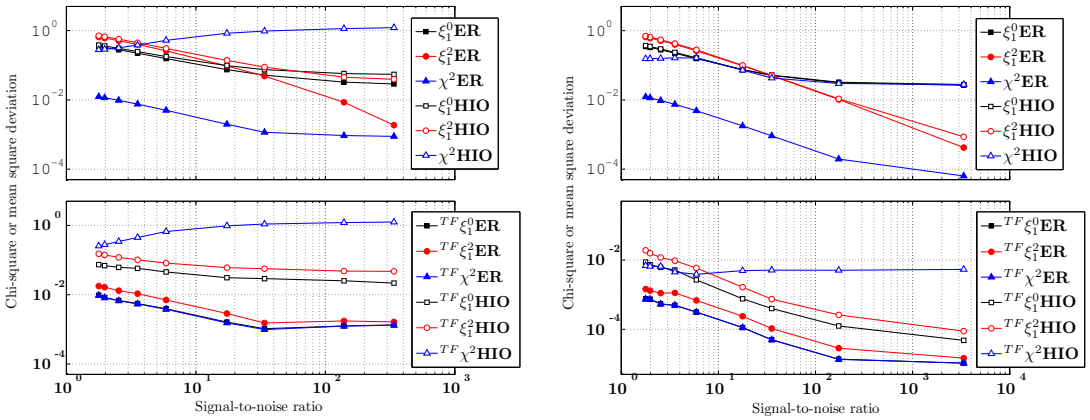

(a) (b)

Figure 4.3.9: The error metric results, for ER and HIO reconstructions from 0-100% background subtracted in diffraction data, and a fixed white-field data with 100% background subtracted and thresholding, (case II, Section 4.3.3.2).
(a) Shot-noise for 10^9 measured photons. (b) Shot-noise for 10^{11} measured photons.
Note the good correlation between ${}^{TF}\xi_1^0$,${}^{TF}\xi_1^2$ for HIO. And for ER there is again precise correlation of ${}^{TF}\xi_1^0$,${}^{TF}\chi^2$ also with ${}^{TF}\xi_1^2$.

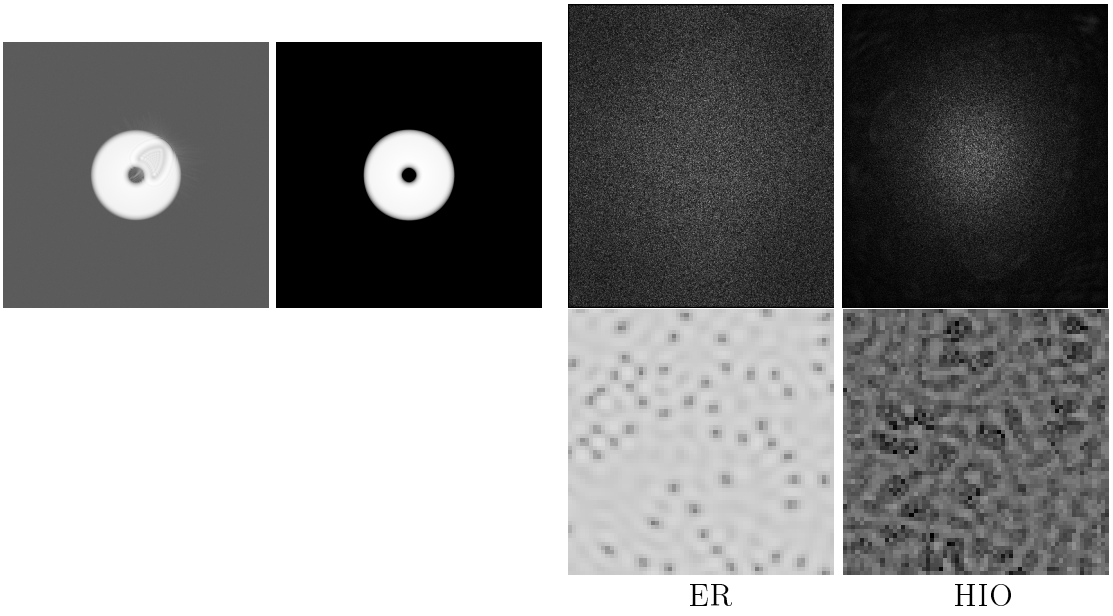

(a)

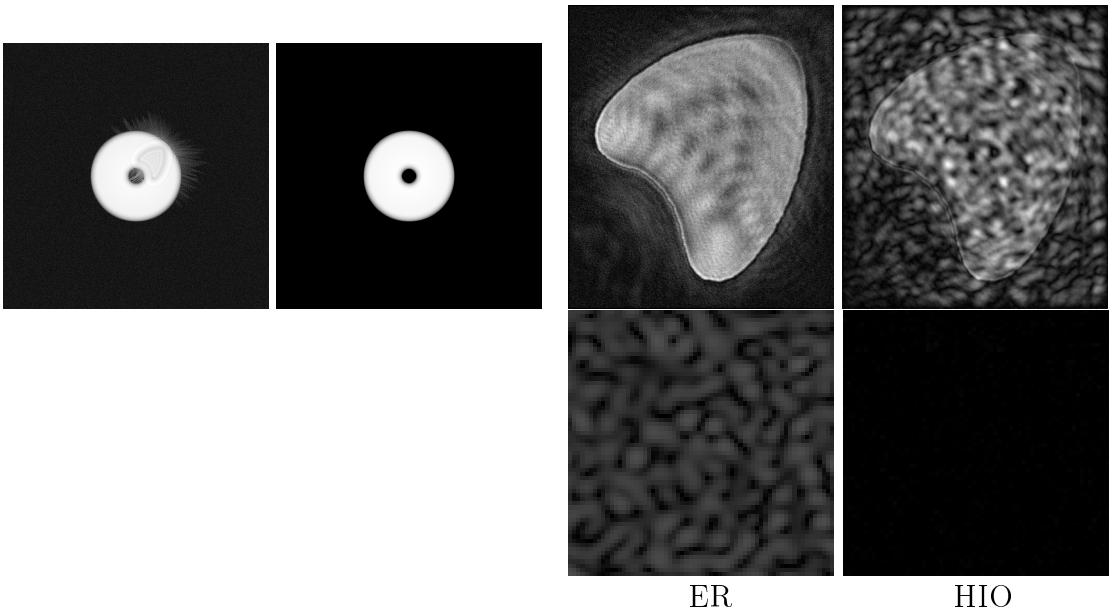

(b)

Figure 4.3.10: Two examples of case II (Section 4.3.3.2). For each (a) and (b), in the first row from left to right: Diffraction data (log-scale), white-field data (log-scale), support region of the magnitude of solution ($|\pi_m^F \rho_{125}^1|$) by ER and HIO. In the second row, below the solution, we see the iterate intensity ($|\rho_{125}^1|^2$) in reciprocal space (log-scaled), zoomed in to a 64x64 pixel area of the upper left corner.
(a) 0% background subtracted in diffraction data (SNR = 1.8). And 100% background subtracted and thresholded white-field data. Shot-noise for 10^9 measured photons. Resembling vortices appear in iterate reciprocal space as for CDI with background present in data (Section 3.2.3).
(b) 100% background subtracted in diffraction data (SNR = 338.9). And 100% background subtracted and thresholded white-field data. Shot-noise for 10^9 measured photons. For this level of noise vortices do not seem to show clearly in iterate reciprocal space. Although for less than 99% background subtracted in diffraction data, vortices do gradually appear evidently.

4.3.3.3 Case III

Here we used diffraction data with 0-100% background subtracted (SNR 1.8 to 338.9). For this whole diffraction data range we used a fixed white-field data that are 95% background subtracted. The error metric plot are shown in Figure 4.3.11, and two examples are shown in Figure 4.3.12. (The entire range of data with solutions are given in Appendix B.2.3). Again for all solutions in this chapter, the general appearance and artifacts appear in the solution and it's belonging TF, within the support region.
For diffraction data with less than 90% background subtracted yielded similar vortices and reconstructions as in case II. However different to the results in case II, here are a fine web of perpendicular stripes that appear over the 2048x2048 array of solution for the entire data range. When the diffraction data had close to between 90-100% background subtracted, the web of perpendicular stripes appeared more clearly, as seen in Figure 4.3.12(b). Also for the entire SNR range in the reciprocal space of the iterate intensity, are stripes aligned to form square features as seen in Figure 4.3.12(a). Any further explanation of these stripe artifacts we have not concluded, and is a subject to further investigation.

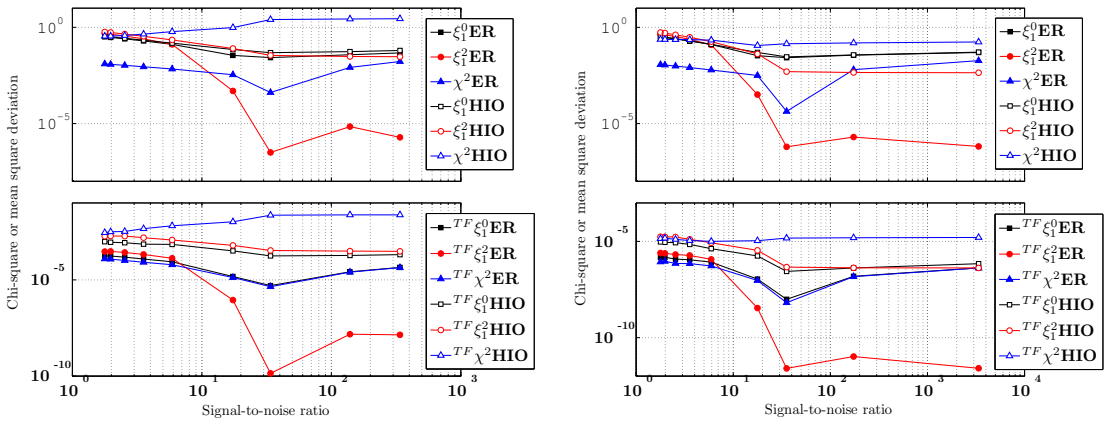

(a) (b)

Figure 4.3.11: The error metric results, for ER and HIO reconstructions from 0-100% background subtracted in diffraction data and a fixed white-field data with 95% background subtracted. (Case III, Section 4.3.3.3). (a) Shot-noise for 10^9 measured photons. (b) Shot-noise for 10^{11} measured photons. Note the close correlation between $^{TF}\xi_1^0$,$^{TF}\xi_1^2$ for HIO, and the precise correlation of $^{TF}\xi_1^0$,$^{TF}\chi^2$ for ER.

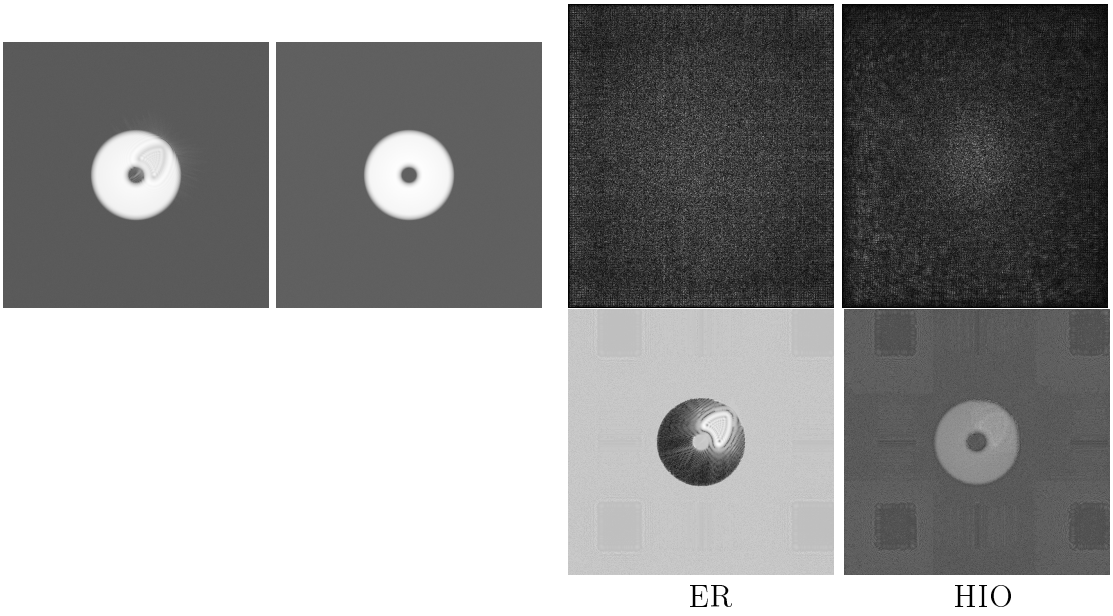

(a)

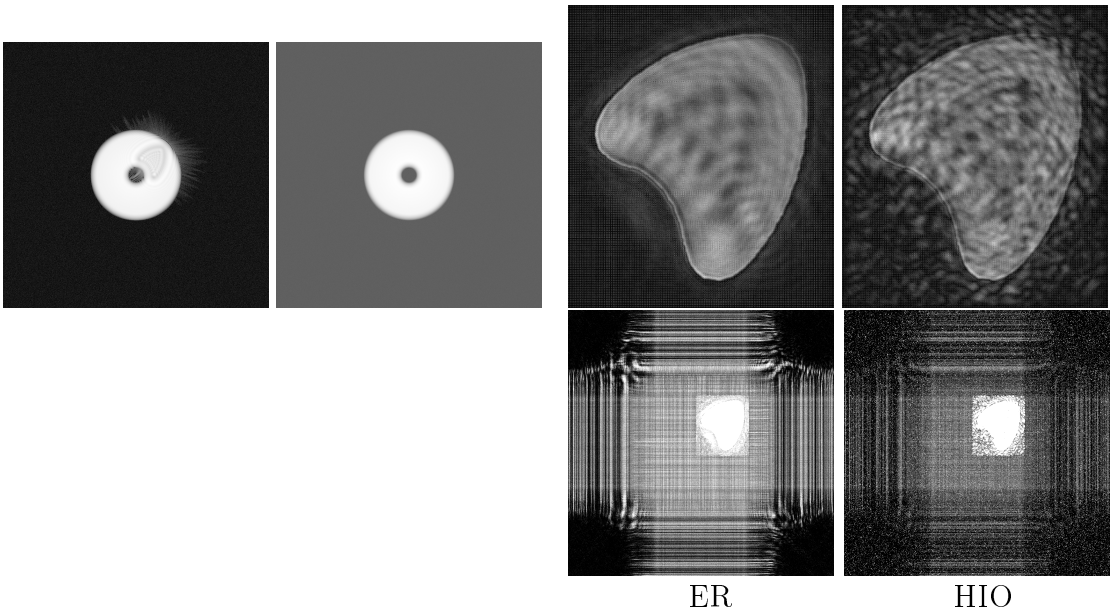

(b)

Figure 4.3.12: Two examples of case III (Section 4.3.3.3). For each (a) and (b), in the first row from left to right: Diffraction data (log-scale), white-field data (log-scale), support region of the magnitude of solution ($|\pi_m^F \rho_{125}^1|$) by ER and HIO.
(a) 0% background subtracted diffraction data (SNR = 1.8). And 95% background subtracted white-field data. Shot-noise for 10^9 measured photons. The solution looks much like as in case II, although here a web of stripes appear across the solution. Below the solution we see the intensity of the iterate ($|\rho_{125}^1|^2$) in reciprocal space (logscaled). What are barely seen here are vortices as in Figure 4.3.10(a) of Case II, but different here are also the appearance of stripes that cross-over to square structures.
(b) 100% background subtracted diffraction data (SNR = 338.9). And 95% background subtracted white-field data. Shot-noise for 10^9 measured photons. We see below the solutions, them being contrasted in the whole 2048x2048 array, which reveals the web of stripes across the solution. In the reciprocal space of the iterate there are also stripes in crossed-over structures, but no apparent vortices.

4.3.3.4 Additional Tests

In addition we performed a test with white-field data that have 0% background subtracted, and varying the background subtracted between 0-100% in the diffraction data (SNR between 1.8 to 338.9). In Figure 4.3.13 we see that the error metrics values has a trend to increase. For the diffraction data with 0% background subtracted (SNR=1.8), and white-field data that have 0% background subtracted, yielded the lowest error metrics and a fairly good reconstruction. As the percentage of the background subtracted from the diffraction data is increased, increasingly appearing is an artifact of a web of stripes that were seen in Figure 4.3.12b of case III. This artifact does not depend on the rectangular support chosen. With the extent of the white-field used as support the corresponding error metric plot and reconstructions, yielded very similar results.
The spurious object artifact as seen in Figure 4.3.8 of case I, appeared also here for the whole diffraction data SNR range, more prominent in the solution ($\pi_m^F \rho_{125}^1$) of ER. Seemingly appearing when there is background noise of both the diffraction and white-field data.

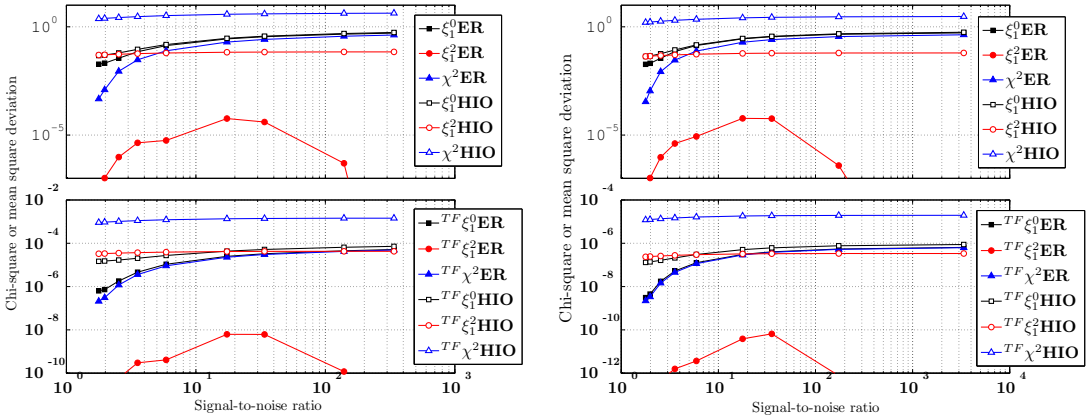

(a) (b)

Figure 4.3.13: The error metric results, for ER and HIO reconstructions, from 0-100% background subtracted in diffraction data and a fixed white-field data with 0% background subtracted. (a) Shot-noise for 10^9 measured photons. (b) Negligable shot-noise for 10^{11} measured photons. For ER ξ_1^2, $^{TF}\xi_1^2$ shows a bell-shape that is far below the other metrics, thus gives more reproducibility for certain tests. Again there is close correlation between $^{TF}\xi_1^0$,$^{TF}\xi_1^2$ for HIO, and the precise correlation of $^{TF}\xi_1^0$,$^{TF}\chi^2$ for ER.

In addition reconstructions were carried out from 10-90% interval of background subtracted in diffraction data, and a fixed white-field data that had 50% background subtracted. The error metrics are shown in Figure 4.3.14. For this test no vortices were noticed as in case II, though a minor appearance of the spurious artifact as in case I, Figure 4.3.8. And the web of stripes as in Figure 4.3.12 of case III did appear when the background mean in the diffraction and white-field data were'nt equal.

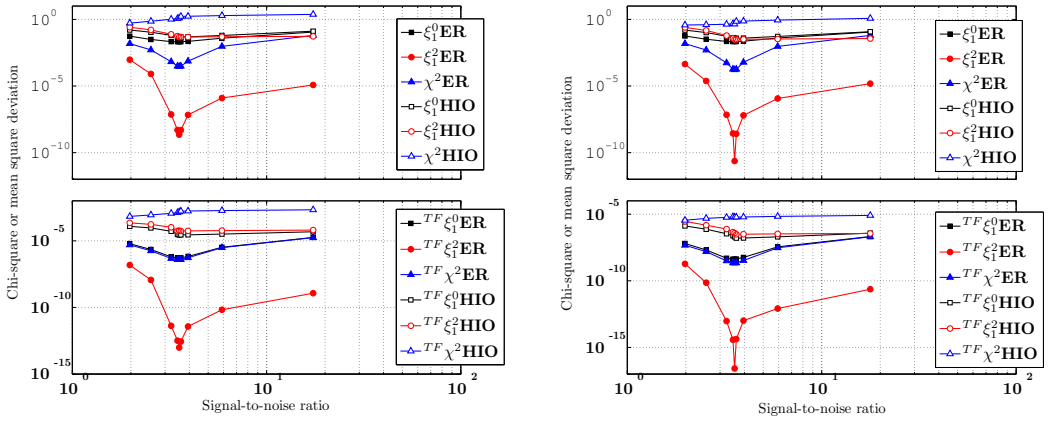

(a) (b)

Figure 4.3.14: The error metric results, for ER and HIO reconstruction from 10-90% background subtracted in diffraction data (SNR 2-17.4) and a fixed white-field data with 50% background subtracted. (a) Shot-noise for 10^9 measured photons. (b) Negligable shot-noise for 10^{11} measured photons. Again $^{TF}\xi_1^0$, $^{TF}\xi_1^2$ show good correlation in HIO, and ER $^{TF}\xi_1^0$, $^{TF}\chi^2$ shows good agreement.

4.4 Conclusions

In using iterative methods to recover lost phase information from a FCDI imaging experiment, it is imperative to consider the effect of noise and the resulting recovered phases before making quantative statements about the sample. Also to determine acceptable experimental conditions. For this purpose, we have simulated a wide range of noise from various sources to investigate the type and severity of artifacts introduced by the presence of noise in the measurement.

We have concluded that the zero noise solution (of Section 4.3.1) deviates to some extent from the true solution of Figure 4.2.2, for the algorithms and experimental parameters presented. Some blurred external features and what looks as interference artifacts within the solution, can be observed. Besides this the general shape and appearance of the true solution is reconstructed to good detail. Also there are a low value of $\xi_1^0 \approx 10^{-2}$, which indicates a fair agreement.

Of further interest is whether noise is likely to cause meaningful non-uniqueness of the final solution. For all FCDI noise tests with HIO and more notably for ER, twin image formation never occurs, and all reconstructions appear in the same position in the array. It is known that the value of $N_F \sim 10$, that we have used is to provide reliable convergence [20, 37]. Although if the data are overwhelmed with noise, it will yield noisy solutions with different artifacts depending on the type of noise. And thus deviate from a zero noise solution.

As expected assuming only shot-noise, simulations with a large number of measured photons allow a better estimate to a true solution. Here we have covered a very large range, $5\times10^5 - 10^{14}$ measured photons. Though in FCDI the number of photons that can be measured depends on sample damage, if there is a biological specimen or a metal, stability of the equipment, specific beamline, for example. In current FCDI experiments the number of frames collected in a single FCDI data set that are correlated, may correspond to more or less on the order of $10^8 - 10^{10}$ measured photons [12, 20, 23, 22, 36, 31]. Here it is implied that to reliably converge to the unique solution of the zero noise solution in Section 4.3.1, is for ER minimum $\sim 10^8$ measured photons, and for HIO minimum $\sim 5 \times 10^{10}$ measured photons. Below which they respectively tend to deviate in quality and give a more noisy solution. This criteria is also when ξ_1^0, ξ_1^2 will close in to the value of a zero-noise solution.
At least for moderate shot-noise inherent in data for 10^9 measured photons, ER reliably con-

verge to a zero noise solution seemingly for all iteration numbers. The HIO algorithm (for our parameters) yields a good estimate to the zero-noise solution for low shot-noise or more than $\sim 5 \times 10^{10}$ measured photons with iteration number $k = 125$, however gives tendency to diverge by increasing iteration number.

Additional background noise has shown to invoke different artifacts and effects on the reconstruction, depending on the balance of the background in the diffraction and white-field data. The overall results of these background noise tests was very similar both when there was significant shot-noise with 10^9 measured photons, and when it was more negligible for 10^{11} measured photons. We infer from our results when shot-noise and different proportions of background are both present in white-field and diffraction data, the effects on the solution are approximately additive. Although higher amount of shot-noise may yield other results.
In case I, when the background level, for the range $0 - 100\%$, were equal in the diffraction and white-field data. ER being more resilient yields solutions which are materially the same. Also solutions of HIO are materially the same but with increasingly noiser solutions, for increasing background level in diffraction and white-field data. Appearing is a spurious object artifact and stripes in the solution, in ER for higher background level in data, in HIO to a more negligable extent when the data are close to 100% background subtracted.
In case II, with white-field data that has been perfectly background subtracted and thresholded, but the diffraction data has insufficient background subtraction will cause vortices, seen in the reciprocal space of the resulting iterate intensity ($|\rho_{125}|^2$). Yielding a less defined and noisier real-space magnitude, this artifact appear here for this case with only 1% deviation in background from the diffraction and white-field data, and appear gradually when increasing the deviation. Here when the diffraction data are 100% background subtracted but not thresholded, there is a minor negligible deviation in quality.
In case III, for a white-field that has 95% background subtracted and diffraction data that has less background subtracted, a similar effect occurs as in case II. However apart from rapidly varying magnitude due to vortices, a web of stripes appears in the solutions. In contrast to when the diffraction data are 100% background subtracted, and the white-field data are 95% background subtracted, which gave rise to a web of stripes in the solution (but no apparent rapid changing magnitude due to vortices).

Hence cases I-III implies that even for small background levels remaining in diffraction and white-field data, will result in deviations and artifacts. These artifacts may be mistaken for actual physical features, so care should be taken to perform a good background subtraction. That means also to gather enough accurate statistical measurements of diffraction and white-field data, so that they have equal inherent shot-noise and background. In addition to gather accurate statistics of the background data used for background subtraction.

We have not investigated here any possible scenarios of beam scatter from optics or air. It is plausible that as in Chapter 3, the effect of a uniform distribution of say air scatter would be similar to solutions from diffraction and white-field data that are not thresholded. Which has already been shown here to have minor effects. Nevertheless care should be taken to avoid sources of alien scatter. For example a circular distribution of beam scatter from the order sorting aperture has been shown in Reference [21], which are not expected to have a straightforward impact on the reconstruction.

The error metric values ξ_1^0, ξ_1^2, χ^2, ${}^{TF}\xi_1^0, {}^{TF}\xi_1^2, {}^{TF}\chi^2$ respectively comparing complex entities has been examined for all tests in this chapter. Analogous error metrics comparing the respective magnitude and phase entities, has also been evaluated for each noise test in this chapter (for those interested, they are included in Appendix B.2.4). The error metrics comparing the magnitude entities is basically identical to the corresponding ones comparing complex entities, so that either one may be used. It is noted in the analogous error metrics comparing phase entities, that ${}^{TF}\xi_1^0, {}^{TF}\xi_1^2, {}^{TF}\chi^2$ has the same behaviour as the error metrics comparing magnitude and complex entity. Although ξ_1^0, ξ_1^2, χ^2 comparing phase entities is similar to those comparing magnitude or complex entities, however has a closer agreement. It is not obvious here that the calculable ξ_1^2 or χ^2 is best to use for any type or level of noise in the data, though a combination

of them may allow a safer identification of a good estimate to the generally unknown true ESW. For all noise levels tested in this Chapter, for ER ${}^{TF}\xi_1^0$ and ${}^{TF}\chi^2$ overlaps almost perfectly and in some tests also with ${}^{TF}\xi_1^2$. For HIO ${}^{TF}\xi_1^0$ ${}^{TF}\xi_1^2$ are in most tests closely correlated. This implies that the calculable ${}^{TF}\chi^2$, ${}^{TF}\xi_1^2$ should allow a safe identification of a good estimate to the generally unknown true solution. For example reconstructions by ER having a low ${}^{TF}\chi^2$, would imply a low ${}^{TF}\xi_1^0$, and thus indicate that a good estimate to the true transmission function has been reconstructed.

There may be several strategies to enchance the solutions fidelity, and which may affect the results presented here. A combination of ER and HIO is anticipated to increase the solutions fidelity, as was the case for CDI in Reference [1]. Modifications to the algorithms as a complex constraint [36], may increase the reconstruction reliability substantially, and may yield more robustness against noise.
The results in this chapter, may depend to some extent on the kind of sample chosen. We chose a single gold object with thickness 150 nm and width $\sim$ 5000 nm. That is a very thin object with no interior features, and with fairly sharp edges, yielding alot of high angle scatter.
Nevertheless the results reached in this chapter, gives an indication on what effects different sources of noisy data may have on the reconstruction, for any version of FCDI.

Chapter 5

Retrospect and Further Investigation

The motivation for this thesis were to reproduce the results by Williams *et al* [1, 2, 3] and show that the method works for CDI. Then extend it to the technique of FCDI, to explore the effects of relevant sources of noise. For both CDI and FCDI respectively in Chapter 3, 4 we have tested analogously the algorithms error reduction and hybrid input-output, covering large ranges of noise from different relevant sources, and have shown the resulting degration and artifacts. Also the behaviour of respective versions of error metrics measuring reproducibility and fidelity of the solutions, along with the conventionally used chi-square (χ^2), has been calculated for each test, showing their correlation. It has been revealed for both CDI and FCDI that error metrics may be used to find a solution of good fidelity to a true solution. Perhaps there are other error metrics that may be used to identify a good solution.
Although the ranges of noise level from various sources examined may be out of reach for what may be relevant in actual data treatment, it is still qualified to examine this range to see how the algorithms deteriorate with large levels of a certain noise source present. It's important to map out these kinds of behaviours, to provide information, for example when shot-noise may be of non-negligible concern, or which algorithms works best.
In particular similar noise simulations may be entitled to perform for other versions or improvements of CDI or FCDI techniques and phase-retrieval algorithms. Since the results obtained in this report may not be the same for other versions of CDI and FCDI.
The noise artifacts and features introduced in FCDI showed similarities and also differences to CDI. Due to apparent differences in methodology, modified algorithms and the comparison means of a diffraction and white-field data. An apparent similarity was the noisy solutions obtained by a low amount of measured photons, and the appearance of vortices in the presence of background. Further investigation may be entitled for evaluating the effects on equal or different background in diffraction and white-field data. For example definition of the vortices, and explanation of the spurious object cross stripes and web of stripes artifacts revealed in Section 4.3.3.

There has been previous work on adjusting the phase-retrieval algorithms, to alleviate the effects of shot-noise on the resulting solution in CDI [18, 38]. In the work of Dilanian *et al* [18], they considered statistical information about measurement errors, where they included a distribution of measurement errors into the reconstruction process using a statistically based modulus constraint. This diminished the effect of shot-noise and high quality reconstructions was obtained, both in simulation and experiment. It may be plausible that a similar approach can be used to reduce the effects of shot-noise in FCDI.

Appendix A

All Reconstructions from Chapter 3 Noise-Added Simulation for Coherent Diffractive Imaging

This appendix contains all simulated diffraction data and the respective reconstructed iterates as described in Chapter 3. For each of the three categories of noise in Appendices A.1-A.3, the first figure shows the entire range of the simulated diffraction data with different SNR. And in the following figures the respective best (out of five) iterates after 500 iterations by ER and HIO is shown. The iterate are for ER and HIO respectively displayed in a three picture row respectively, from left to right: logarithm of the reciprocal-space squared magnitude, the reciprocal phase, and the corresponding real-space magnitude (region inside support shown), of the iterate.

A.1 Photon Number

The results of Section 3.2.1 is shown here.

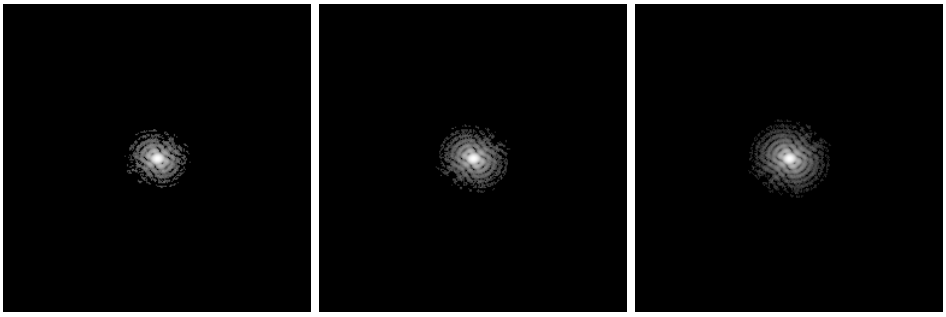

(a) **SNR = 299** (b) **SNR = 416** (c) **SNR = 625**

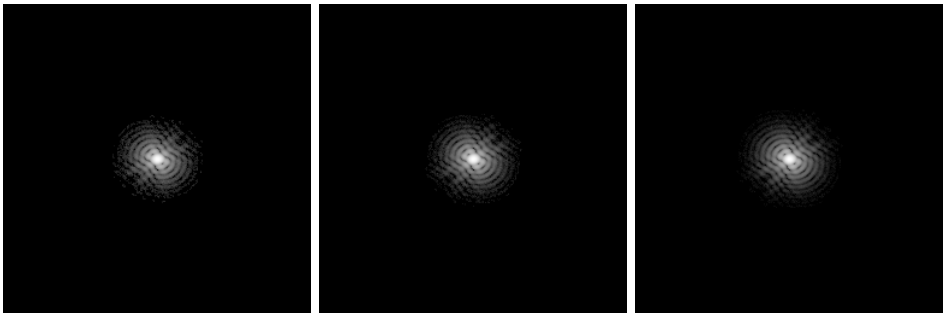

(d) **SNR = 860** (e) **SNR = 1191** (f) **SNR = 1846**

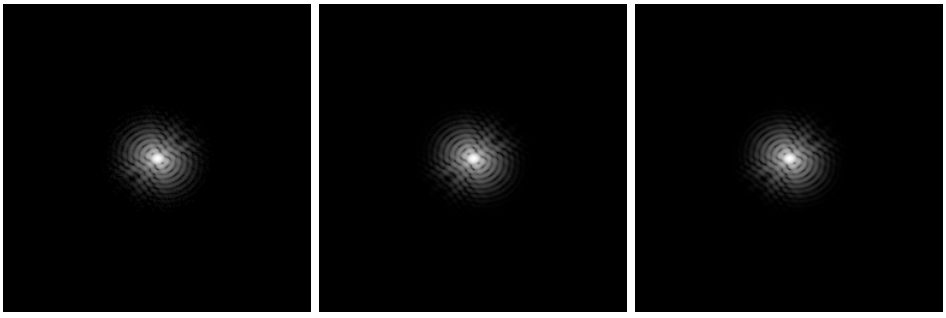

(g) **SNR = 2581** (h) **SNR = 5692** (i) **SNR = 8018**

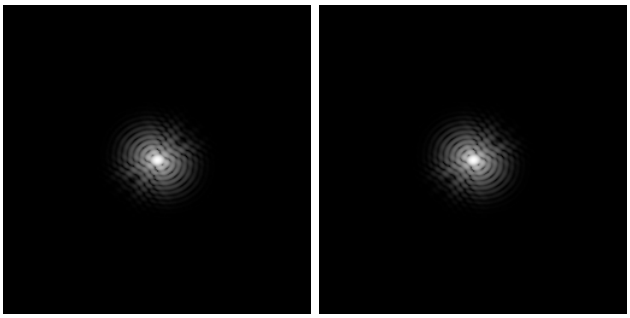

(j) **SNR = 17835** (k) **SNR = 25172**

Figure A.1.1: All simulated diffraction data of the analysis of Section 3.2.1, obtained by the steps (i-iv) in Section 3.1 for different number of measured photons and corresponding SNR. The number of photons in each pattern are: (a) 9×10^4, (b) 2×10^5, (c) 5×10^5, (d) 1×10^6, (e) 2×10^6, (f) 5×10^6, (g) 1×10^7, (h) 5×10^7, (i) 1×10^8, (j) 5×10^8, (k) 1×10^9. The diffraction data are shown in a logarithmic scale. Note that each image display similar brightness since each image is normalised to its own highest value. But they differ by orders of magnitude since different photon number yields different scaling in real and reciprocal space.

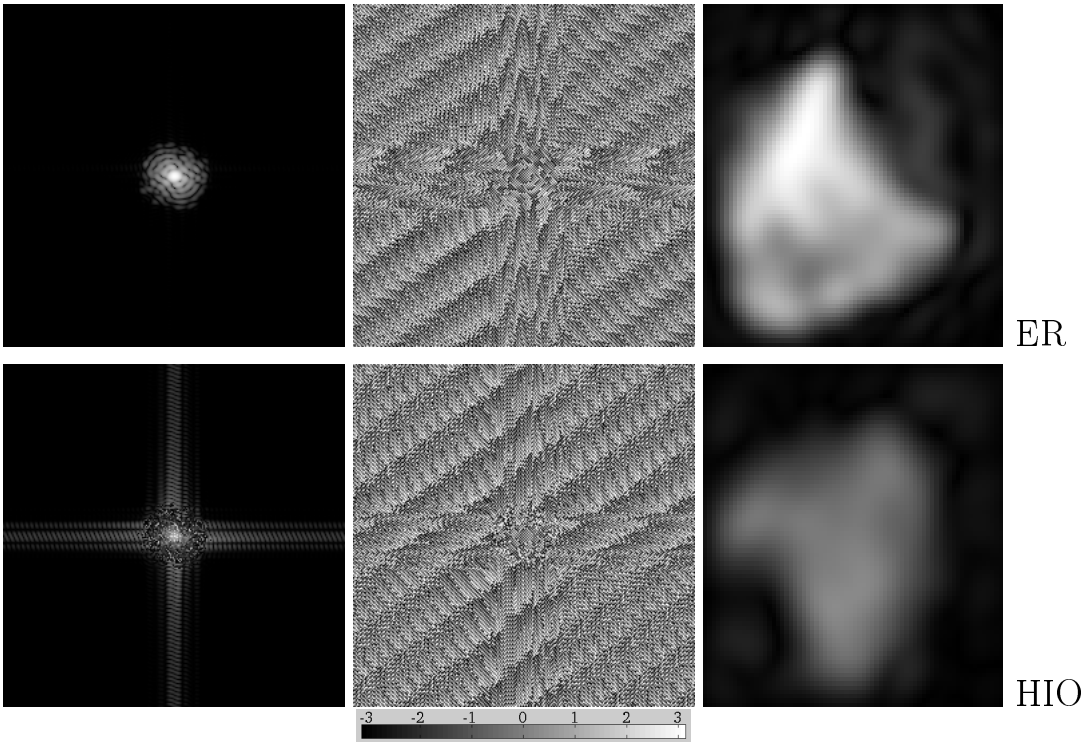

Figure A.1.2: 9×10^4 photons.

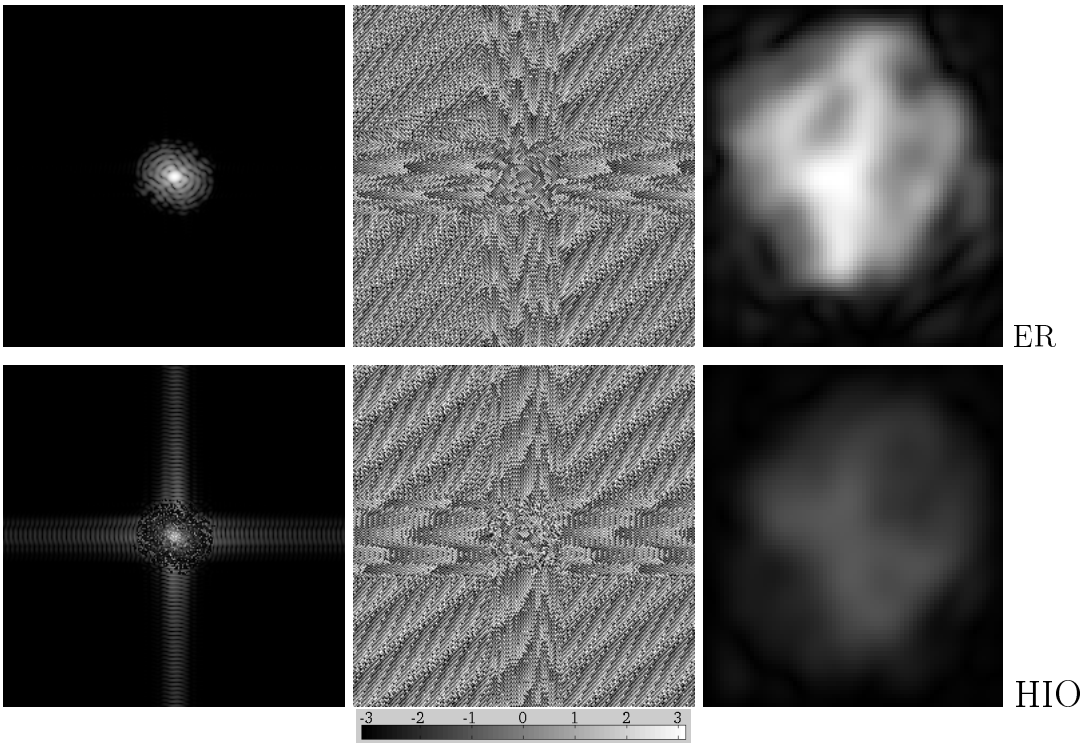

Figure A.1.3: 2×10^5 photons.

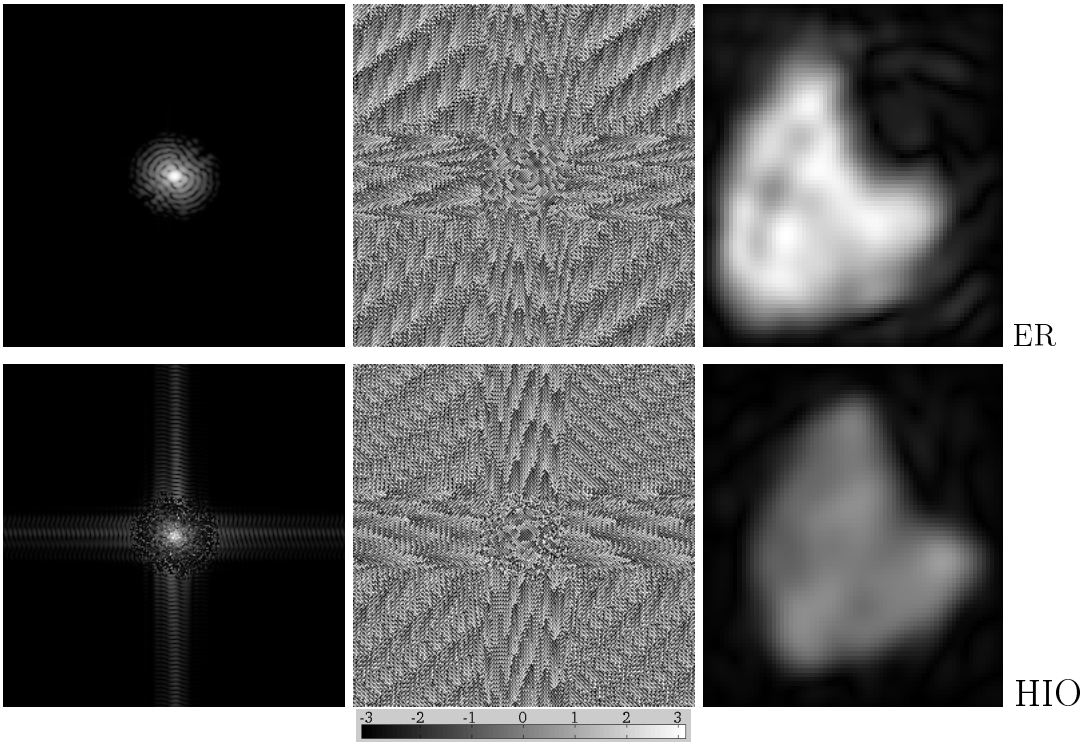

Figure A.1.4: 5×10^5 photons.

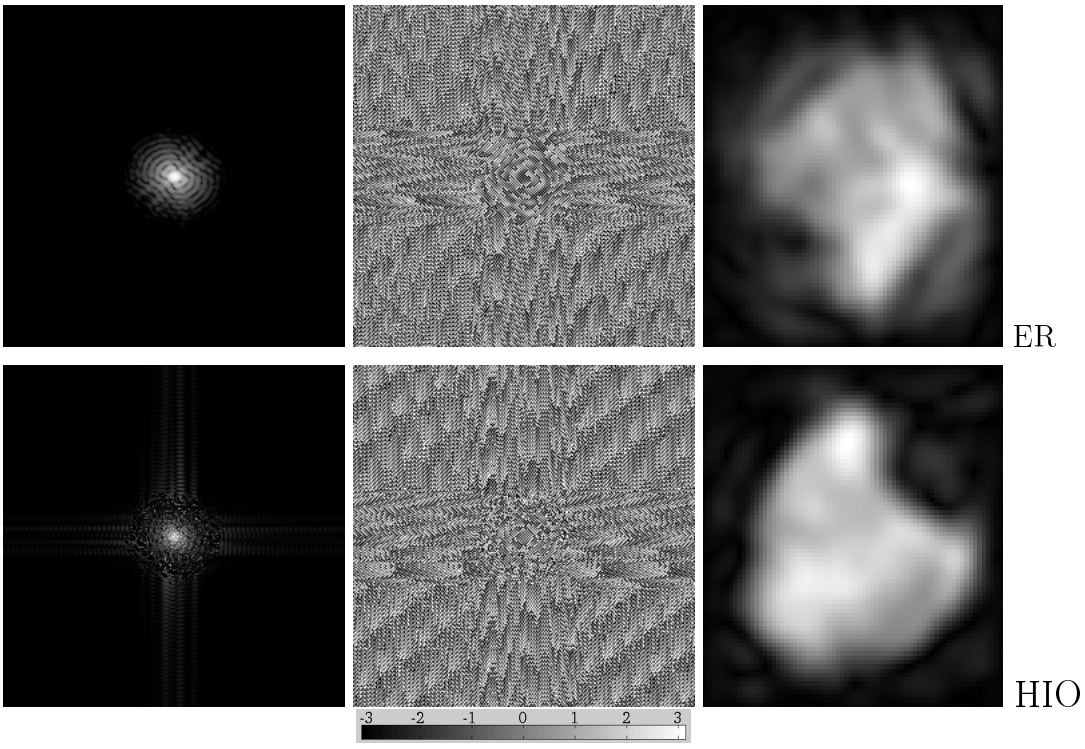

Figure A.1.5: 10^6 photons.

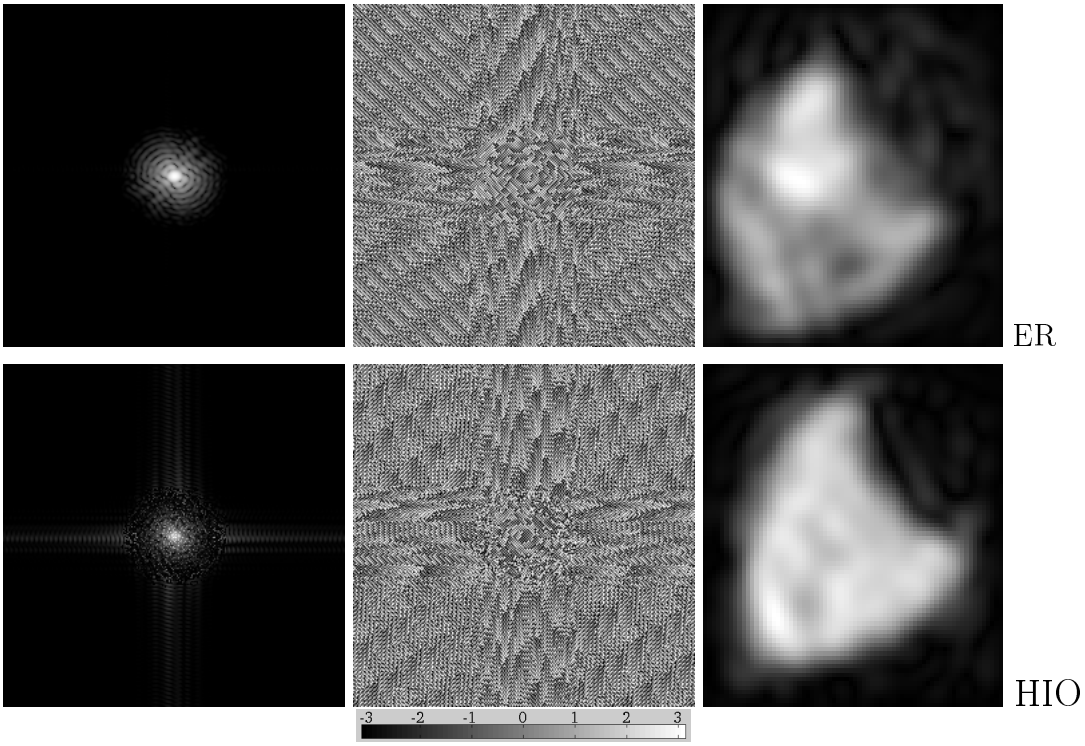

Figure A.1.6: 2×10^6 photons.

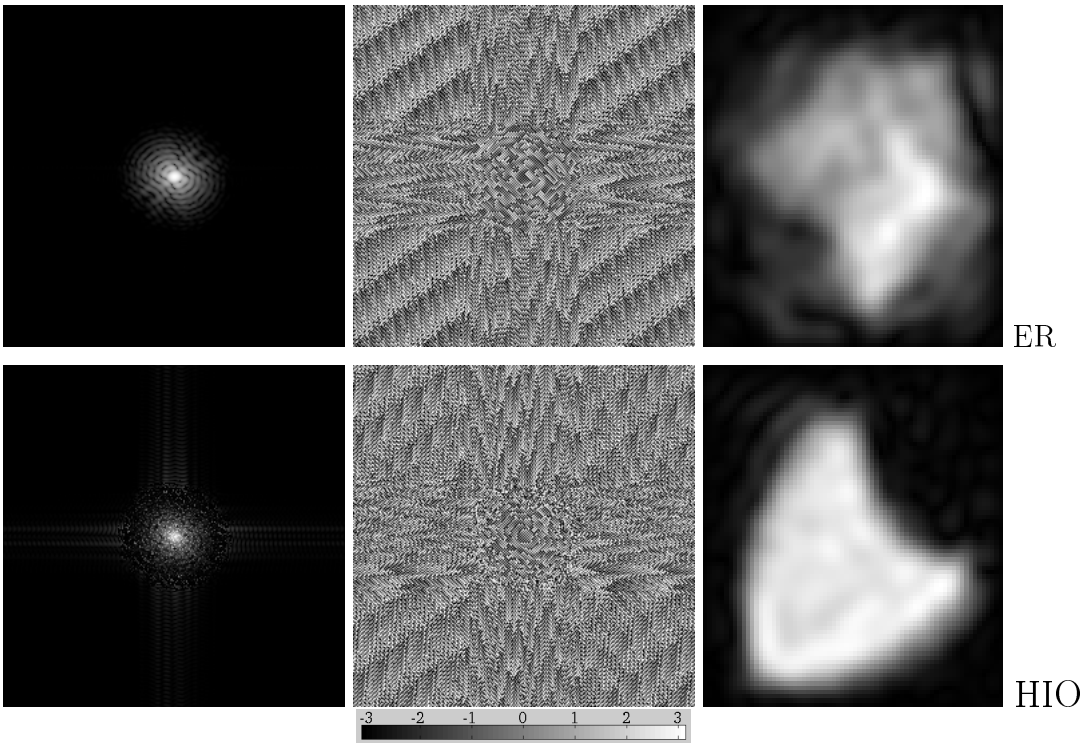

Figure A.1.7: 5×10^6 photons.

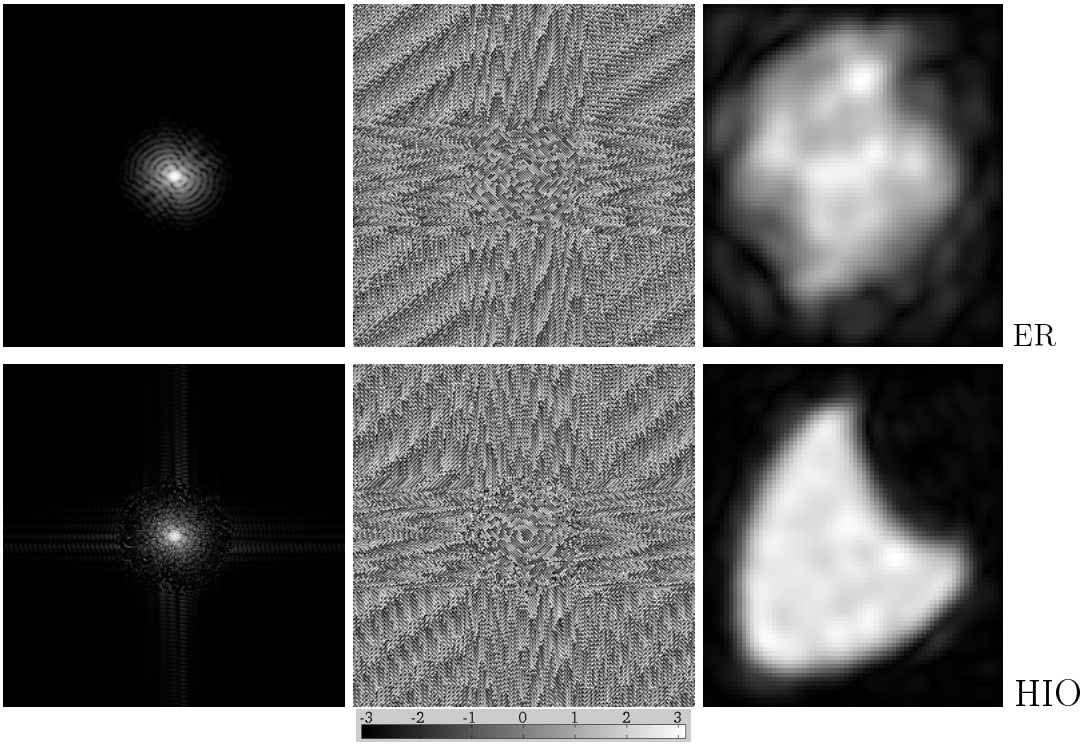

Figure A.1.8: 10^7 photons.

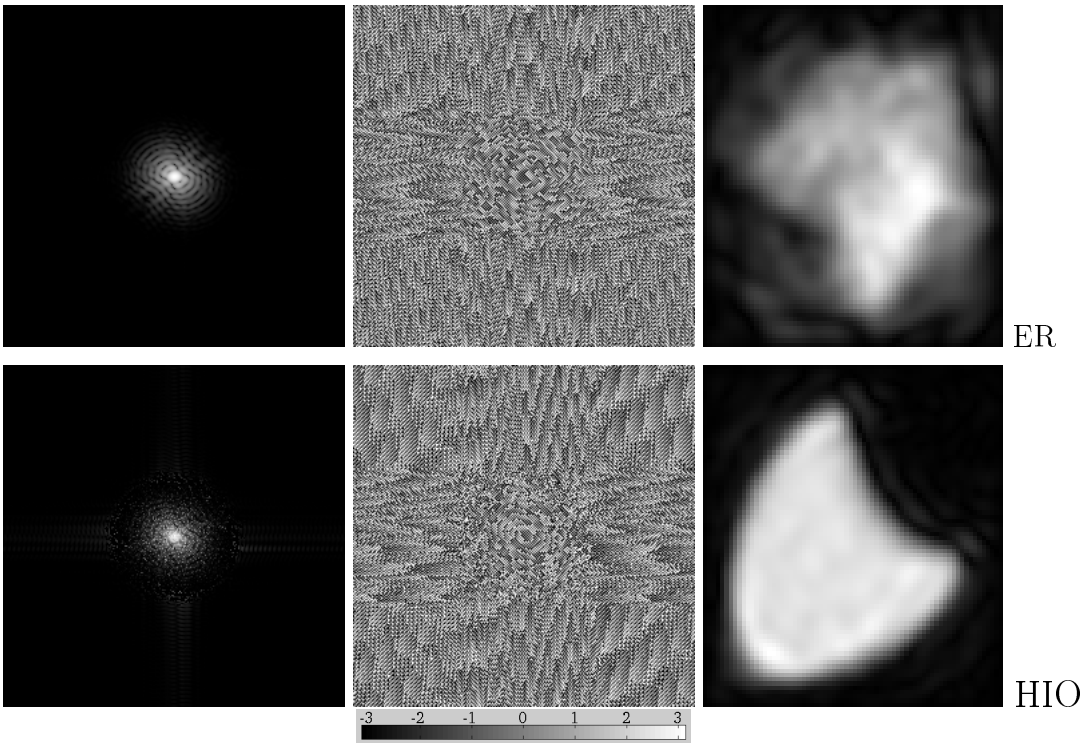

Figure A.1.9: 5×10^7 photons.

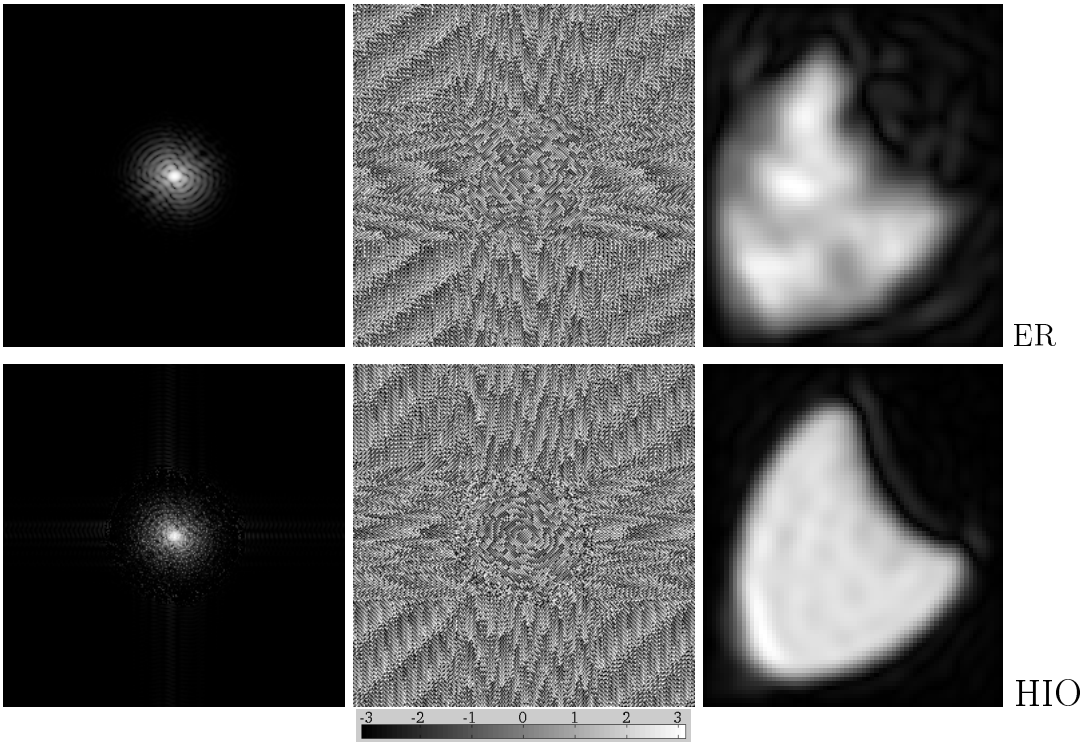

Figure A.1.10: 10^8 photons.

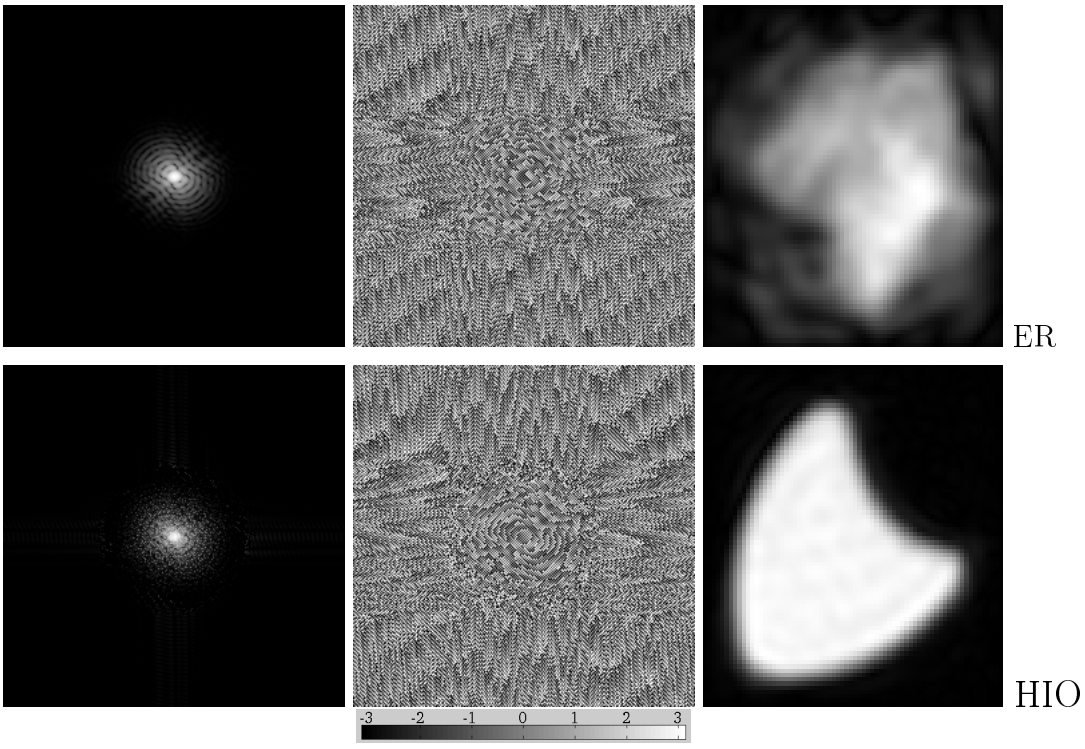

Figure A.1.11: 5×10^8 photons.

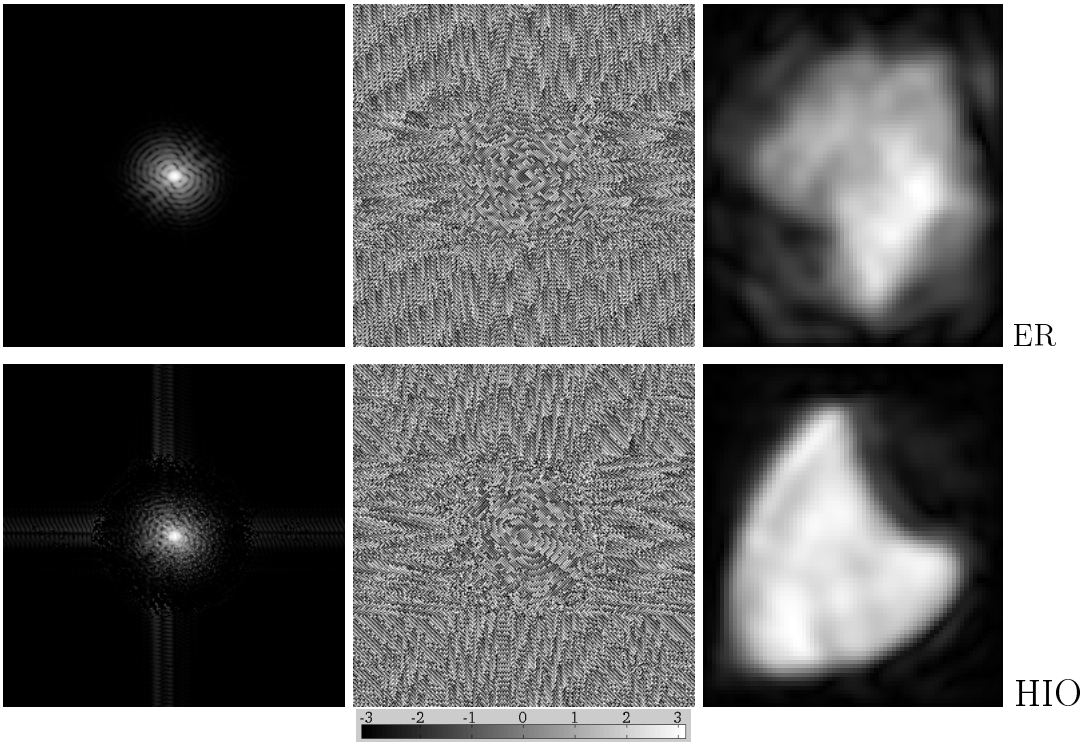

Figure A.1.12: 10^9 photons.

A.2 Alien Scatterers

The results of Section 3.2.2 is shown here.

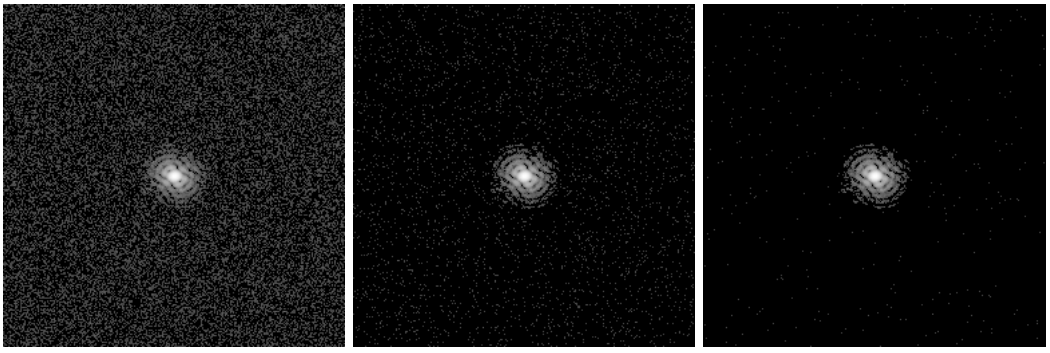

(a) **SNR = 3.53** (b) **SNR = 24.75** (c) **SNR = 137**

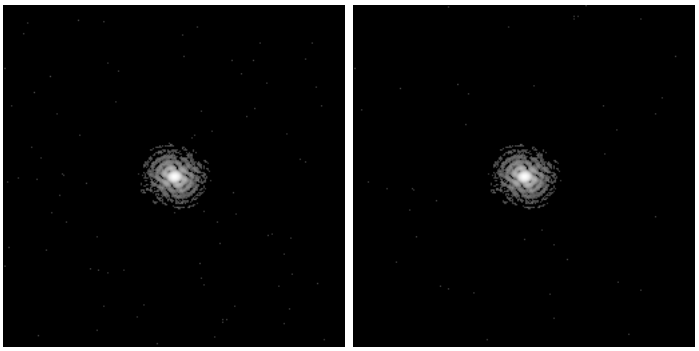

(d) **SNR = 228** (e) **SNR = 258**

Figure A.2.1: All simulated diffraction data for the analysis of Section 3.2.2. From diffraction data with shot-noise for 9×10^4 photons with additional shot-noise due to different amount of alien scatter and corresponding SNR, obtained by the steps (i-iv) of Section 3.1. The alien scattering noise is specified by the alien photon mean of a Poisson distribution from which it is drawn for each pixel. The mean are for these images: (a) 0.5, (b) 0.05, (c) 0.005, (d) 0.0013, (e) 0.0005. The diffraction data are shown in a logarithmic scale.

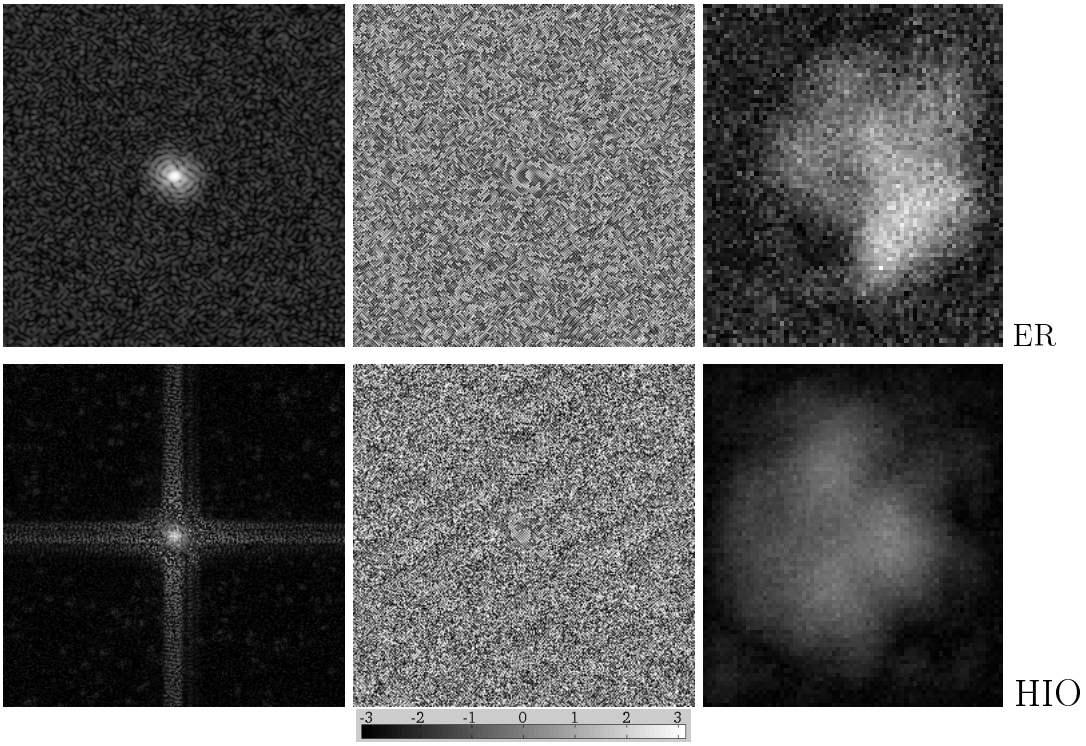

Figure A.2.2: Poisson mean 0.5

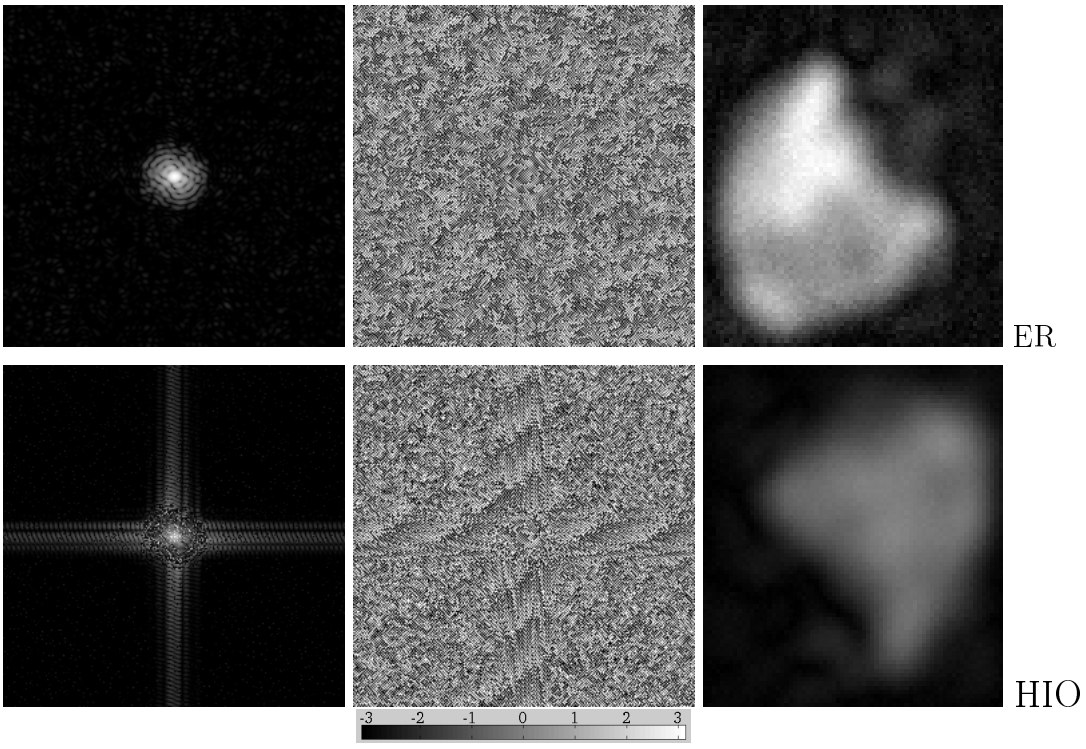

Figure A.2.3: Poisson mean 0.05

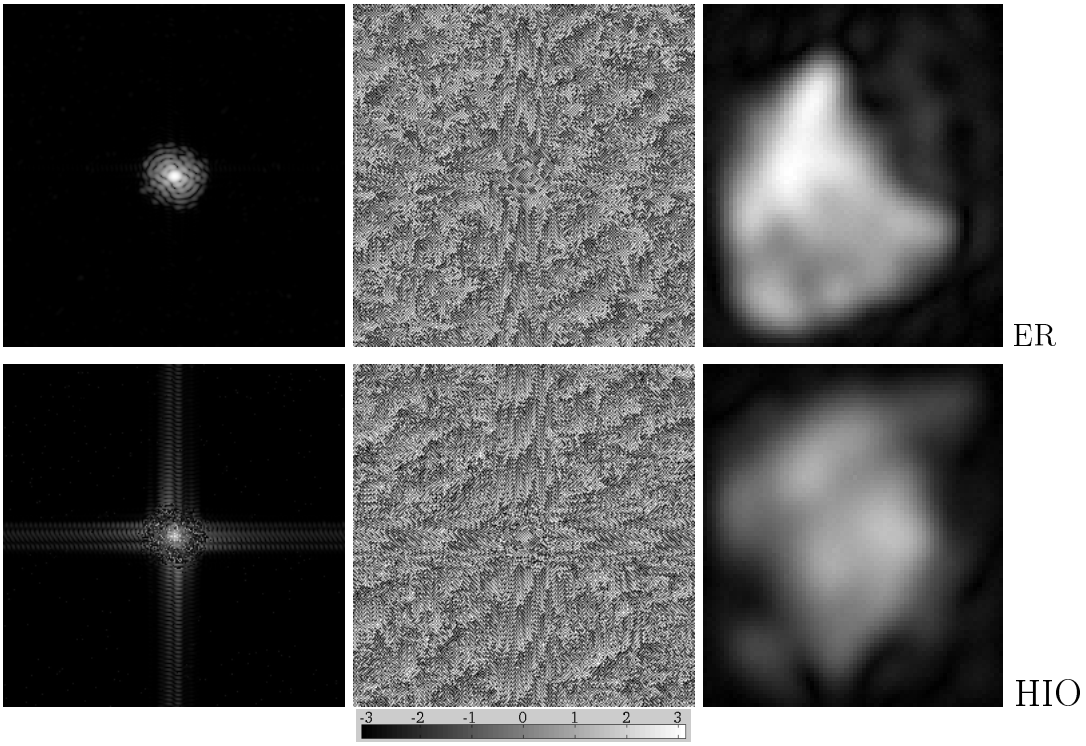

Figure A.2.4: Poisson mean 0.005

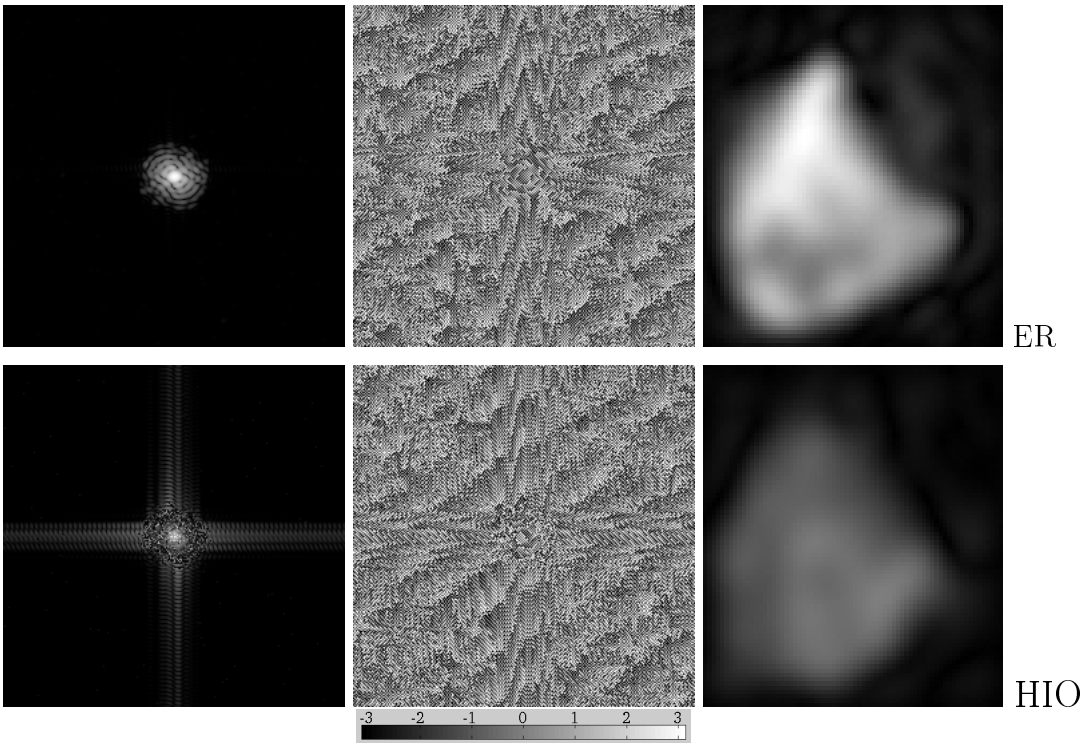

Figure A.2.5: Poisson mean 0.0013

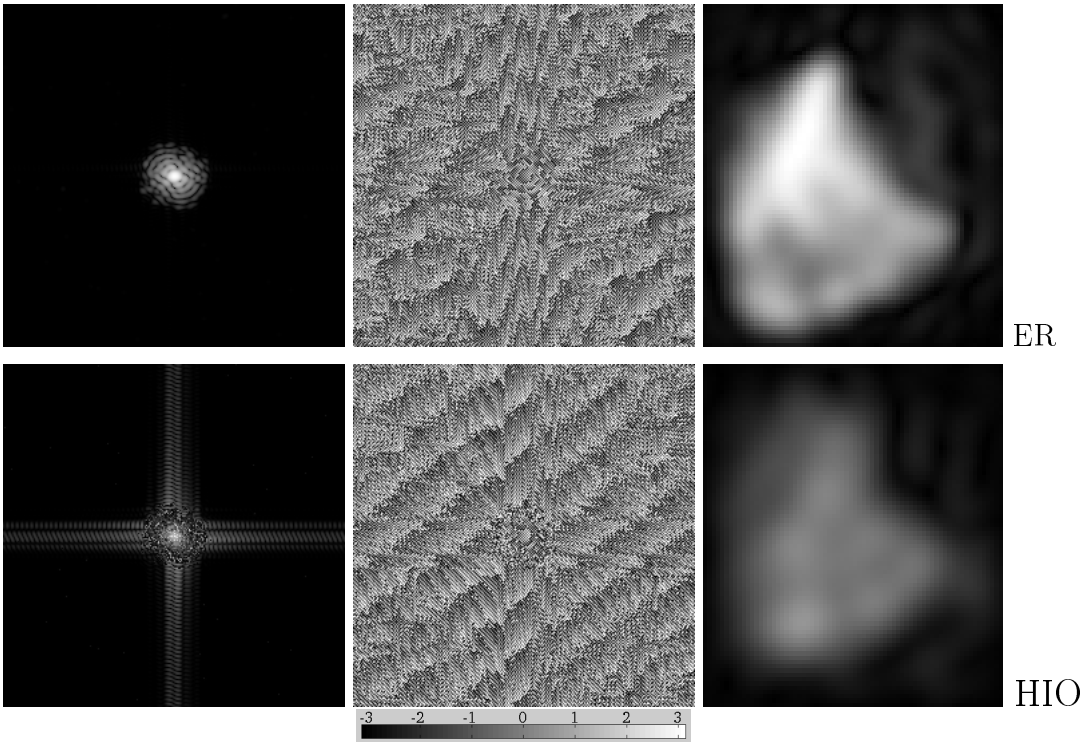

Figure A.2.6: Poisson mean 0.0005

A.3 Incomplete Background Subtraction

The results of Section 3.2.3 is shown here.

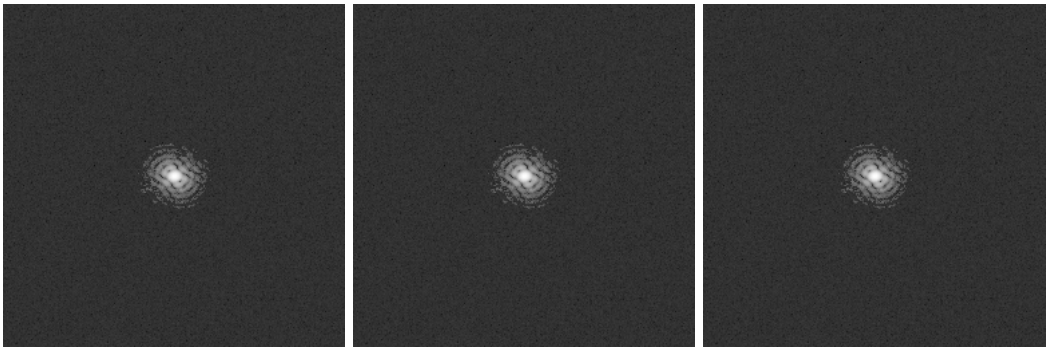

(a) **SNR = 0.442** (b) **SNR = 0.491** (c) **SNR = 0.631**

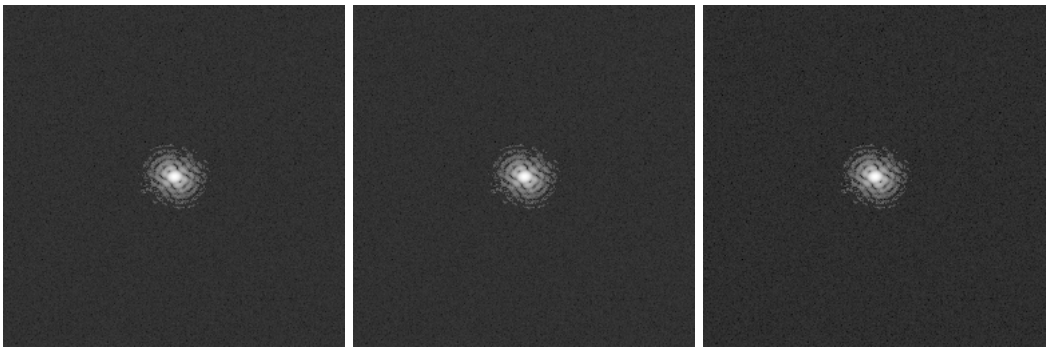

(d) **SNR = 0.882** (e) **SNR = 1.468** (f) **SNR = 4.357**

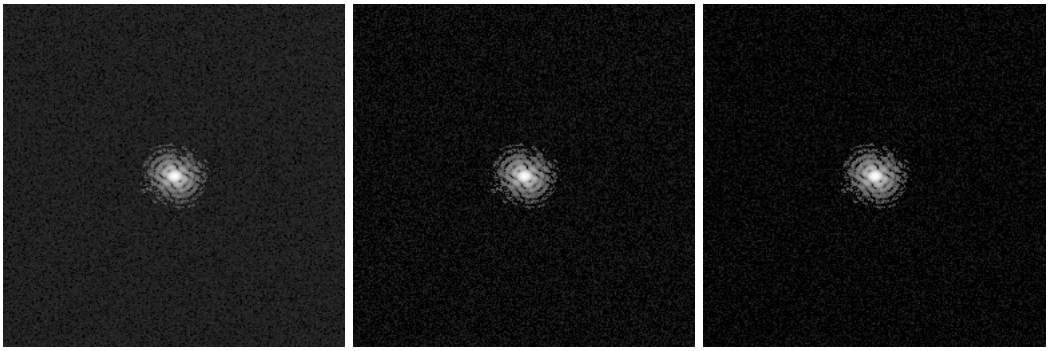

(g) **SNR = 8.524** (h) **SNR = 24.49** (i) **SNR = 35.92**

Figure A.3.1: All simulated diffraction data in the analysis of Section 3.2.3, obtained by the steps (i-v) in Section 3.1. For data with shot-noise inherent for 9×10^4 measured photons, the inherent measured background noise are included by drawing a number in each pixel from a Gaussian distribution with mean 1000 ADUs and standard deviation 27. The amount of background subtracted: (a) 0%, (b) 10%, (c) 30%, (d) 50%, (e) 70%, (f) 90%, (g) 95%, (h) 99%, (i) 100%. The diffraction data are shown in a logarithmic scale.

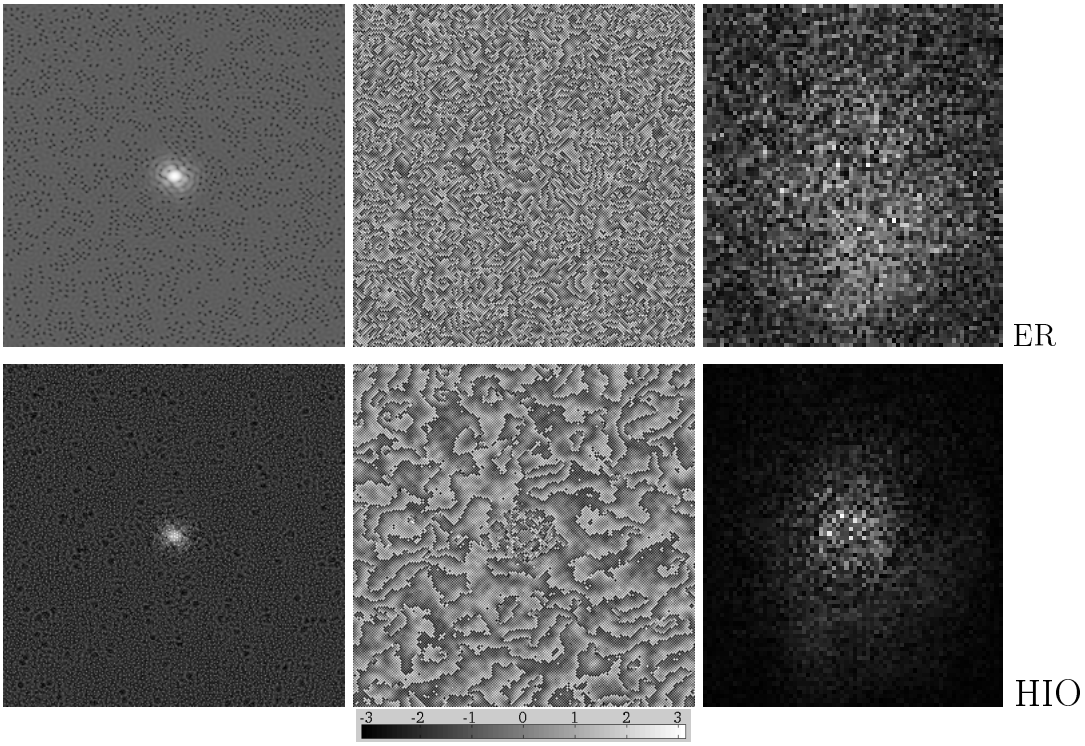

Figure A.3.2: 0% background subtracted

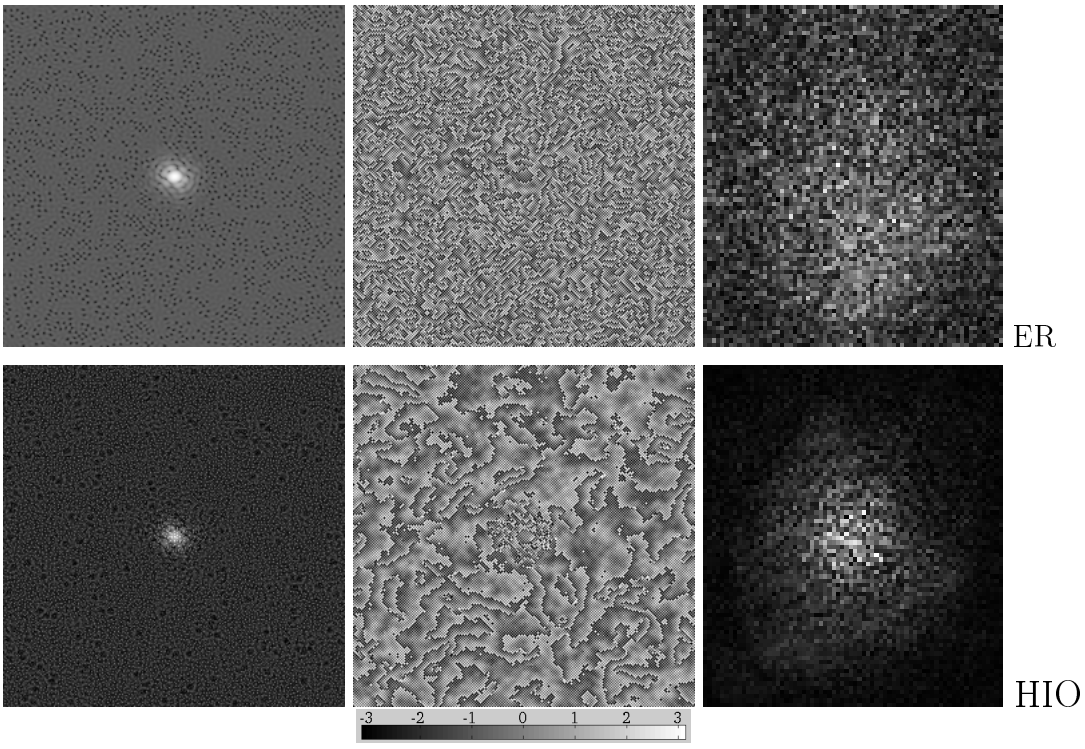

Figure A.3.3: 10% background subtracted

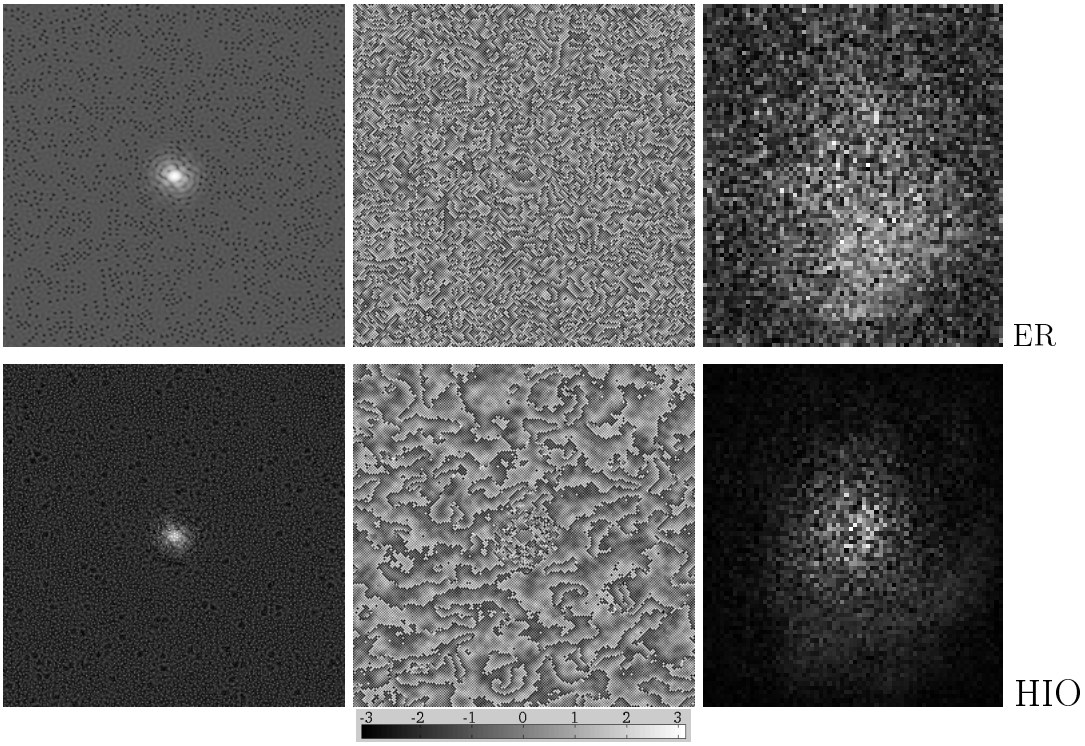

Figure A.3.4: 30% background subtracted

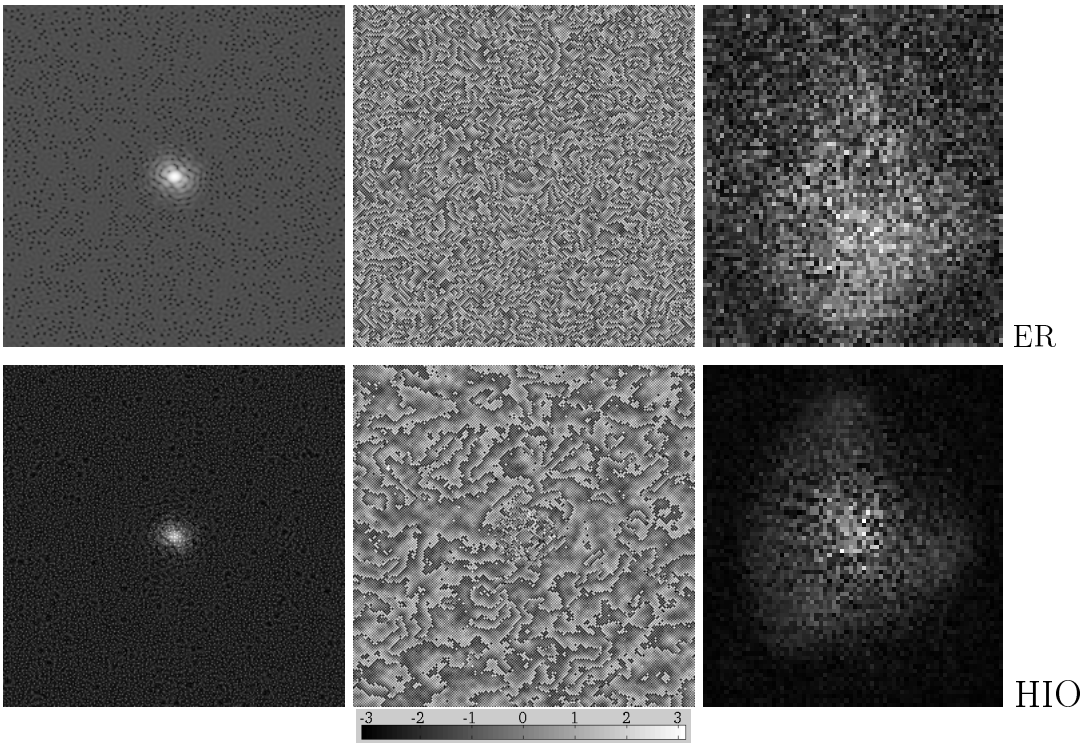

Figure A.3.5: 50% background subtracted

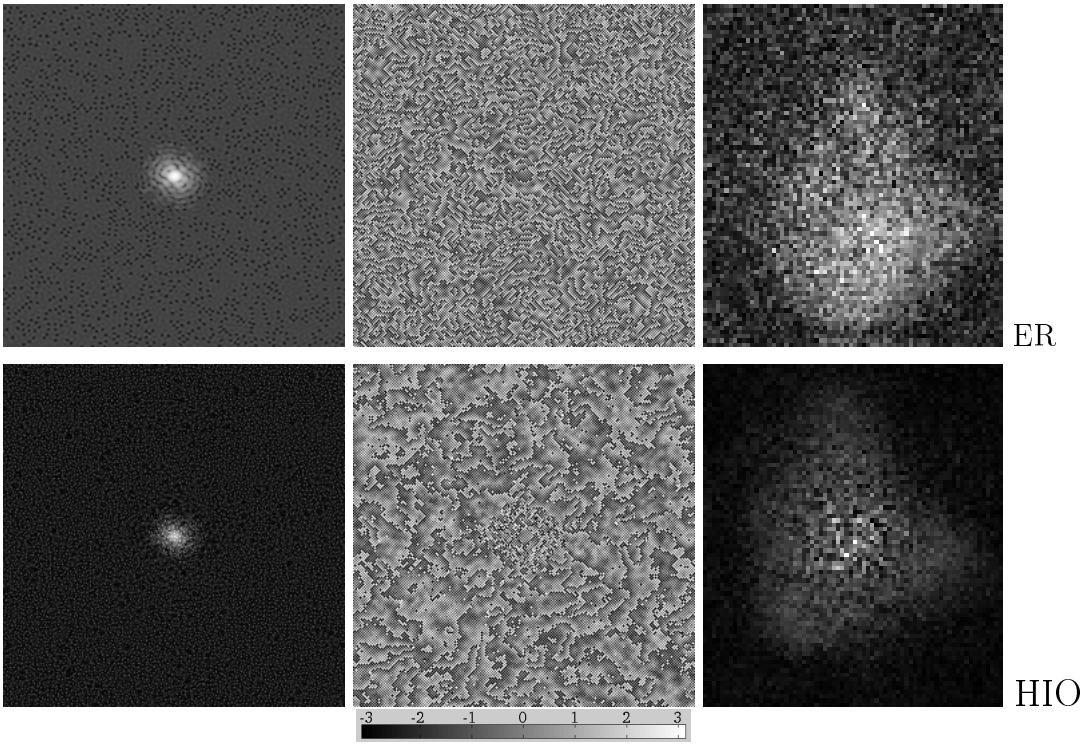

Figure A.3.6: 70% background subtracted

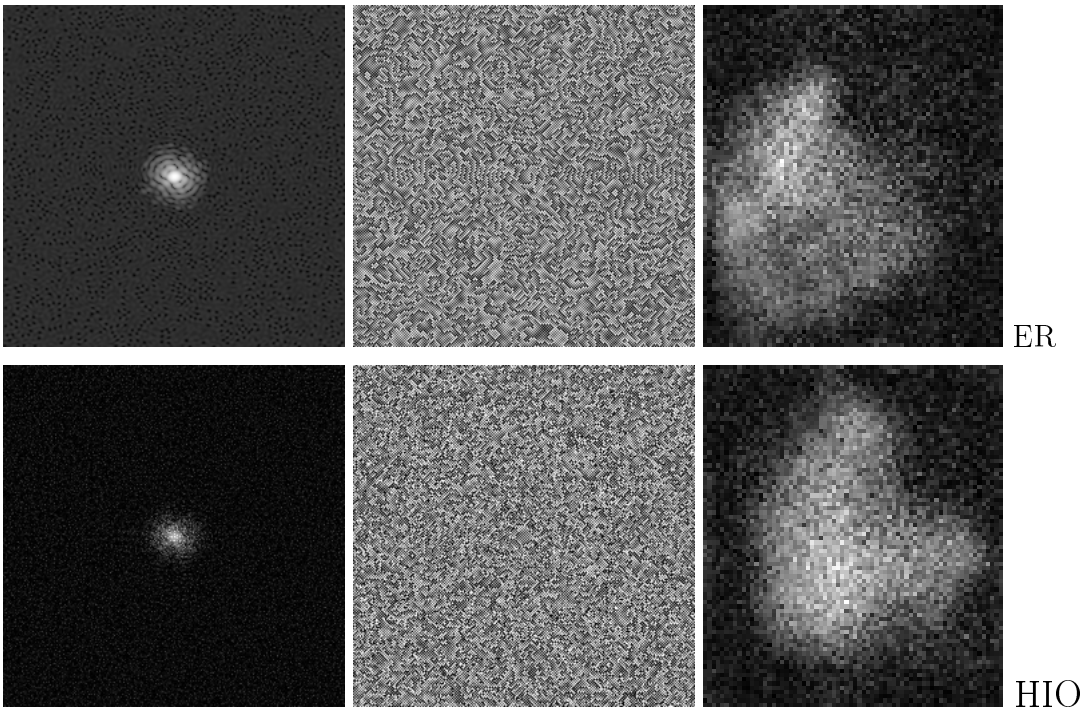

Figure A.3.7: 90% background subtracted

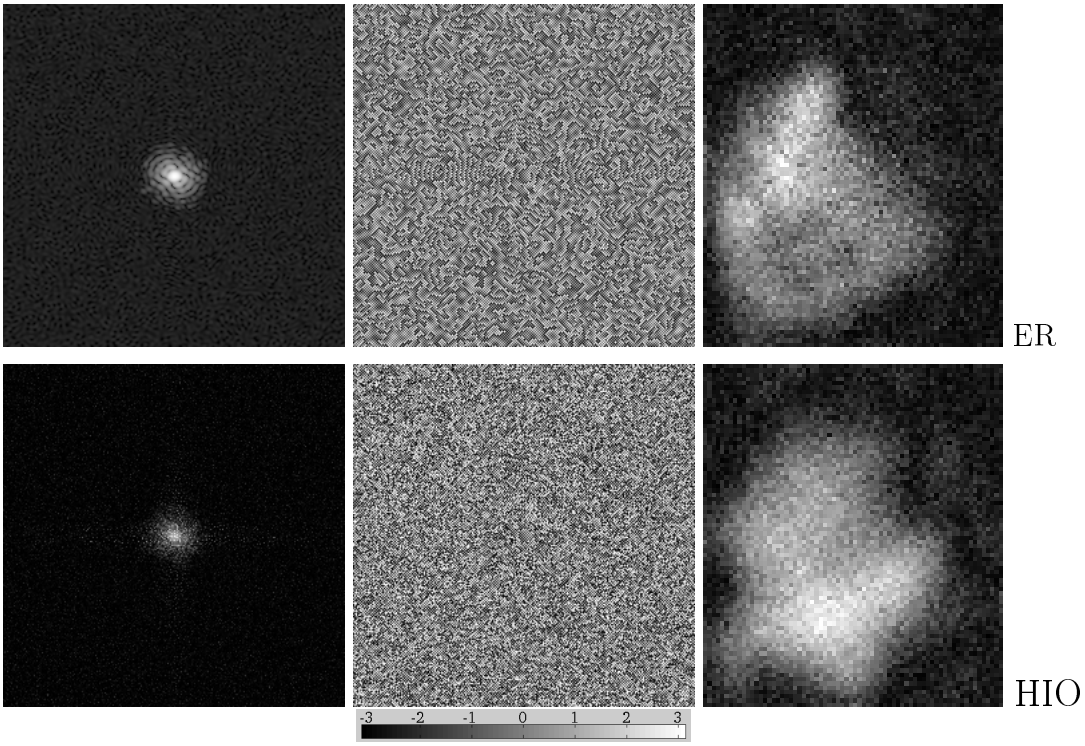

Figure A.3.8: 95% background subtracted

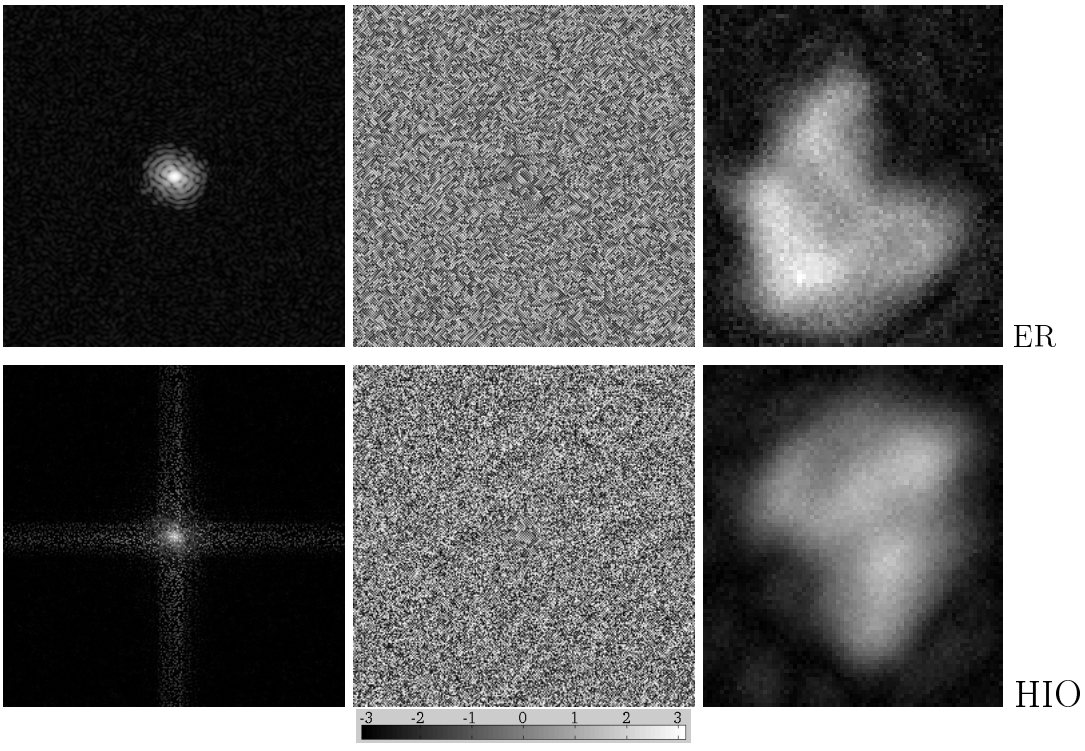

Figure A.3.9: 99% background subtracted

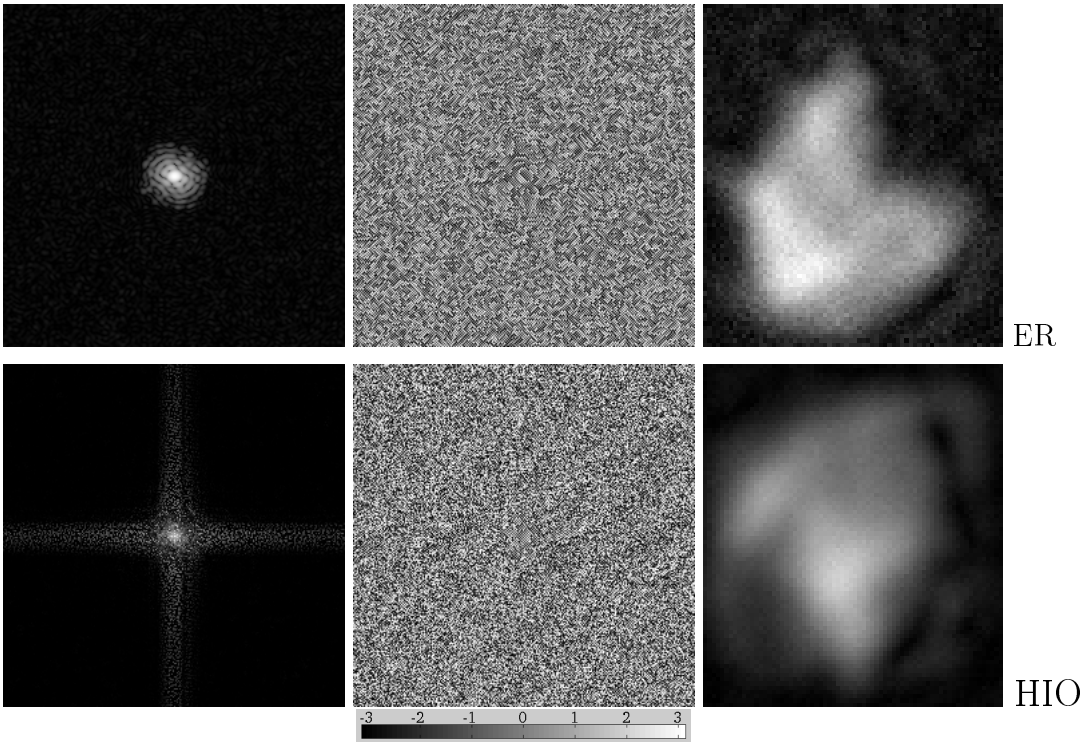

Figure A.3.10: 100% background subtracted

Appendix B

Reconstructions from Chapter 4 Noise-Added Simulation for Fresnel Coherent Diffractive Imaging

This appendix contains all simulated diffraction data (white-field data omitted) and the respective reconstructed solutions, for Section 4.3.2 (Photon number), and Section 4.3.3 (Incomplete background subtraction; Case I-III).
In Appendix B.1 (Photon number), the first figure shows the entire range of diffraction data with different amount of measured photons (with equal amount of measured photons in the white-field data, not shown). In the following figures the respective solution ($\pi_m^F \rho_{125}^1$) by ER and HIO are shown, and it's derived transmission function.
In Appendix B.2 (Incomplete background subtraction), the first figure shows the entire range of diffraction data with shot-noise for 10^9 measured photons and 0-100% background subtracted (used in cases I-III). In the following Appendices B.2.1-B.2.3 (Case I-III) the solutions from the diffraction and white-field data (with shot-noise for 10^9 measured photons), stated with how much background was subtracted respectively. The abbreviations DPD (diffraction pattern data), and WFD (white-field data) are used.

For all solutions in this appendix, four entities of the solution are shown (support region) for ER and HIO respectively: top row; magnitude of solution (left), phase of solution (right): bottom row; magnitude of the solution's transmission function, phase of the solution's transmission function.

Furthermore in Appendix B.2.4, we see the error metrics ξ_1^0, ξ_1^2, χ^2, ${}^{TF}\xi_1^0$, ${}^{TF}\xi_1^2$, ${}^{TF}\chi^2$ for all tests of Chapter 4, but comparing magnitude and phase entities rather than the complex ones as in Chapter 4. For the error metrics of Section 4.3.3 only the one's of shot-noise for 10^9 measured photons are shown.

B.1 Photon Number

The results of Section 4.3.2 is shown here.

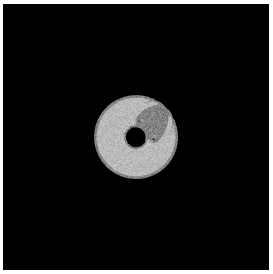

(a) **SNR = 19, 5×10^5 photons.**

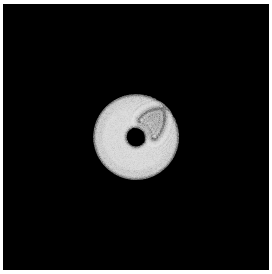

(b) **SNR = 24, 10^6 photons.**

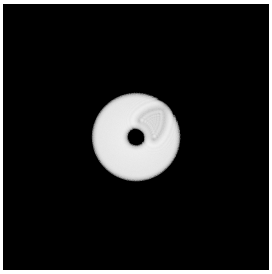

(c) **SNR = 50, 5×10^6 photons.**

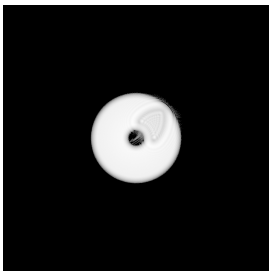

(d) **SNR = 218, 10^8 photons.**

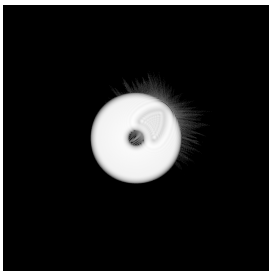

(e) **SNR = 686, 10^9 photons.**

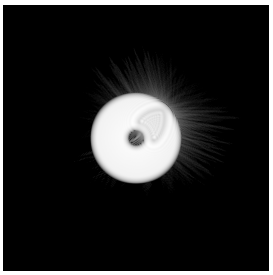

(f) **SNR = 1525, 5×10^9 photons.**

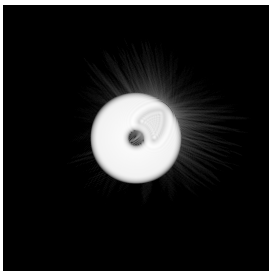

(g) **SNR = 2152, 10^{10} photons.**

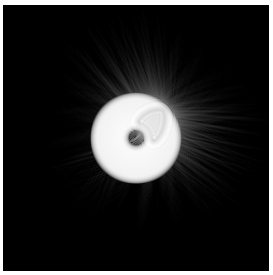

(h) **SNR = 4789, 5×10^{10} photons.**

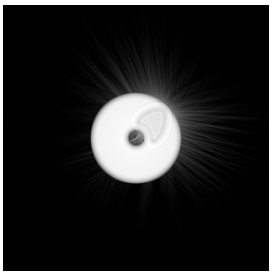

(i) **SNR = 6762, 10^{11} photons.**

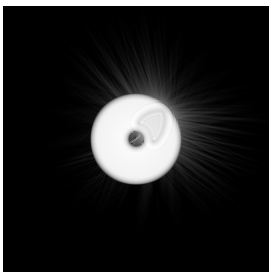

(j) **SNR = 21315, 10^{12} photons.**

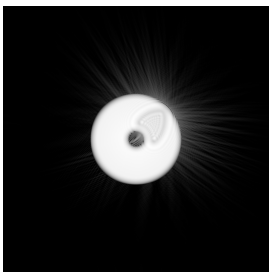

(k) **SNR = 212923, 10^{14} photons.**

Figure B.1.1: All simulated diffraction data in the analysis of Section 4.3.2, obtained by the steps (i-iv) in Section 4.2, for different number of measured photons and corresponding SNR. The white-field data has the same amount of measured photons with inherent shot-noise, not included here. The diffraction data are shown in a logarithmic scale. Note that each image display similar brightness since each image is normalised to its own highest value. But they differ by orders of magnitude since different photon number yields different scaling in real and reciprocal space.

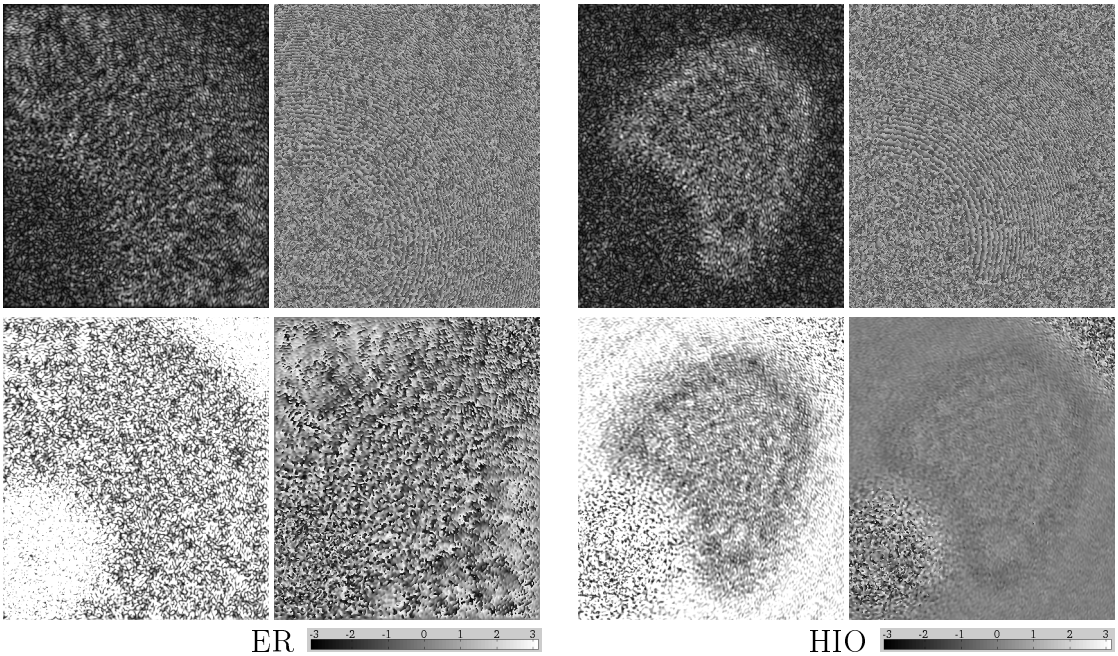

Figure B.1.2: **SNR = 19, 5×10^5 photons.**

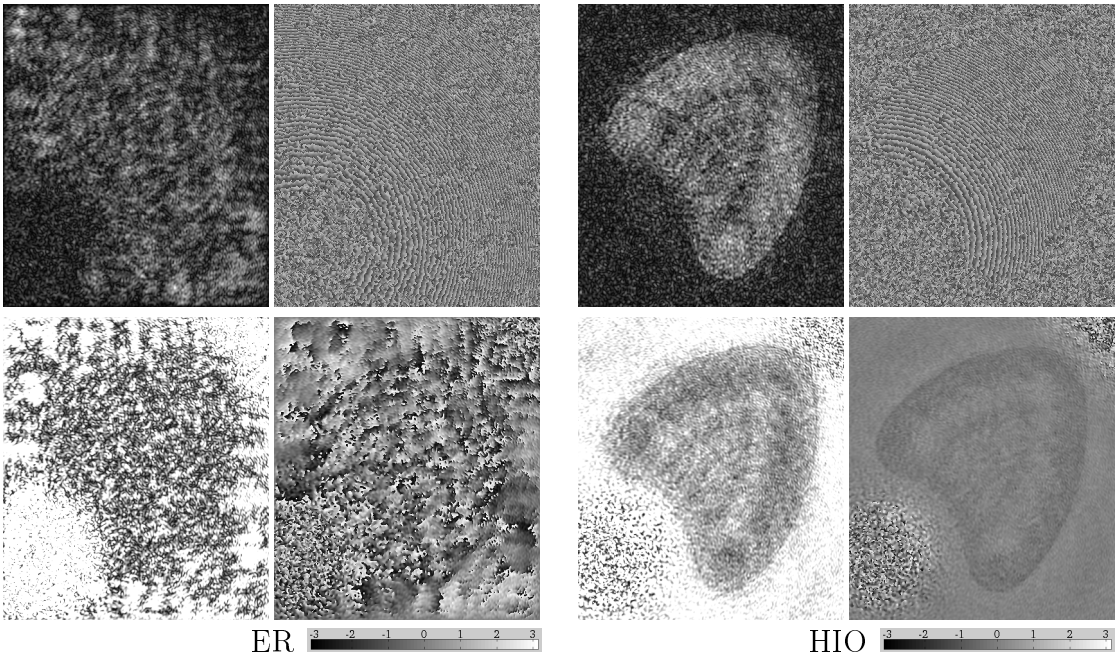

Figure B.1.3: **SNR = 24, 10^6 photons.**

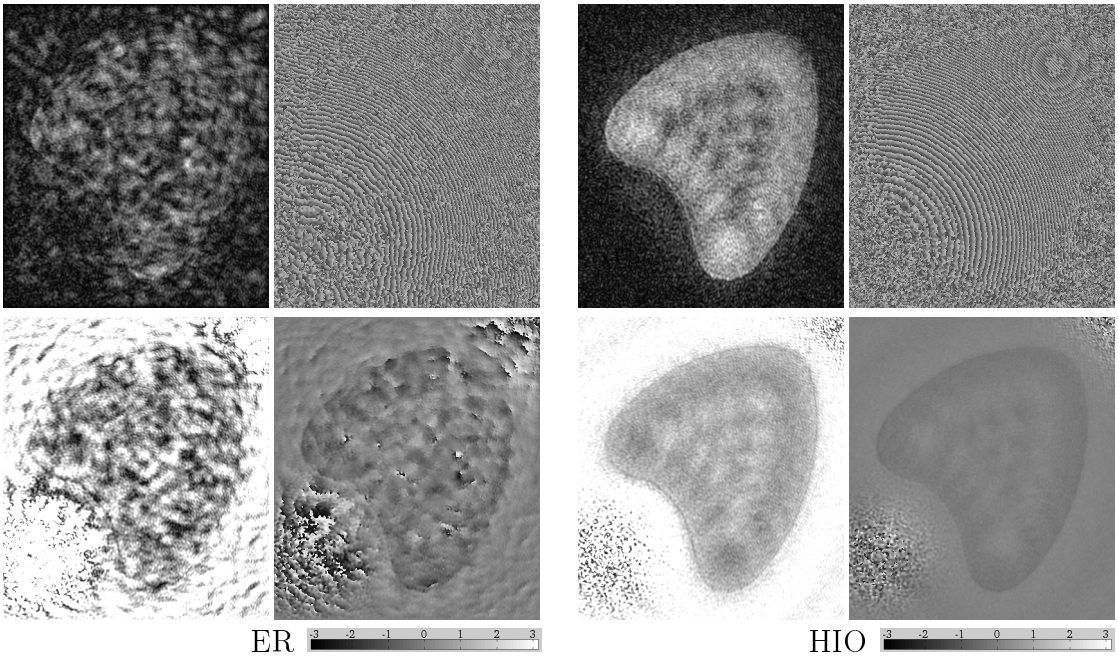

Figure B.1.4: **SNR = 50, 5×10^6 photons.**

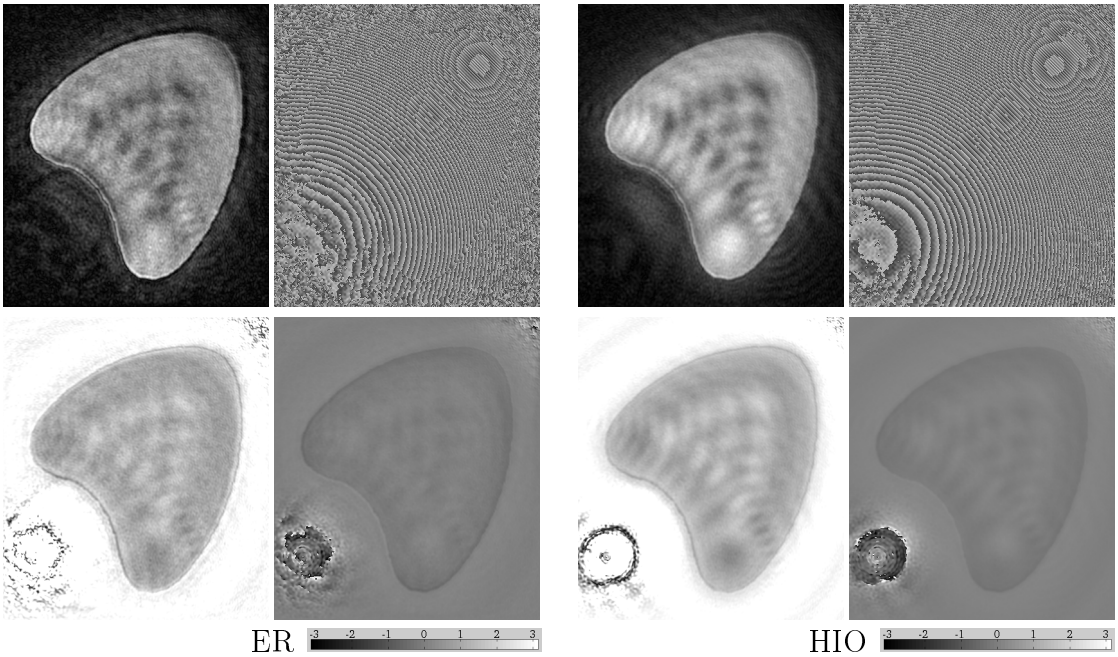

Figure B.1.5: **SNR = 218, 10^8 photons.**

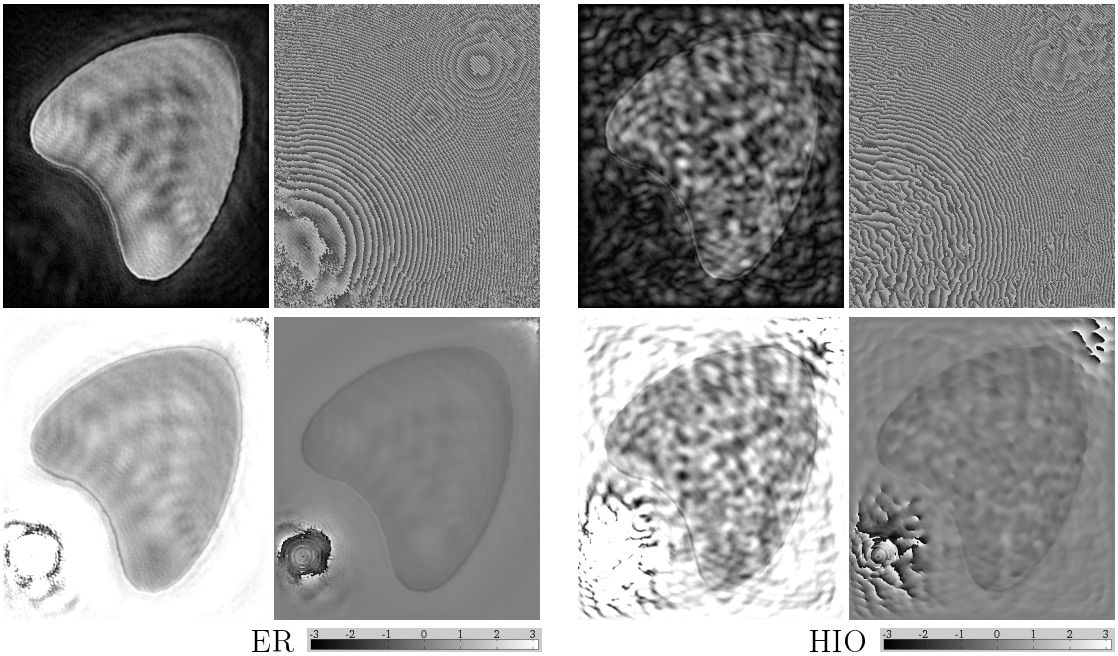

Figure B.1.6: **SNR = 686, 10^9 photons.**

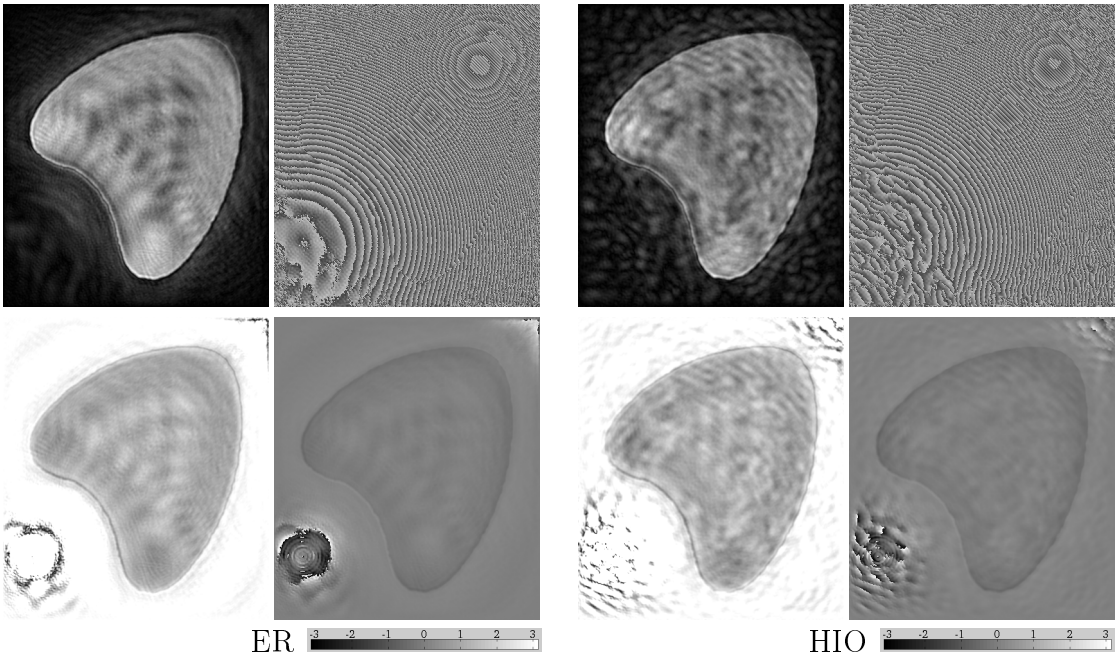

Figure B.1.7: **SNR = 1525, 5×10^9 photons.**

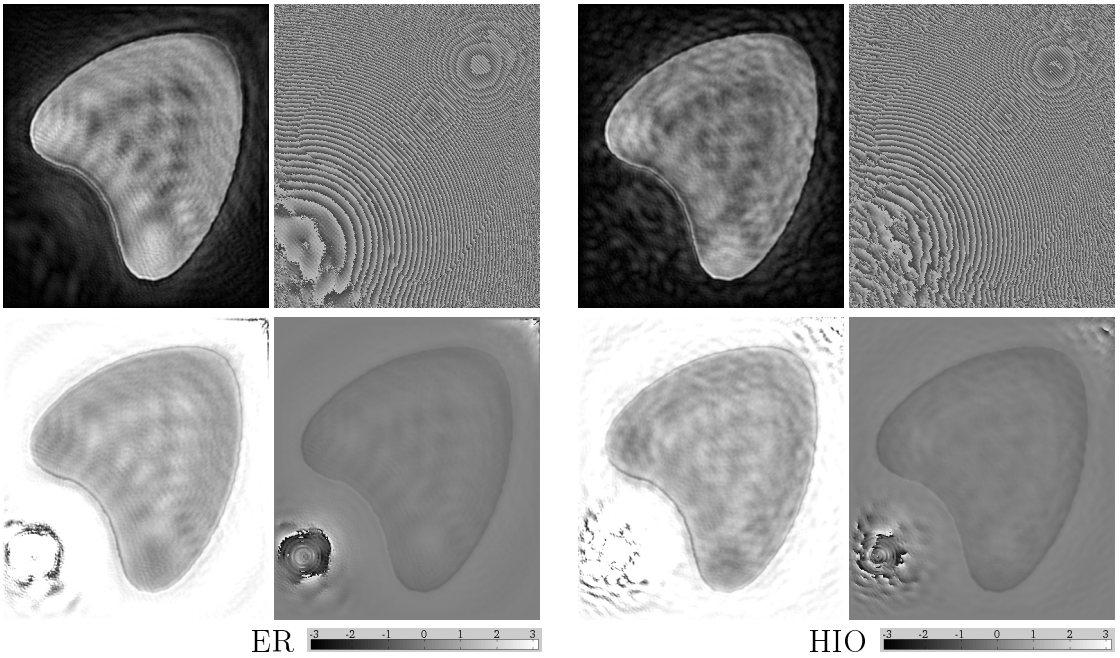

Figure B.1.8: **SNR = 2152, 10^{10} photons.**

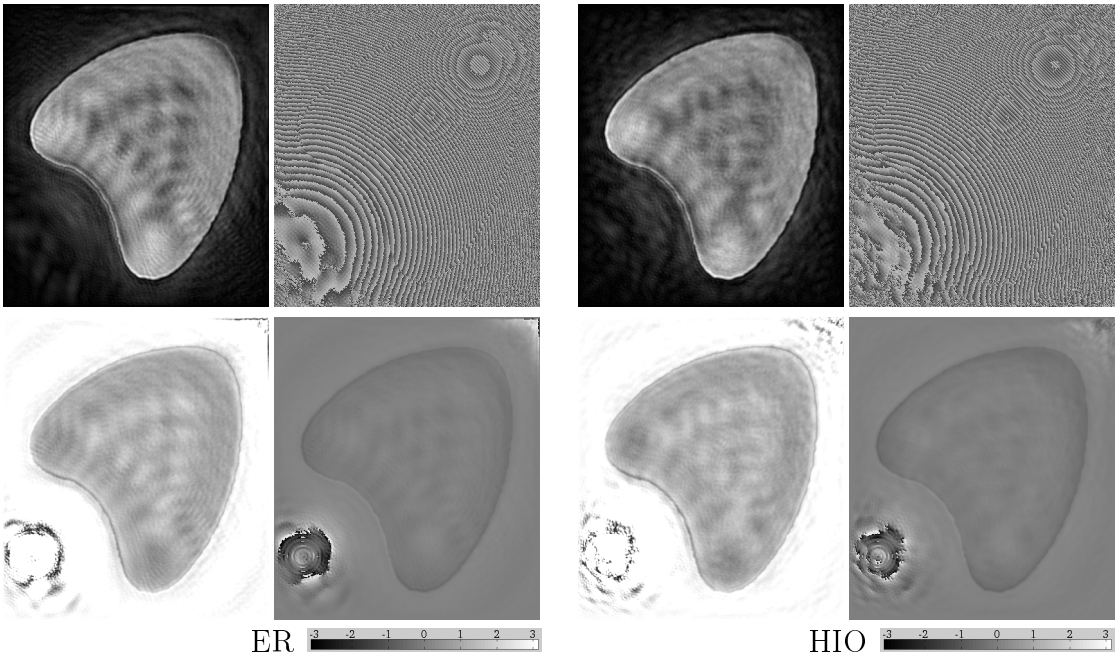

Figure B.1.9: **SNR = 4789, 5×10^{10} photons.**

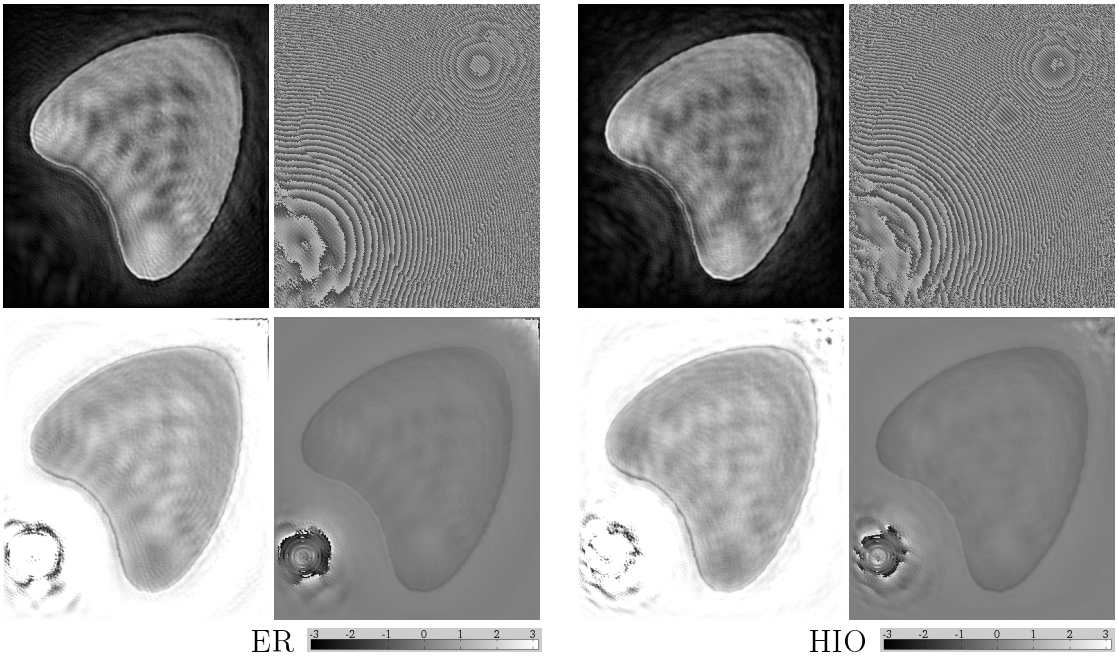

Figure B.1.10: **SNR = 6762, 10^{11} photons.**

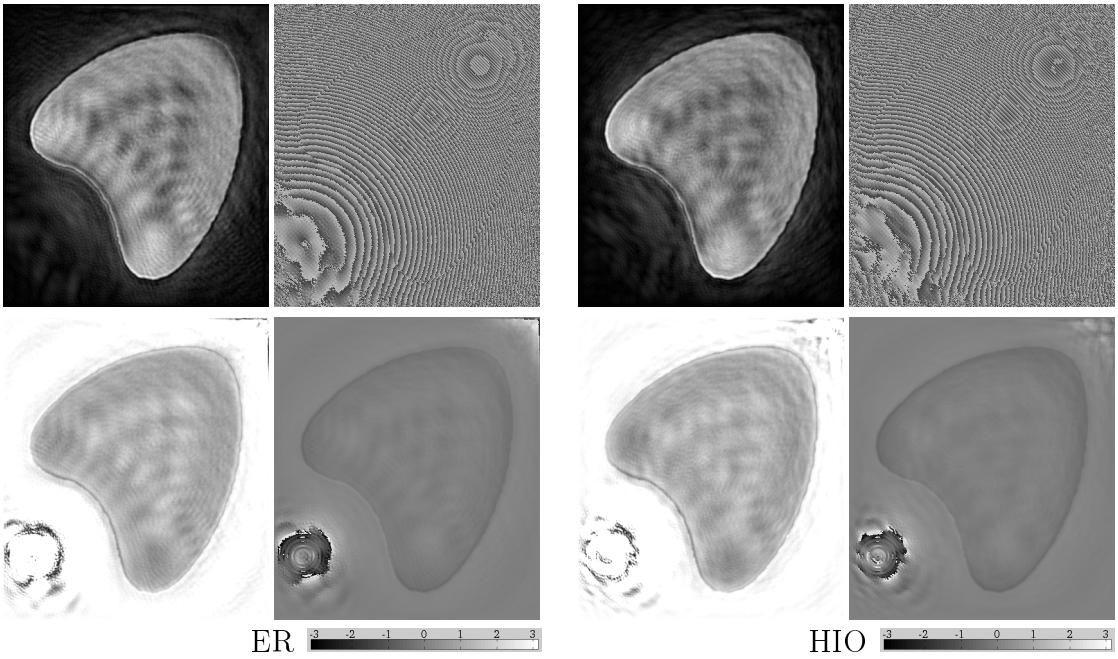

Figure B.1.11: **SNR = 21315, 10^{12} photons.**

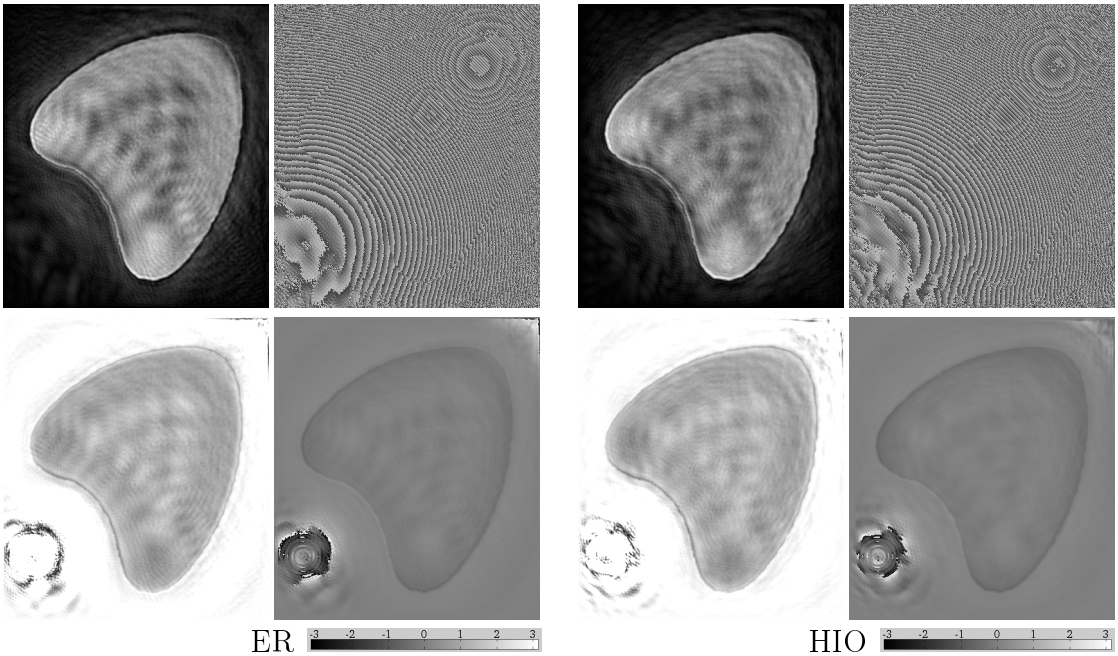

Figure B.1.12: **SNR = 212923, 10^{14} photons.**

B.2 Incomplete Background Subtraction

The results of Section 4.3.3 is shown here.

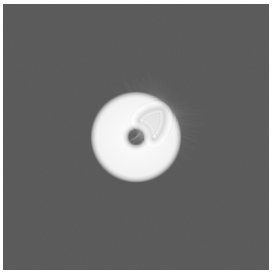

(a) **SNR = 1.8; 0% mean background subtracted**

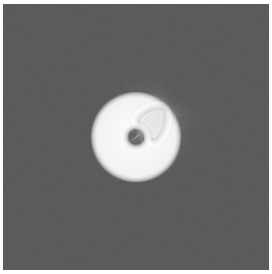

(b) **SNR = 2; 10% mean background subtracted**

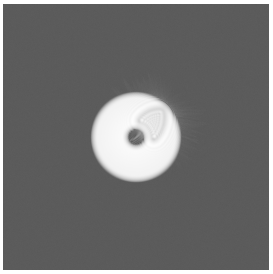

(c) **SNR = 2.5; 30% mean background subtracted**

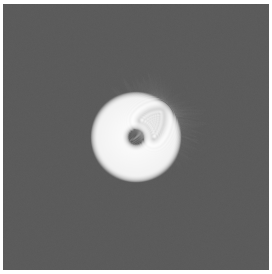

(d) **SNR = 3.5; 50% mean background subtracted**

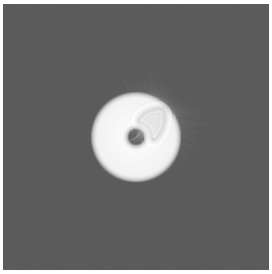

(e) **SNR = 5.9; 70% mean background subtracted**

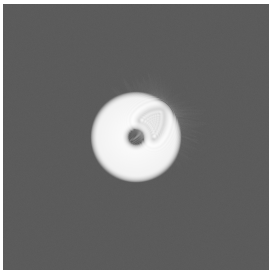

(f) **SNR = 17.4; 90% mean background subtracted**

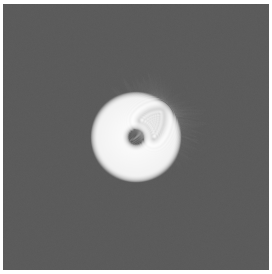

(g) **SNR = 33.9; 95% mean background subtracted**

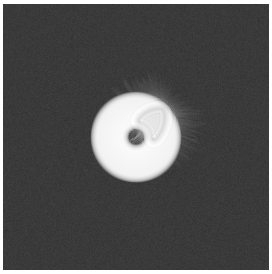

(h) **SNR = 139.3; 99% mean background subtracted**

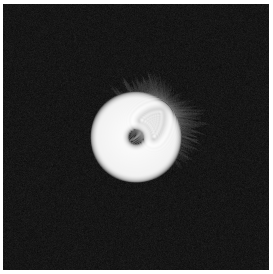

(i) **SNR = 338.9; 100% mean background subtracted**

Figure B.2.1: All simulated diffraction data used in Section 4.3.3 with shot-noise for 10^9 measured photons, and different amount of background subtracted, obtained by steps (i-v) of Section 4.2. These SNR range of the diffraction data were used for all tests with different comparison means to background subtracted white-field data, that has equal amount of shot-noise.

B.2.1 Case (I)

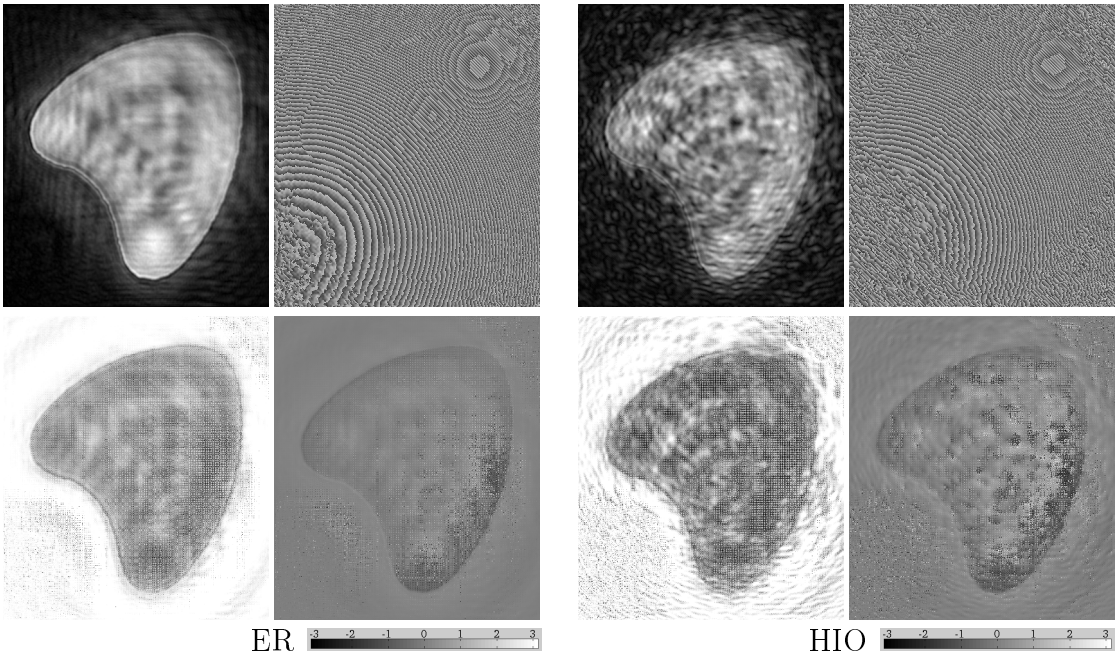

Figure B.2.2: **Background subtracted: 0% in DPD (SNR = 1.8), 0% in WFD.**

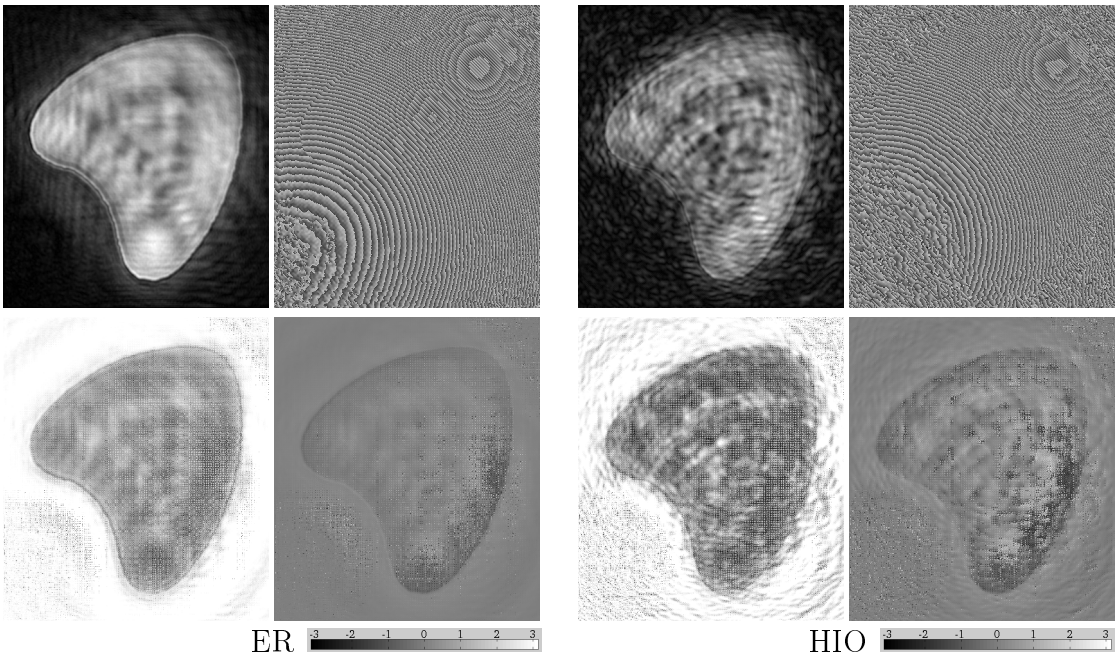

Figure B.2.3: **Background subtracted: 10% in DPD (SNR = 2), 10% in WFD.**

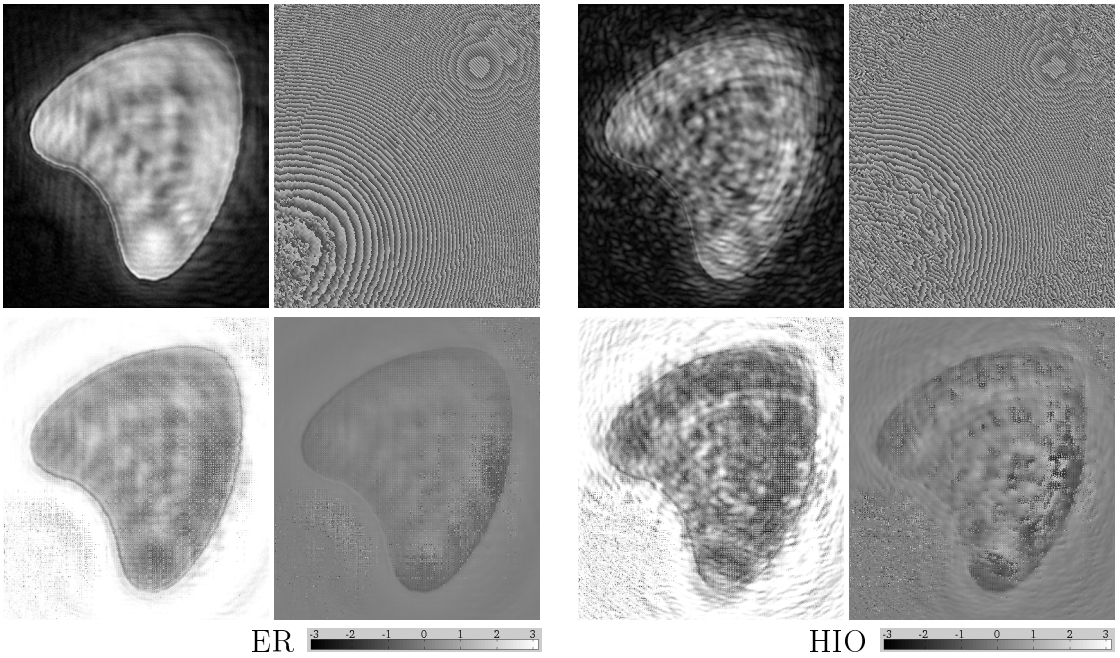

Figure B.2.4: **Background subtracted: 30% in DPD (SNR = 2.5), 30% in WFD.**

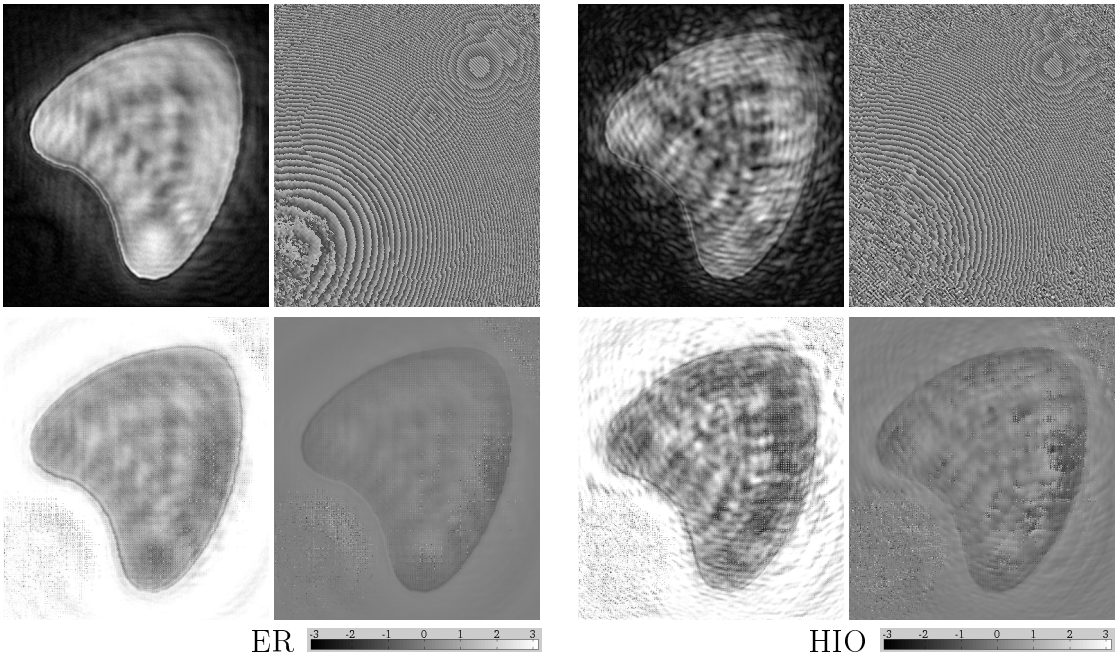

Figure B.2.5: **Background subtracted: 50% in DPD (SNR = 3.5), 50% in WFD.**

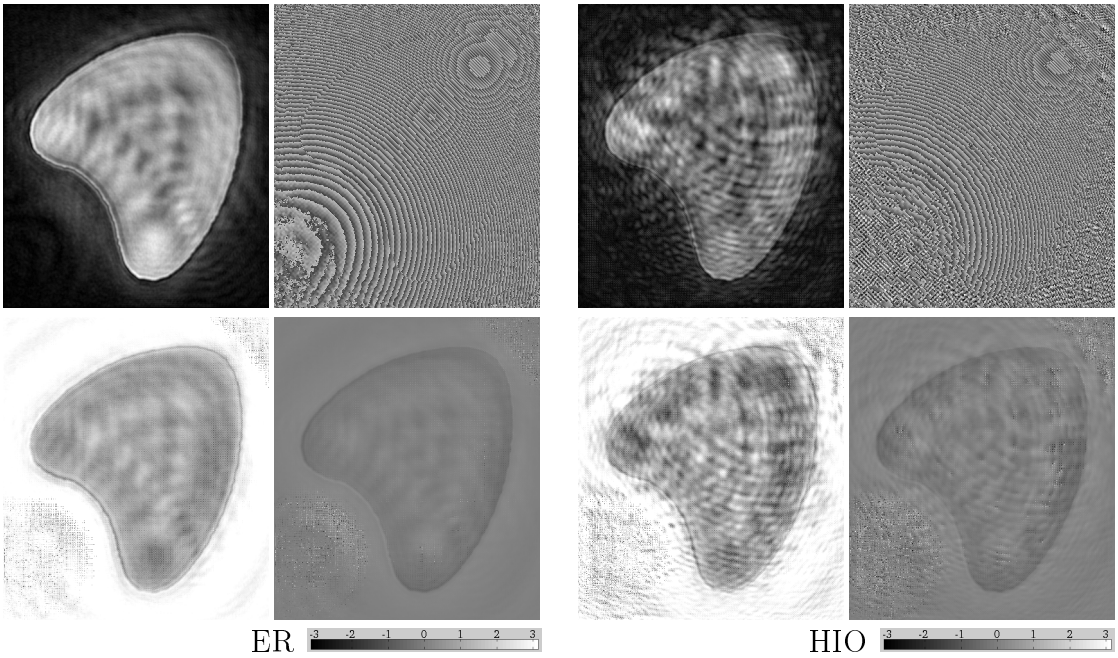

Figure B.2.6: **Background subtracted: 70% in DPD (SNR = 5.9), 70% in WFD.**

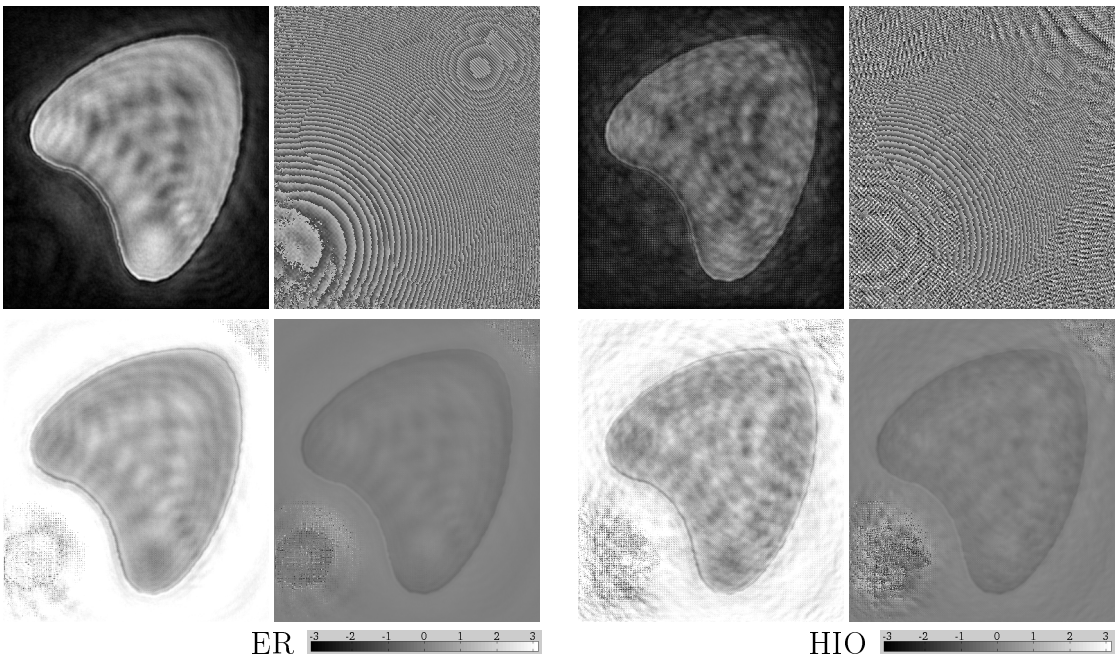

Figure B.2.7: **Background subtracted: 90% in DPD (SNR = 17.4), 90% in WFD.**

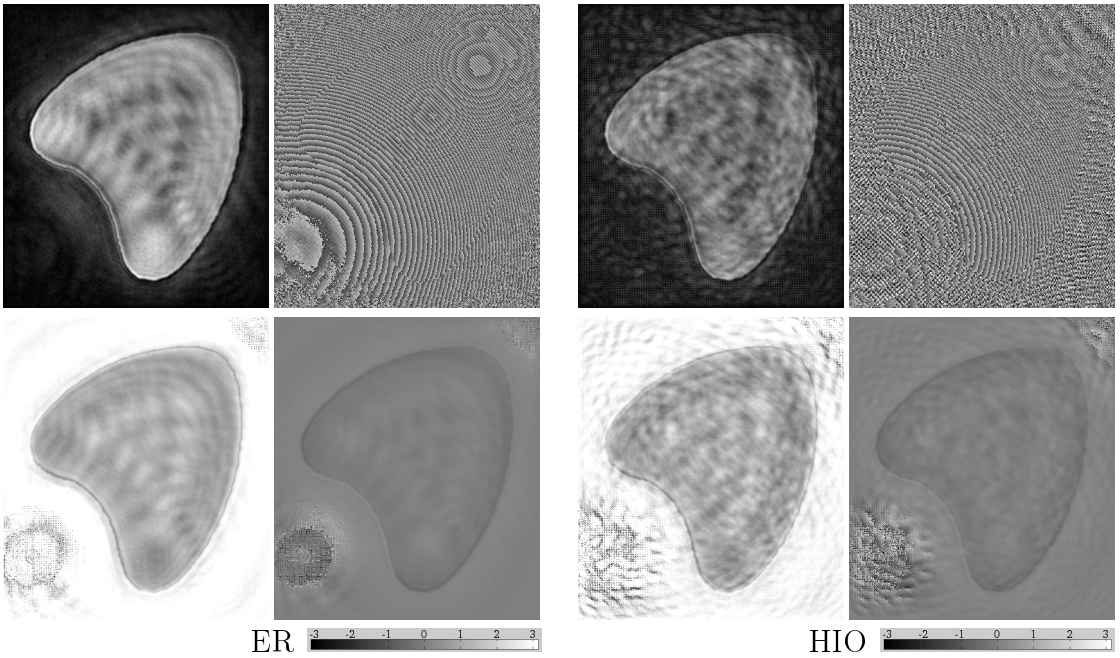

Figure B.2.8: **Background subtracted: 95% in DPD (SNR = 33.9), 95% in WFD.**

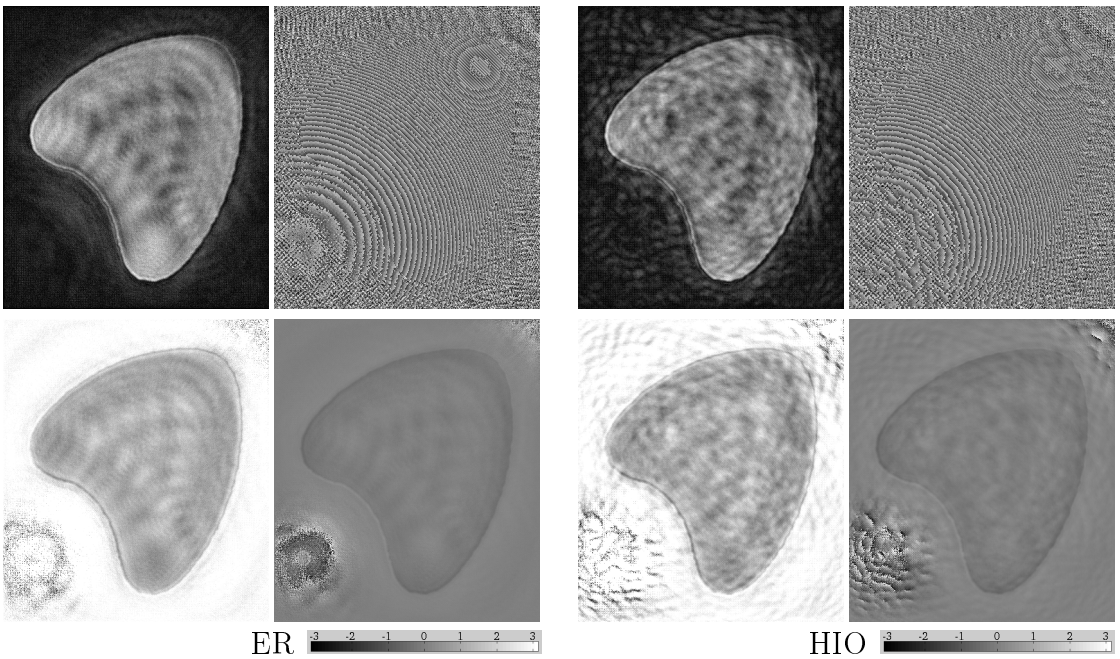

Figure B.2.9: **Background subtracted: 99% in DPD (SNR = 139.3), 99% in WFD.**

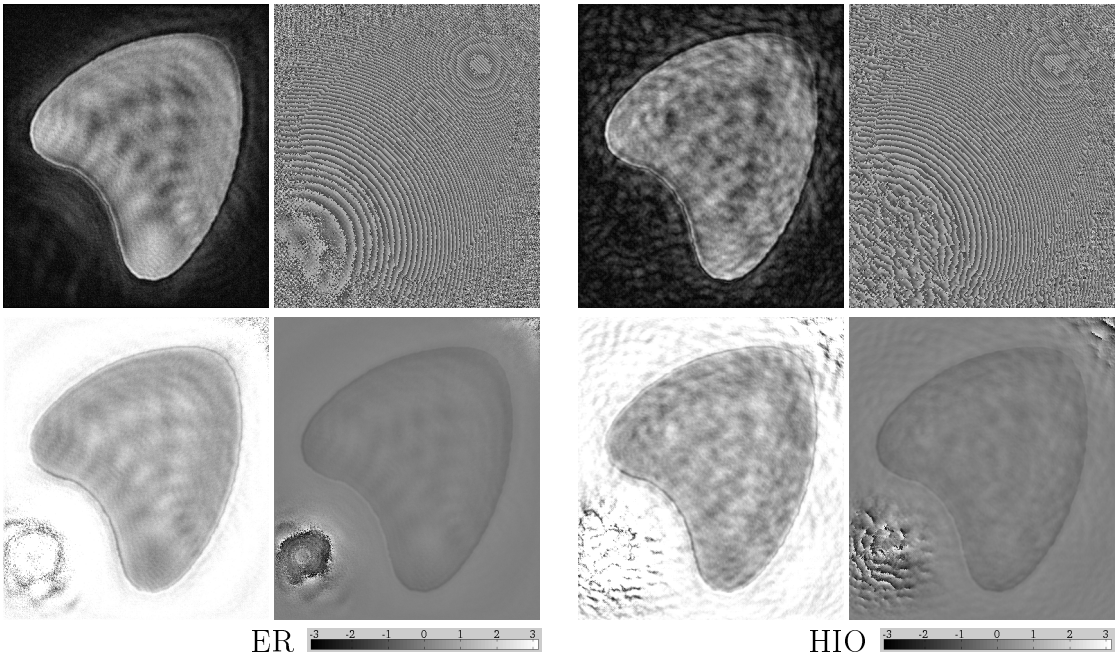

Figure B.2.10: **Background subtracted: 100% in DPD (SNR=338.9), 100% in WFD.**

B.2.2 Case (II)

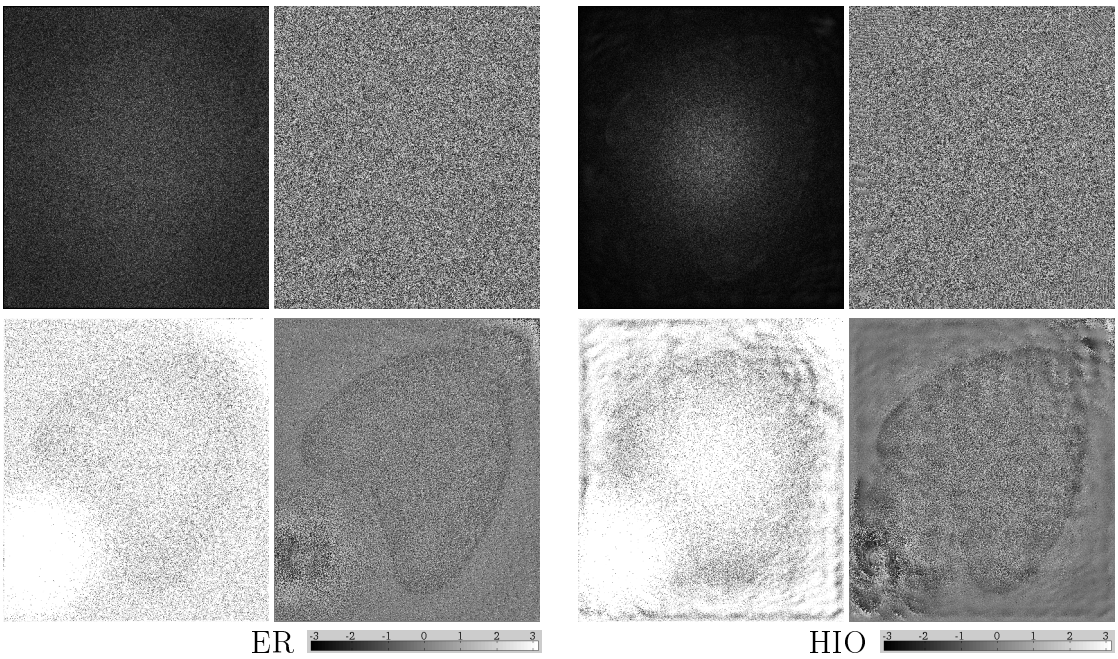

Figure B.2.11: **Background subtracted: 0% in DPD (SNR = 1.8), 100% in WFD.**

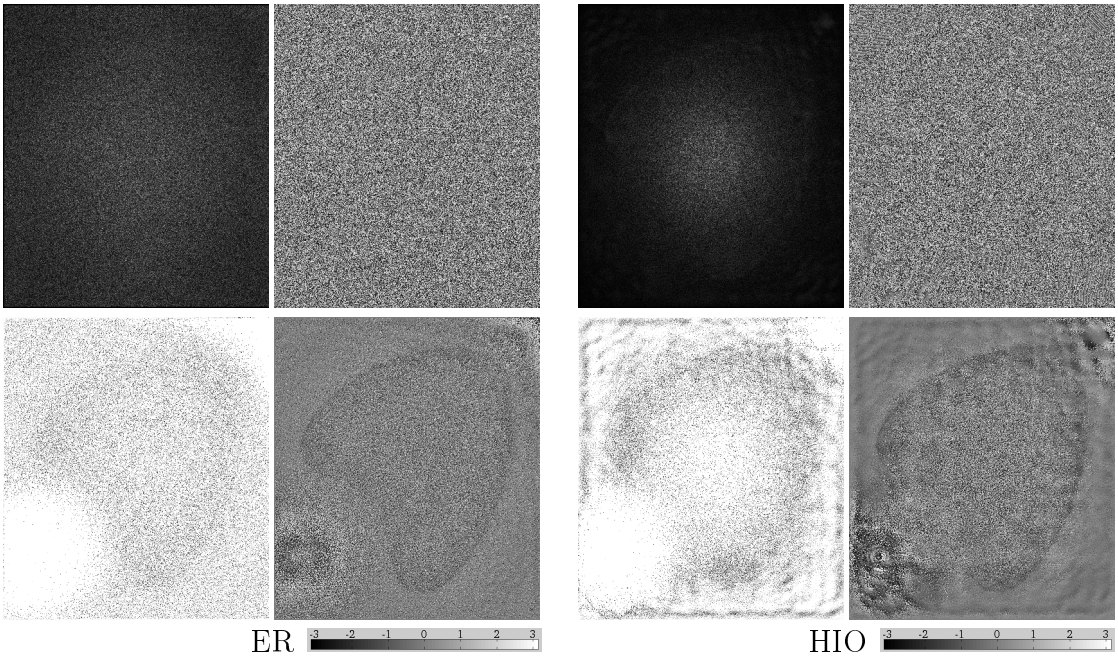

Figure B.2.12: **Background subtracted: 10% in DPD (SNR = 2), 100% in WFD.**

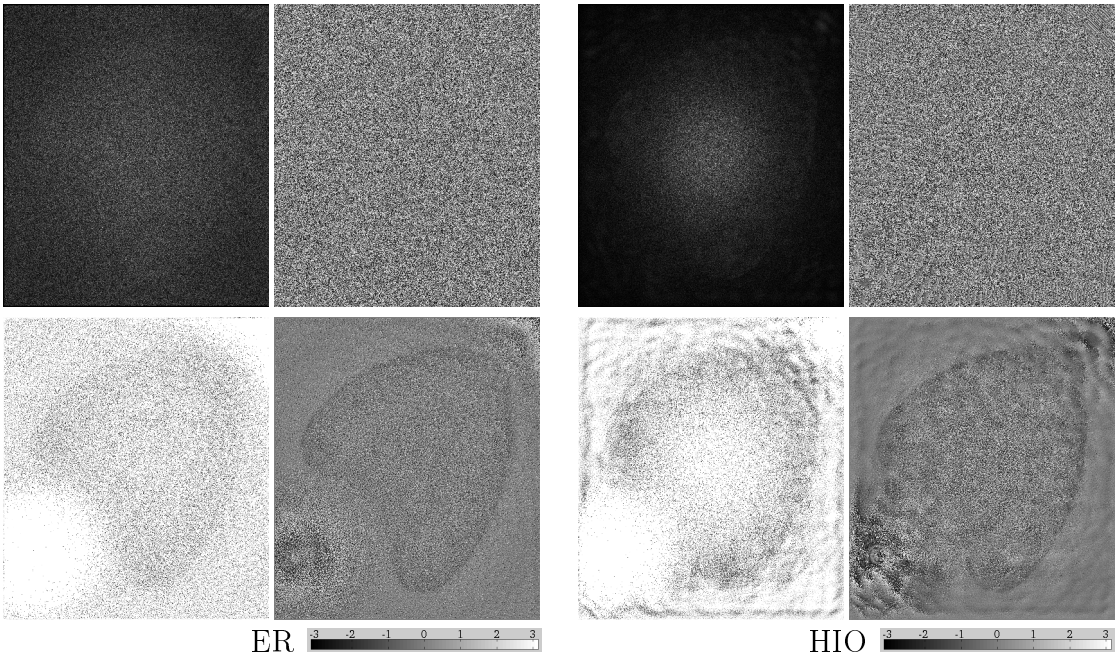

Figure B.2.13: **Background subtracted: 30% in DPD (SNR = 2.5), 100% in WFD.**

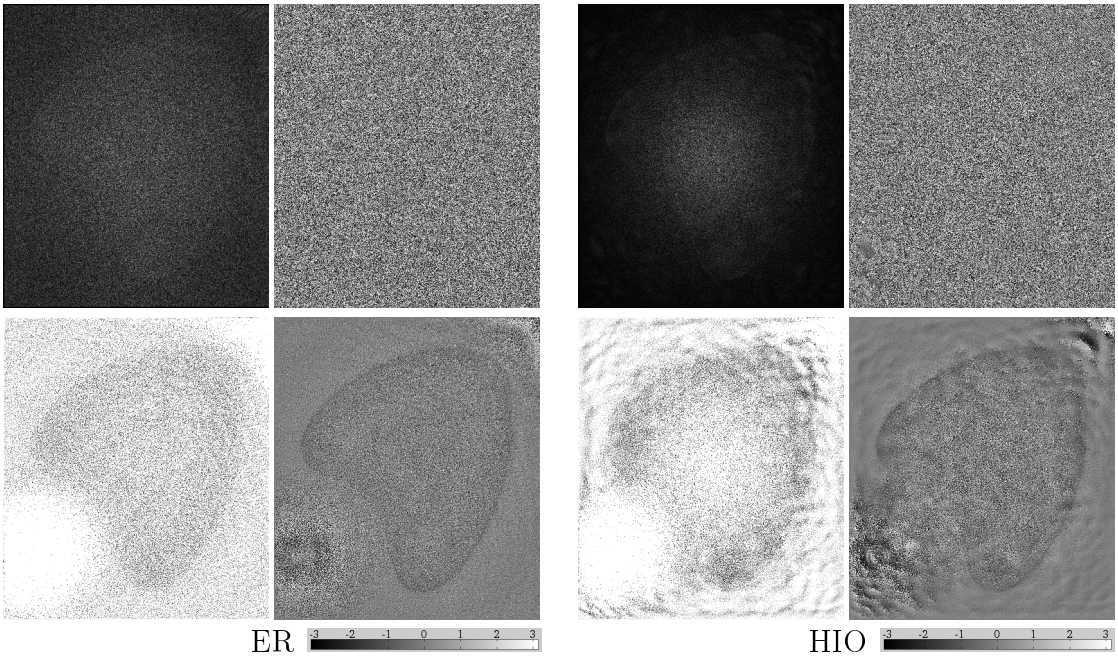

Figure B.2.14: **Background subtracted: 50% in DPD (SNR = 3.5), 100% in WFD.**

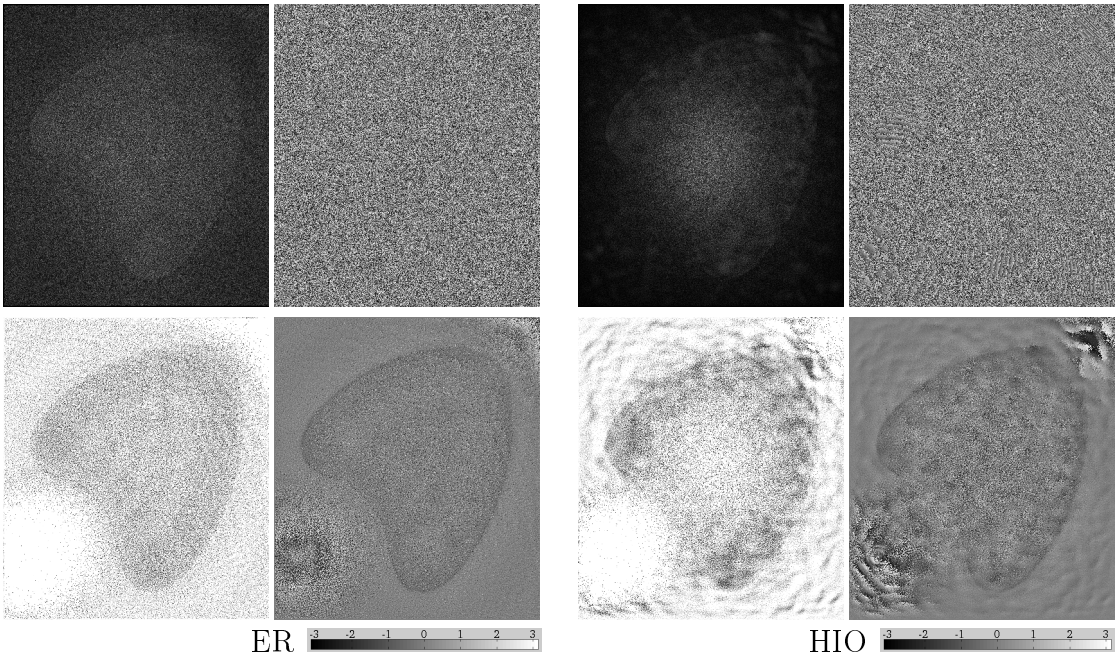

Figure B.2.15: **Background subtracted: 70% in DPD (SNR = 5.9), 100% in WFD.**

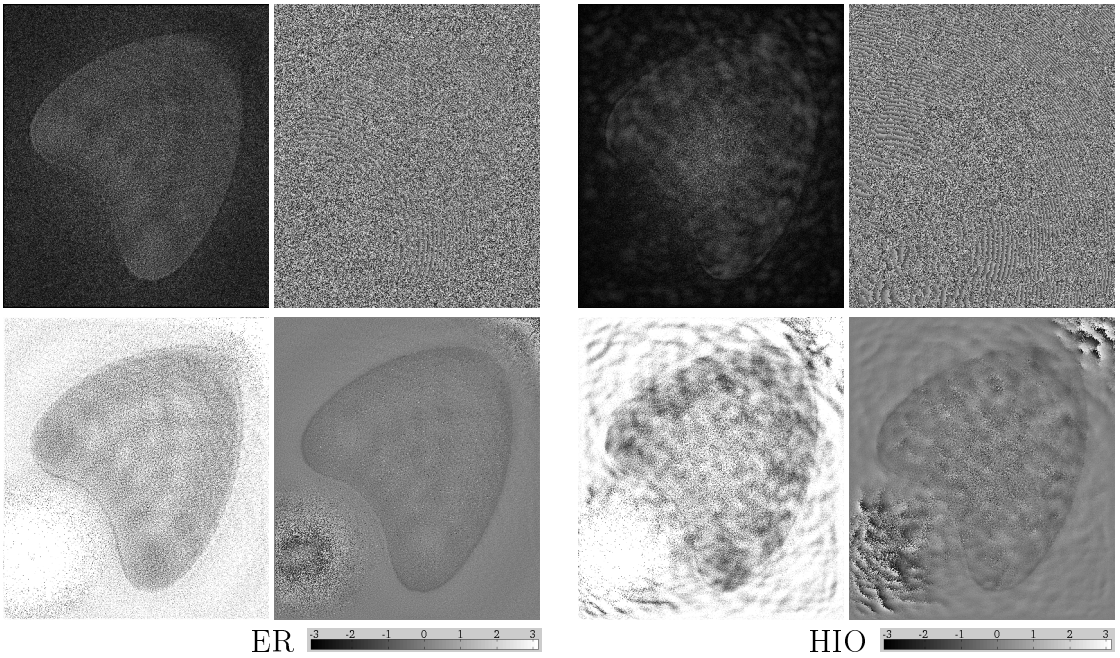

Figure B.2.16: **Background subtracted: 90% in DPD (SNR = 17.4), 100% in WFD.**

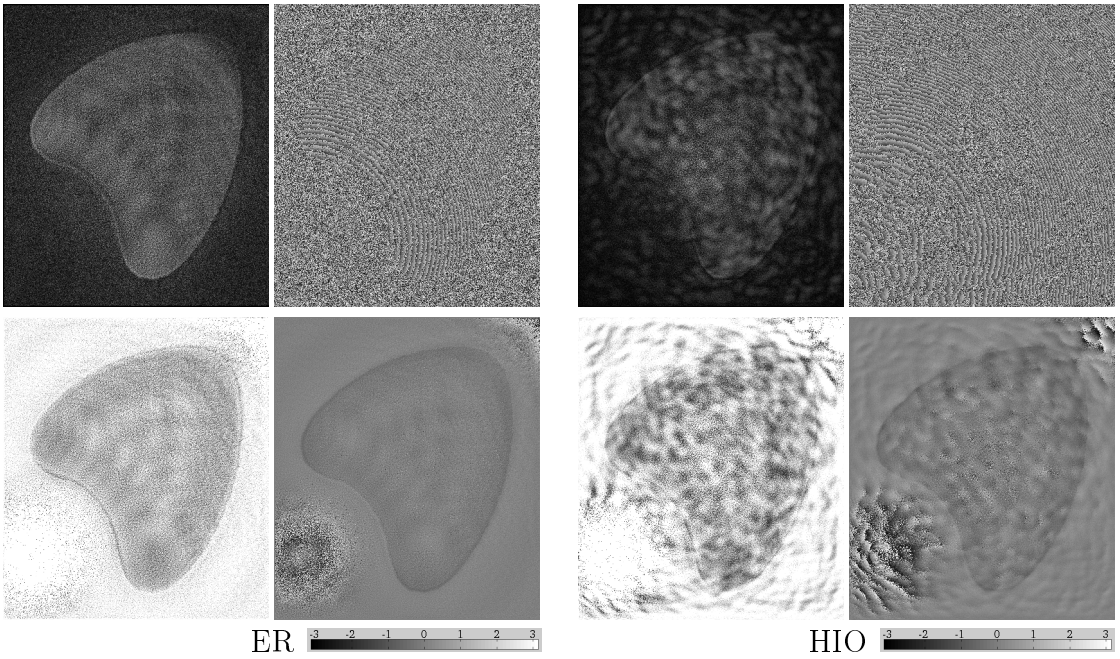

Figure B.2.17: **Background subtracted: 95% in DPD (SNR = 33.9), 100% in WFD.**

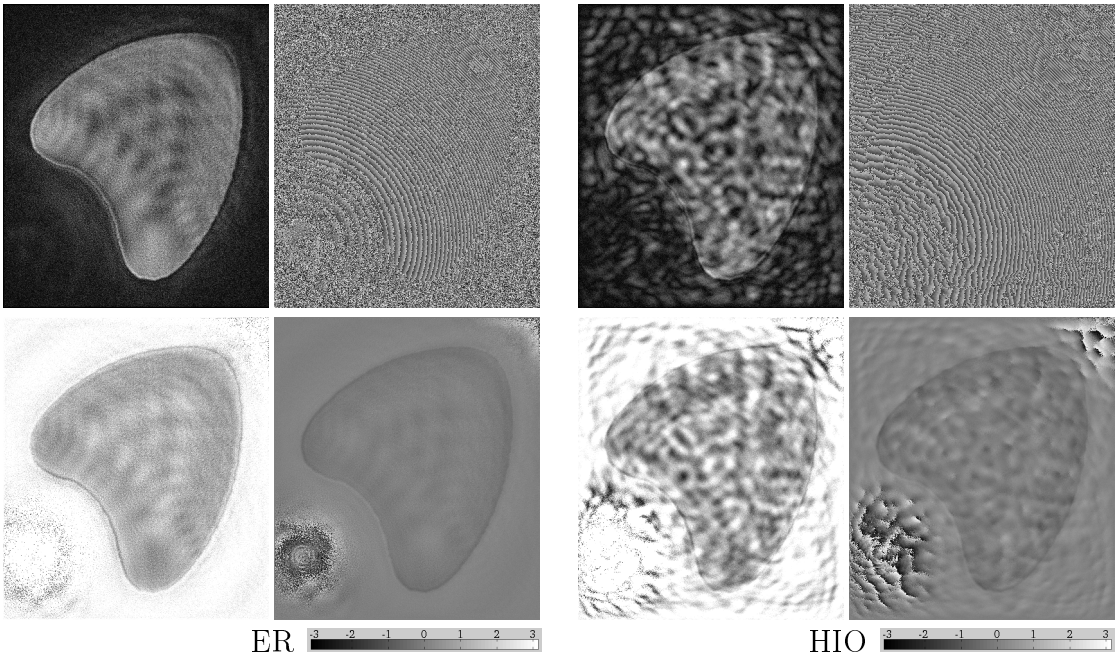

Figure B.2.18: **Background subtracted: 99% in DPD (SNR = 139.3), 100% in WFD.**

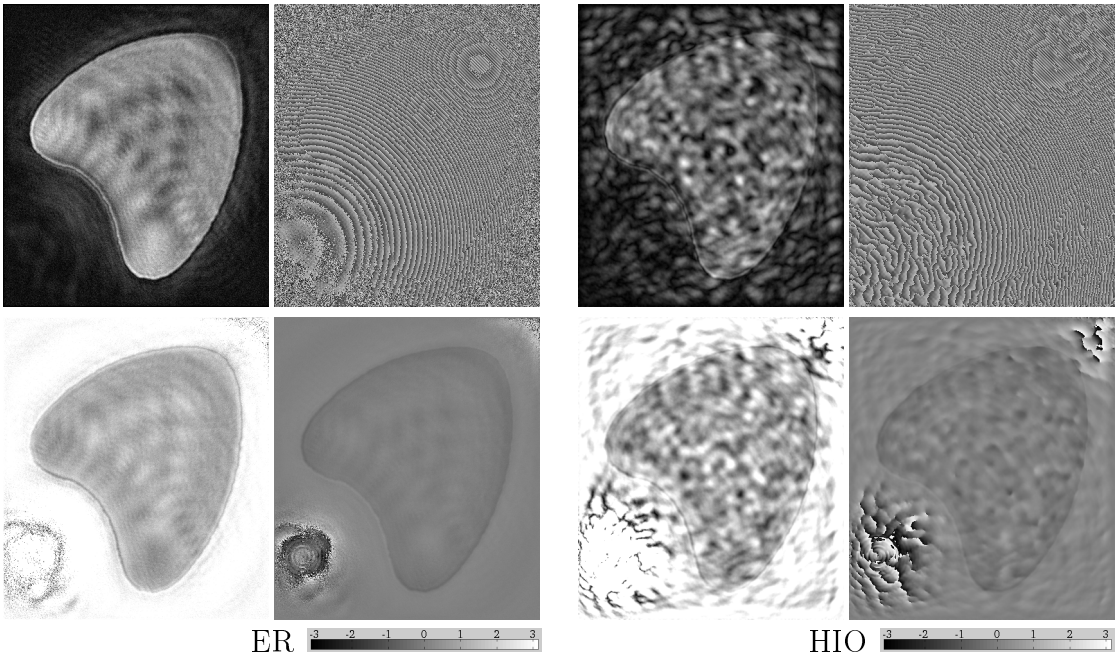

Figure B.2.19: **Background subtracted: 100% in DPD (SNR = 338.9), 100% in WFD.**

B.2.3 Case (III)

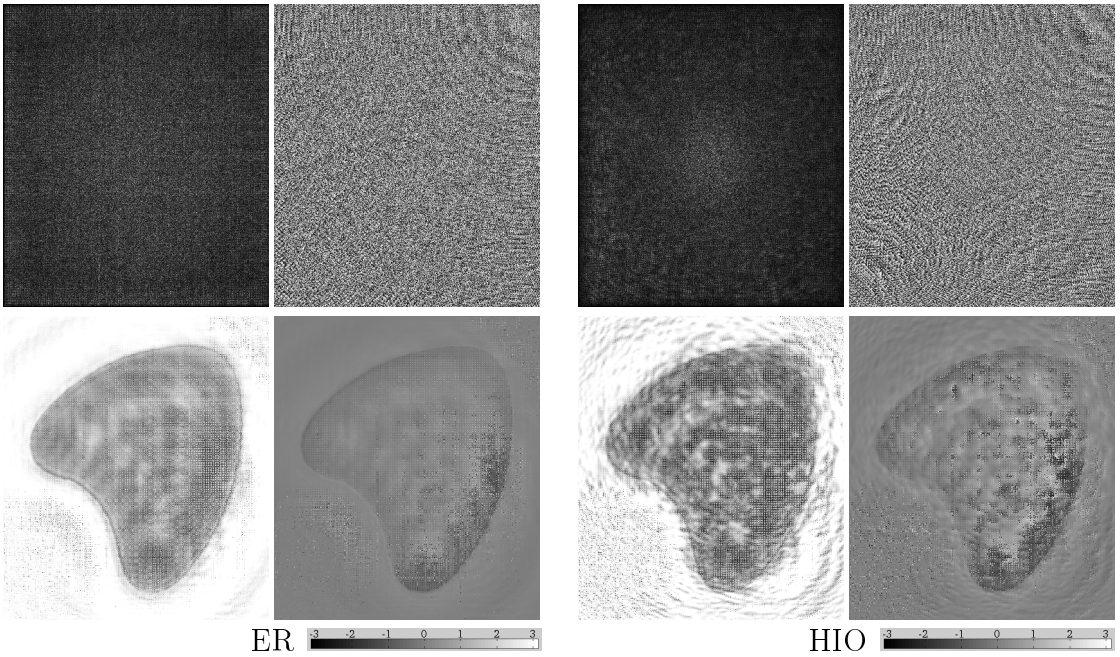

Figure B.2.20: **Background subtracted: 0% in DPD (SNR = 1.8), 95% in WFD.**

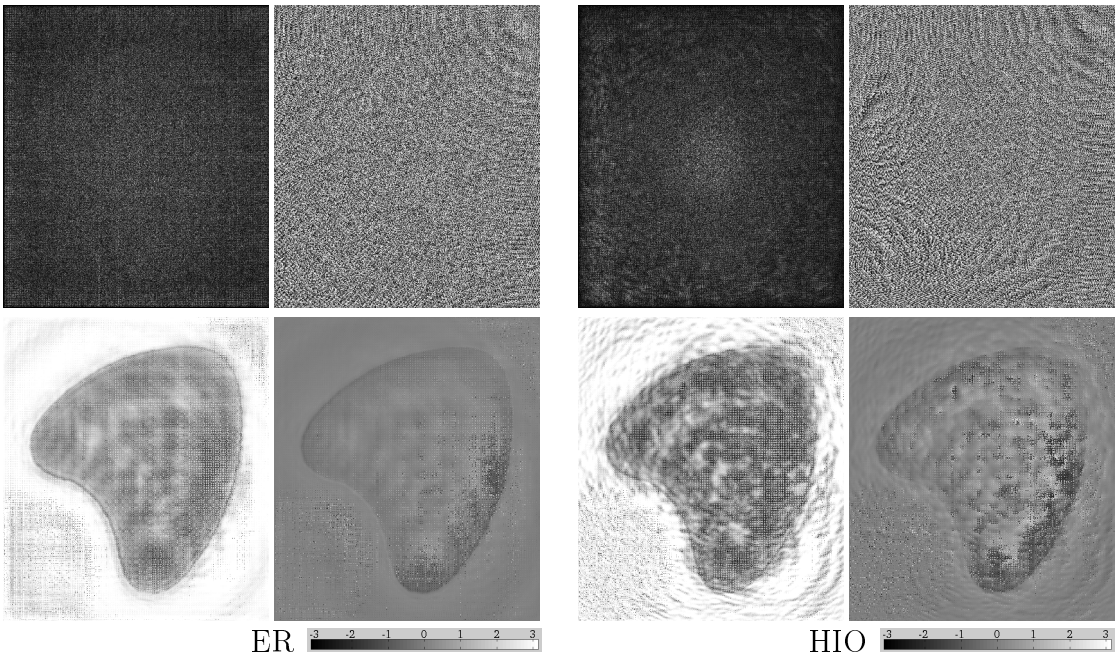

Figure B.2.21: **Background subtracted: 10% in DPD (SNR = 2), 95% in WFD.**

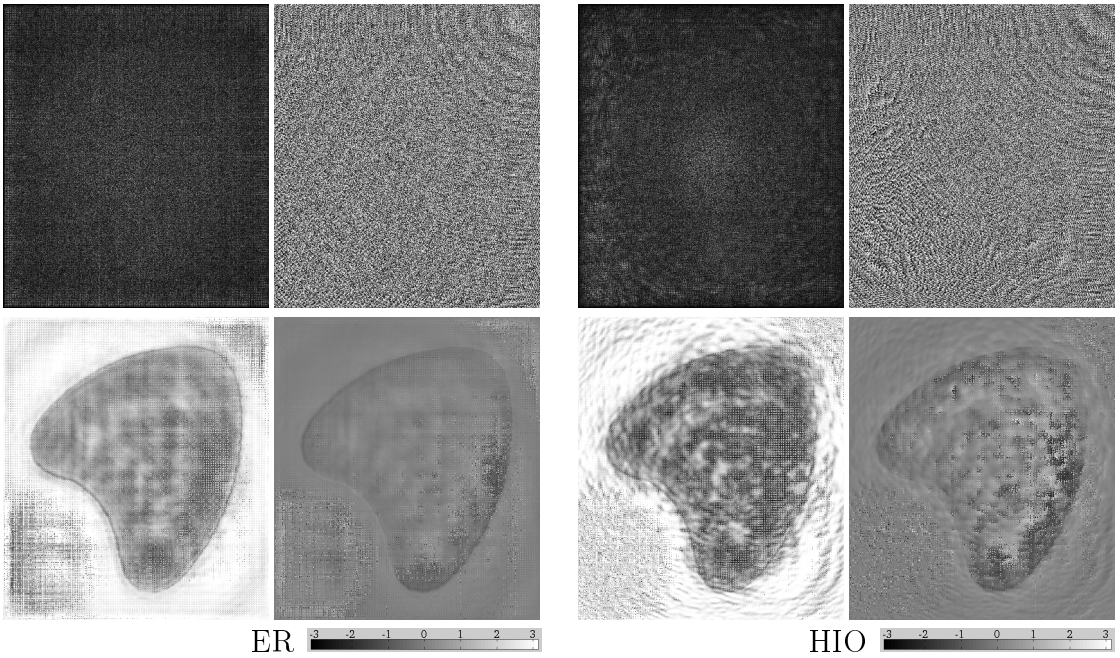

Figure B.2.22: **Background subtracted: 30% in DPD (SNR = 2.5), 95% in WFD.**

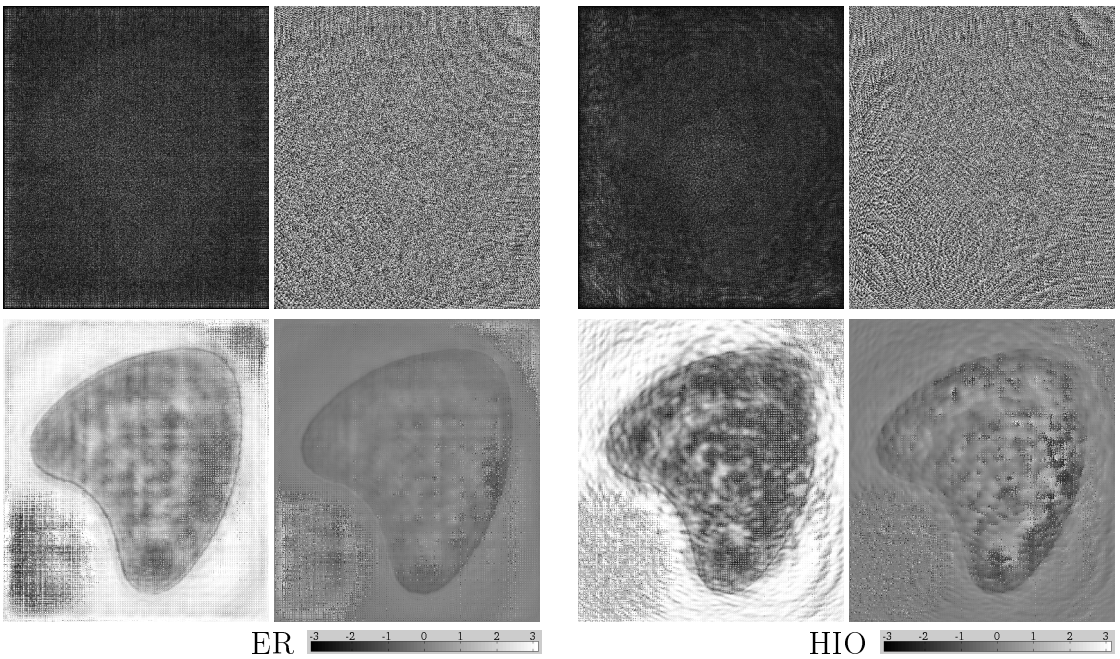

Figure B.2.23: **Background subtracted: 50% in DPD (SNR = 3.5), 95% in WFD.**

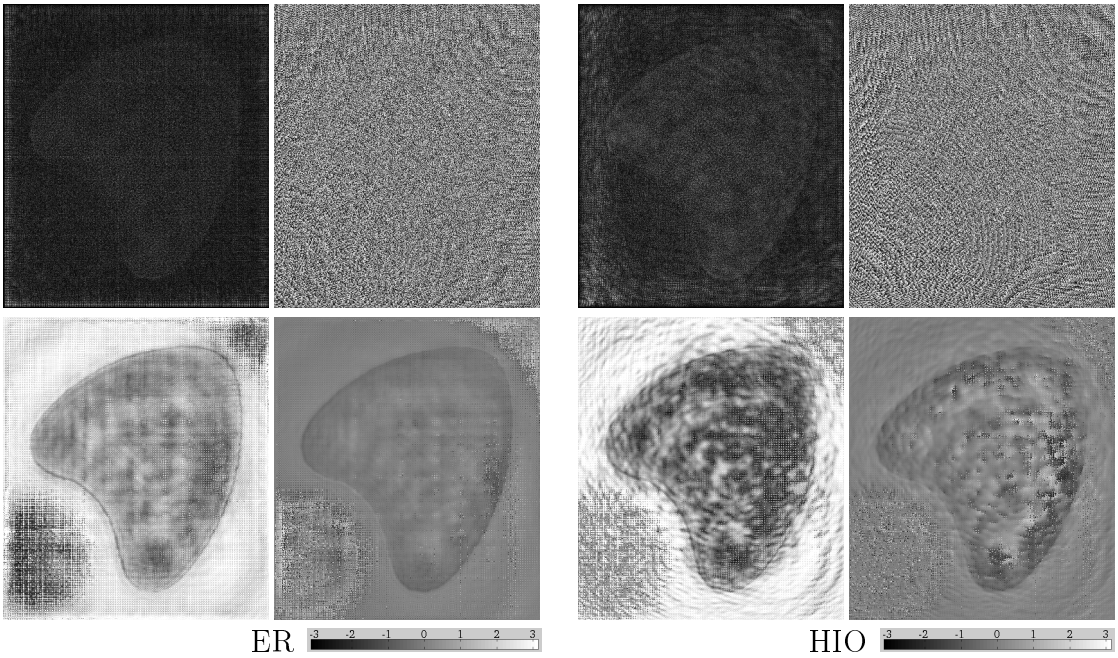

Figure B.2.24: **Background subtracted: 70% in DPD (SNR = 5.9), 95% in WFD.**

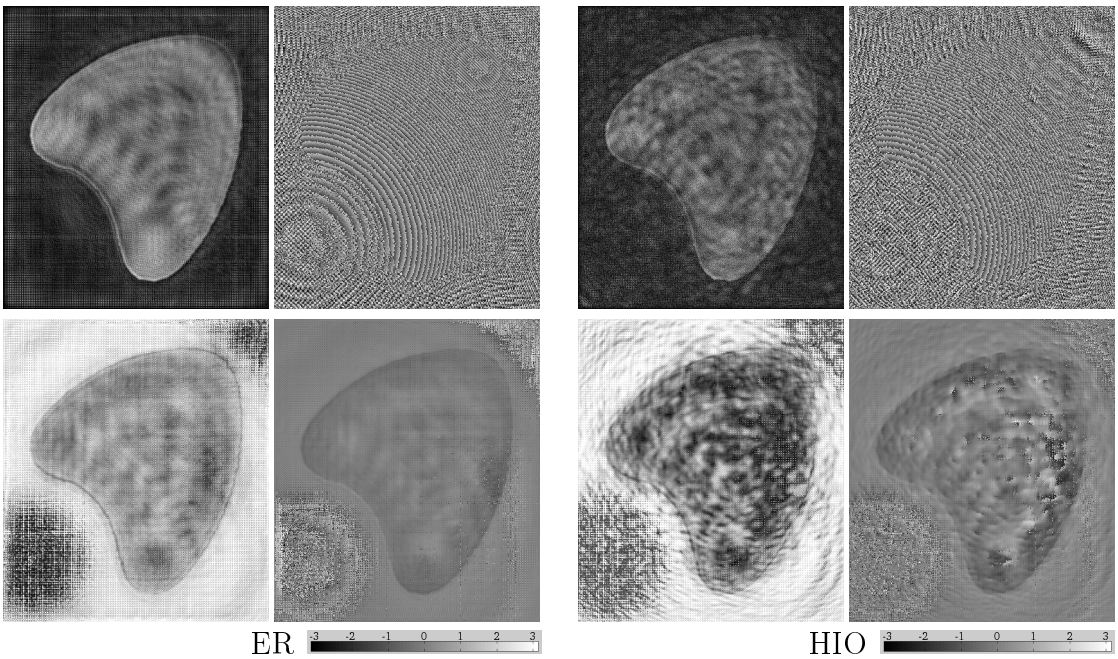

Figure B.2.25: **Background subtracted: 90% in DPD (SNR = 17.4), 95% in WFD.**

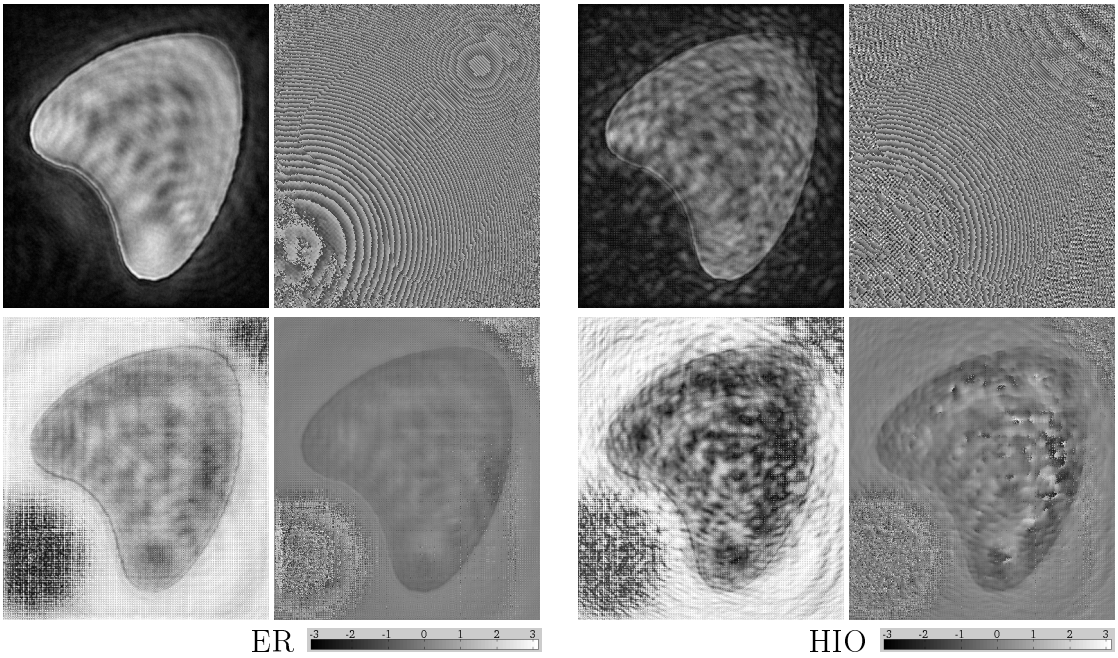

Figure B.2.26: **Background subtracted: 95% in DPD (SNR = 33.9), 95% in WFD.**

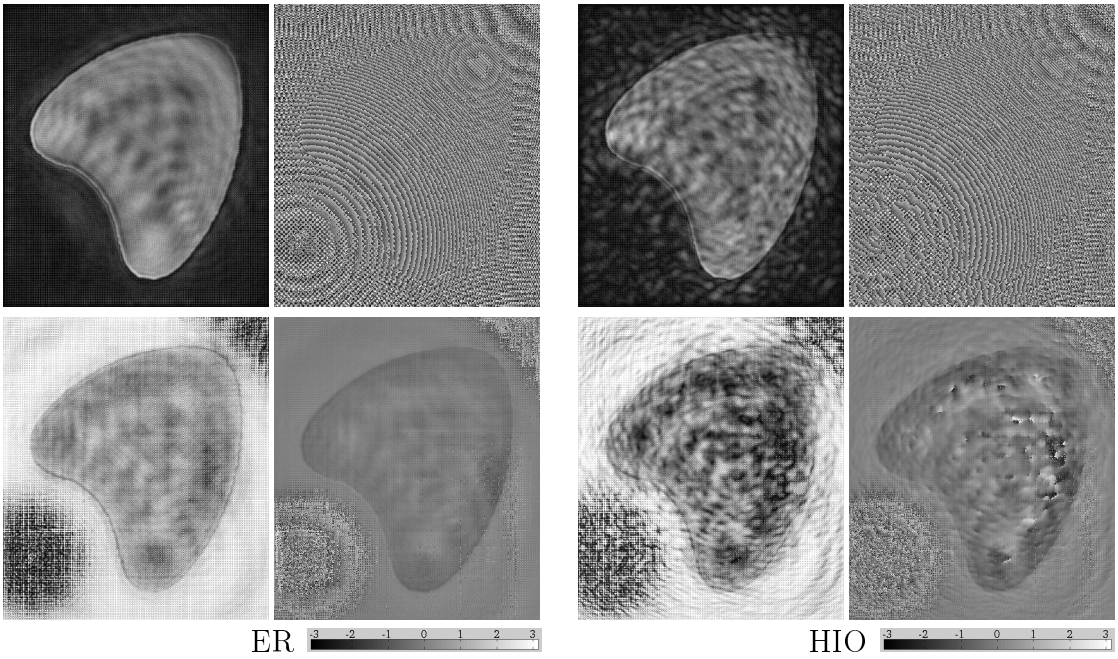

Figure B.2.27: **Background subtracted: 99% in DPD (SNR = 139.3), 95% in WFD.**

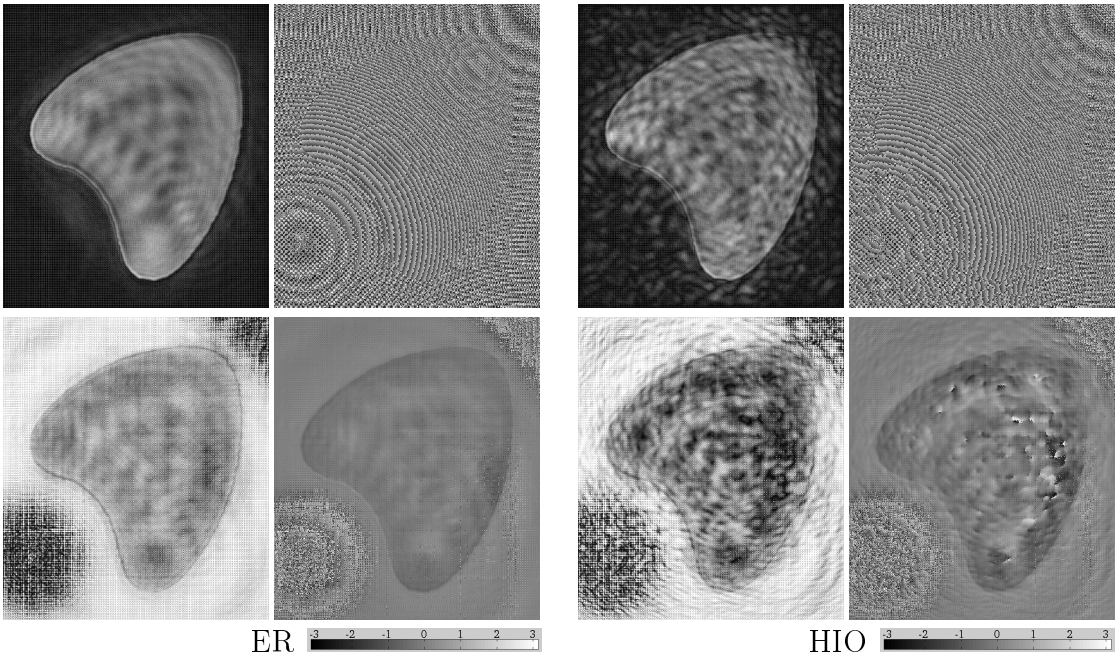

Figure B.2.28: **Background subtracted: 100% in DPD (SNR = 338.9), 95% in WFD.**

B.2.4 Error Metrics of Chapter 4, Comparing Magnitude And Phase Entities

Here we show the error metrics of Chapter 4, that compare magnitude and phase entities rather than the complex entity that was shown in Chapter 4.

The magnitude entities error metrics below, is almost identical to the error metrics comparing the complex entities.

Regarding the Phase entities error metrics, ${}^{TF}\xi_1^0$, ${}^{TF}\xi_1^2$, ${}^{TF}\chi^2$ are similar to the error metrics comparing magnitude or complex entities. Also characteristic for ξ_1^0, ξ_1^2, χ^2 comparing phase entities is that they show closer agreement than when comparing the complex or magnitude entities. The ξ_1^0 for ER and HIO overlaps (and sometimes with ξ_1^2, χ^2), when either or both are not visible in the graphs.

B.2.4.1 Photon number

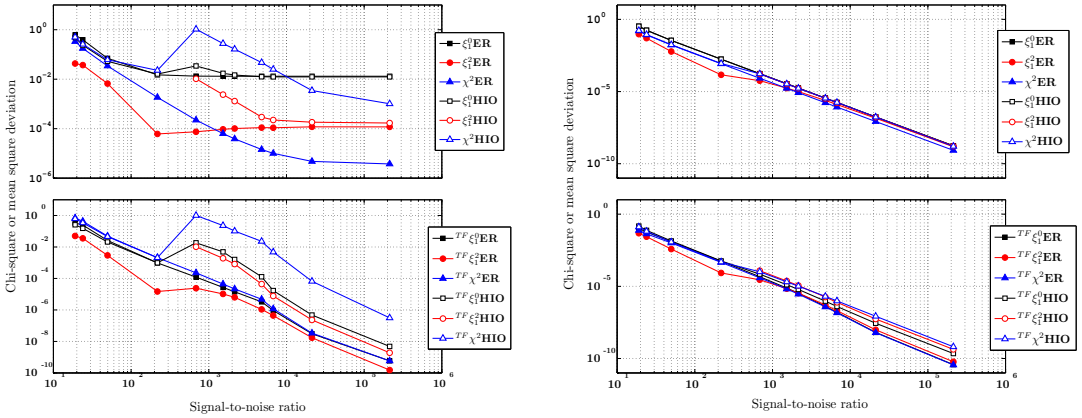

(a) (b)

Figure B.2.29: Error metrics of Section 4.3.2 (Photon number). Entities compared; (a) Magnitude. (b) Phase, for ER ${}^{TF}\xi_1^0$ overlaps with ${}^{TF}\chi^2$. And ξ_1^0 for ER and HIO overlaps, also with HIO ξ_1^2.

B.2.4.2 Iteration number

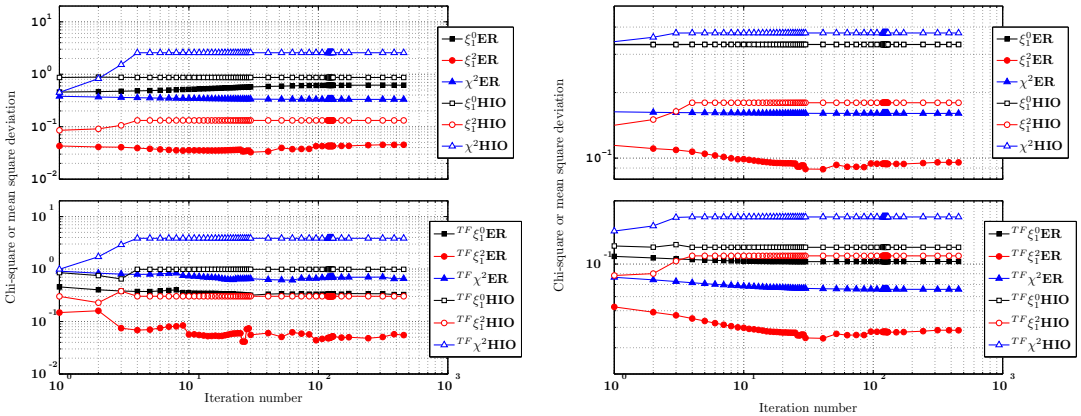

(a) (b)

Figure B.2.30: Error metrics of Section 4.3.2.1 (Iteration number), case $5{\times}10^5$ photons. Entities compared; (a) Magnitude. (b) Phase.

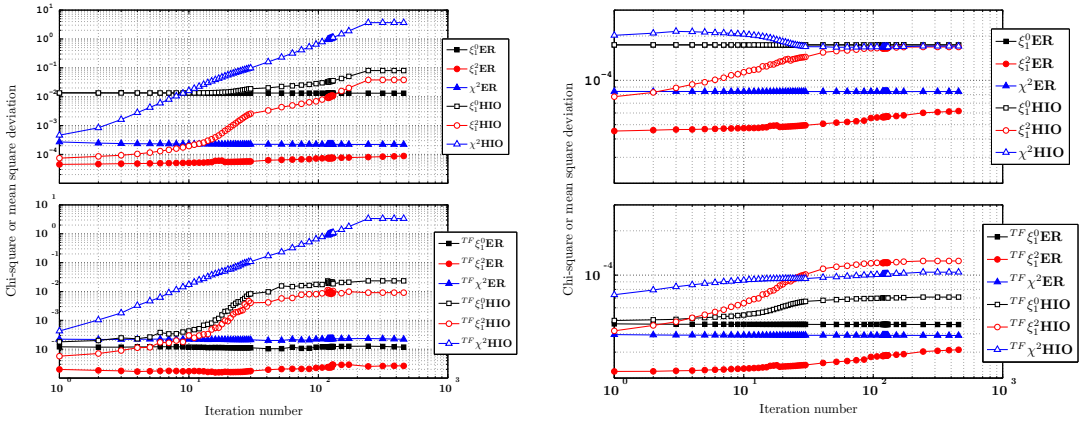

(a) (b)

Figure B.2.31: Error metrics of Section 4.3.2.1 (Iteration number), case 10^9 photons. Entities compared; (a) Magnitude. (b) Phase.

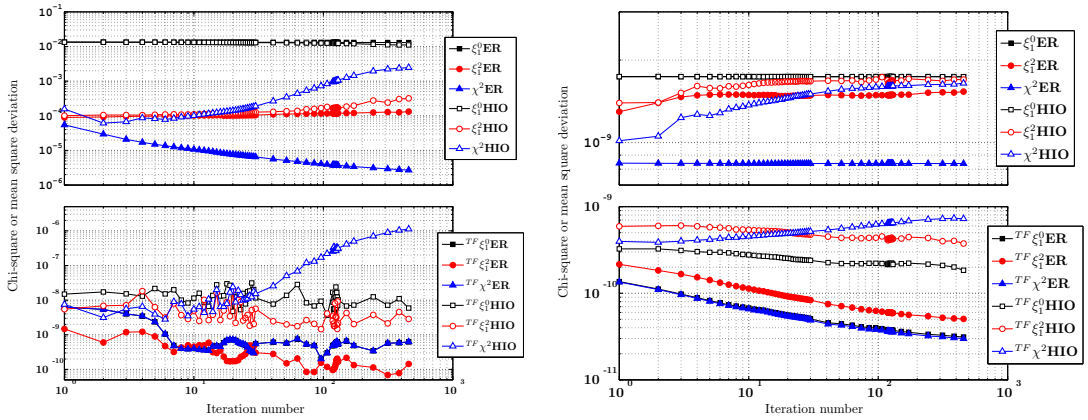

(a) (b)

Figure B.2.32: Error metrics of Section 4.3.2.1 (Iteration number), case 10^{14} photons. Entities compared. (a) Magnitude, (b) Phase.

B.2.4.3 Incomplete Background Subtraction

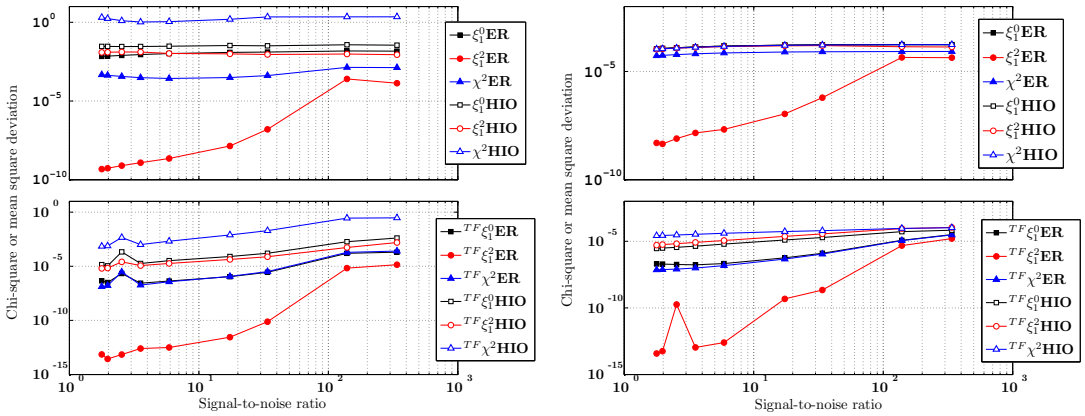

(a) (b)

Figure B.2.33: Error metrics of Section 4.3.3.1 (Case I). Entities compared; (a) Magnitude. (b) Phase.

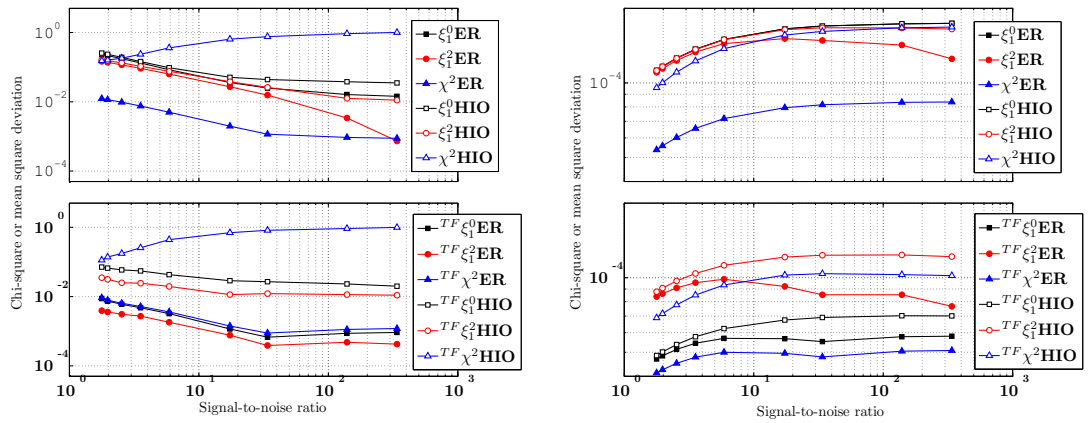

(a) (b)

Figure B.2.34: Error metrics of Section 4.3.3.2 (Case II). Entities compared; (a) Magnitude. (b) Phase.

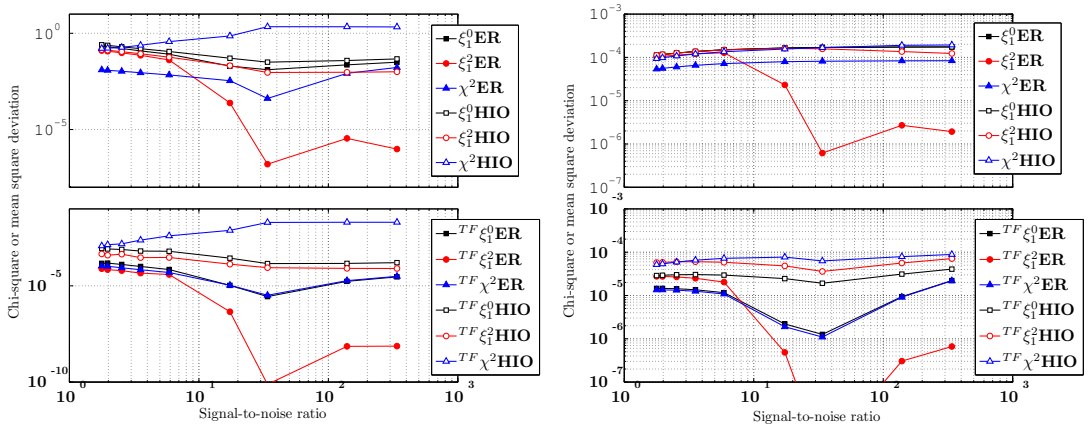

Figure B.2.35: Error metrics of Section 4.3.3.3 (Case III). Entities compared; (a) Magnitude. (b) Phase.

B.2.4.4 Additional tests

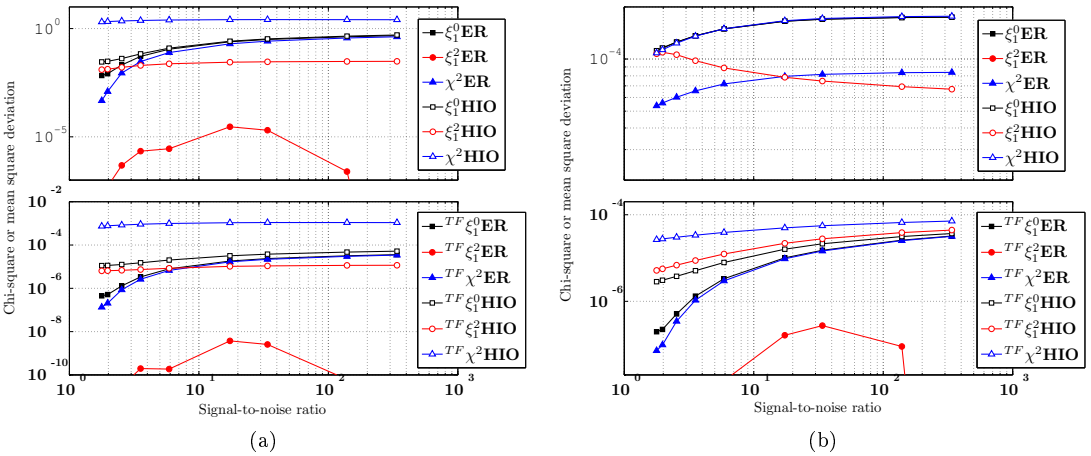

Figure B.2.36: Error metrics of Section 4.3.3.4 (Additional tests; 0% background subtracted white-field data, 0-100% background subtracted diffraction data). Entities compared. (a) Magnitude. (b) Phase.

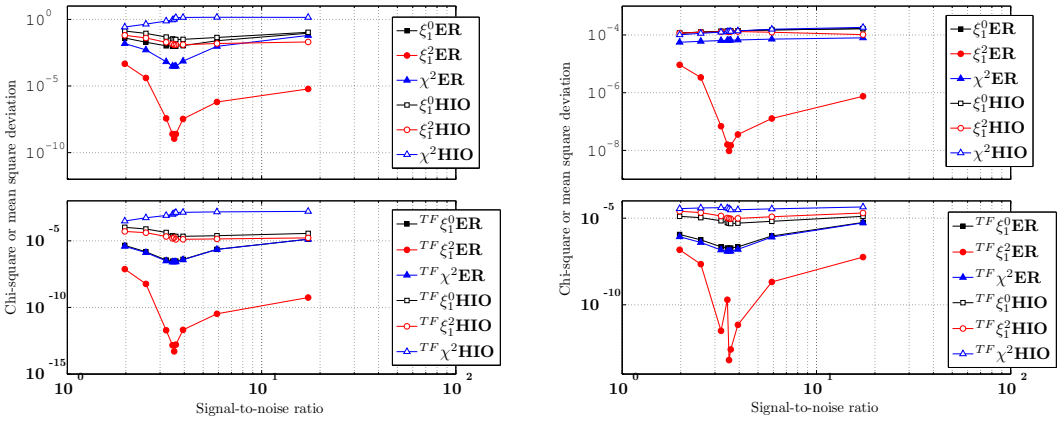

Figure B.2.37: Error metrics of Section 4.3.3.4 (Additional tests; 50% background subtracted white-field data, 0-100% background subtracted diffraction data). Entities compared; (a) Magnitude. (b) Phase.

References

[1] Ivan Vartanyants Ian Robinson Garth Williams, Mark Pfeifer. Effectiveness of iterative algoirithms in recovering phase in the presence of noise. *Acta Cryst.*, A63:36–42, 2007.

[2] Garth J. Williams. *Microscopy of gold microcrystals by coherent x-ray diffractive imaging.* PhD thesis, University of Illinois, U.S.A. Illinois. Urbana, 2005.

[3] Ian K. Robinson. Garth J. Williams, Mark A. Pfeiferm Ivan A. Vartanyants. Convergence of phase inversion for simple crystal shapes using coherent x-ray diffraction. *Proc.SPIE*, 5562:208, 2004.

[4] Lubert Stryer Jeremy M. Berg, John L. Tymoczko. *Biochemistry, sevent edition.* W. H. Freeman and Company, 2011.

[5] Henry N. Chapman... Femtosecond x-ray protein nanocrystallography. *Nature*, 470:73–78, 2011.

[6] R. H. T. Bates. *Optik (Stuttgart)*, 61:247–262, 1982.

[7] Z. Caim D. Paterson H. M. Quiney, A. G. Peele and K. A. Nugent. Diffractive imgaing of highly focused x-ray fields. *Nature Physics*, 2:101–104, 2006.

[8] Pitts T A and Greenleaf J F. Fresnel transform phase retrieval from magnitude. *IEEE Trans. Ultrason. Ferroelectr. Freq. Control 8*, pages 1035–45, 2003.

[9] H. M. Quiney D. J. Vine R. A. Dilanian S. Flewett K. A. Nugent A. G. Peele E. Balaur I. Mcnulty L. W. Whitehead, G. J. Williams. Diffractive imaging using partially coherent x-rays. *Physical review letters*, PRL 103, 2009.

[10] Andrew G. Peele Garth J. Williams, Harry M. Quiney and Keith A. Nugent. Coherent diffractive imaging and partial coherence. *Physical review letters B*, 75, 2007.

[11] C. Kittel. *Introduction to Solid State Physics, Eight edition.* John Wiley and Sons, 2005.

[12] Corey T. Putkunz. *New Methods in Fresnel Coherent Diffractive Imaging.* PhD thesis, La Trobe Univerisy, Australia, Melbourne, 2011.

[13] H. M. Quiney. Tutorial review. coherent diffractive imaging using short wavelength light sources. *Journal of Modern Optics*, 57:1109–1149, 2011.

[14] David M. Paganin. *Coherent x-ray optics.* Oxford university press, 2006.

[15] Keith A. Nugent Henry N. Chapman. Coherent lensless x-ray imaging. *Nature Photonics*, 4:833–839, 2010.

[16] Gerchberg R W and Saxton W O. A practical algorithm for the determination of phase from image and diffraction plane pictures. *Optik*, 35:237–46, 1972.

[17] J. R. Fienup. Phase retrieval algorithms: a comparison. *Applied optics*, 21:15, 1982.

[18] L. W. Whitehead D. J. Vine A. G. Peele E. Balaur I. Mcnulty H. M. Quiney R. A. Dilanian, G. J. Williams and K. A. Nugent. Coherent diffractive imaging: a new statistically regularized amplitude constraint. *New Journal of Physics*, 12, 2010.

[19] Okan K. Ersoy. *Diffraction, Fourier Optics and Imaging.* Wiley series in pure and applied optics, 2007.

[20] B. B. Dhal C. Q. Tran K. A. Nugent A. G. Peele D. Paterson G. J. Williams, H. M. Quiney and M. D. de Jonge. Fresnel coherent diffractive imaging. *Physical Review Letters*, PRL 97:025506, 2006.

[21] A. Carroll. Characterization of a zone plate focus at the x-ray fluorescence microprobe beamline of the australian synchotron. Master's thesis, La Trobe University, Department of physics, 3086, Melbourne, Victoria, Australia, 2010.

[22] A. G. Peele G. J. Williams, H. M. Quiney and K. A. Nugent. Fresnel coherent diffractive imaging: treatment and analysis of data. *New Journal of physics*, 12, 2010.

[23] G. J. Williams J.N. Clark A. G. Peele M. A. Pfeifer M. D. Jonge I. Mcnulty. B. Abbey, K. A. Nugent. Keyhole coherent diffractive imaging. *Nature Physics*, 4:394–398, 2008.

[24] W. R. Leo. *Techniques for Nuclear and Particle Physics Experiments, A How-to Approach, Second Revised Edition.* Springer Verlag, 1994.

[25] X-ray Group Princeton Instruments. Direct detection of x-rays (30ev to 20kev) using detectors based on ccd technology. *Technical note nr1. Princeton instruments*, 2010.

[26] X-ray group Princeton instruments. Pi-mte 2048b. *www.princetoninstruments.com.*

[27] J. Osterman C. Nordling. *Physics handbook, 8th edition.* Student litteratur AB, 2006.

[28] `http://www.coecxs.org/joomla/index.php/research-and-projects/nadia-software-project.html`.

[29] J. R. Fienup and C.C. Wackerman. Phase-retrieval stagnation problem and solutions. *J. Opt. Soc. Am. A.*, 3:1897–1907, 1986.

[30] E. M. Gullikson B. L. Henke and J. C. Davis. X-ray interactions- photoabsorption, scattering, transmission, and reflection at e=50-30,000 ev, z=1-92. *At. Data Nucl. Data Tables 54(2)*, pages 181–342.

[31] Andrew G. Peele Mark A. Pfeifer Jesse Clark Brian Abbey Guido Cadenazzi Martin D. de Jonge Stefan Vogt Leann Tilley Keith A. Nugent Garth J. Williams, Eric Hanssen. High resolution x-ray imaging of plasmodium falciparum infected red blood cells. *Cytometry Part A*, 73A (Issue 10):949–957, 2008.

[32] Evan K. Curwood David J. Vine Robert Scholten Ian Mcnulty Keith A. Nugent Jesse N. Clark, Corey T. Putkunz and Andrew G. Peele. Dynamic sample imaging in coherent diffractive imaging. *optics letters*, 36. No.11:1954–1956, 2011.

[33] G. D. Demeester H. H. Barrett. Quantum noise in fresnel zone plate imaging. *Applied optics*, 13, No. 5:1100–1109, 1974.

[34] Jan Steinbrener Johanna Nelson David Shapiro Andrew Stewart Joshua Turner Chris Jacobsen Xiaojing Huang, Huijie Miao. Signal-to-noise and radiation exposure considerations in conventional and diffraction x-ray microscopy. *Opt Express*, 17(16):13541–13553, 2009.

[35] `http://mathworld.wolfram.com/NormalSumDistribution.html`.

[36] M. A. Pfeifer A. G. Peele G. J. Williams B. Chen K. A. Nugent C. Hall W. Fullagar S. Kim J. N. Clark, C. T. Putkunz and I. Mcnulty. Use of a complex constraint in coherent diffractive imaging. *Optics express*, 18:No.3, 2010.

[37] A. G. Peele H. M. Quiney, K. A. Nugent. Iterative image reconstruction algorithms using wave-front intensity and phase variation. *Optics letters*, 30, No.13, 2005.

[38] A. V. Martin et al. Noise-robust coherent diffractive imaging with a single diffraction pattern. *Optics express*, 20. No.15:16650–16661, 2012.